Ultrahigh-energy cosmic rays, superheavy long-lived particles, and matter creation after inflation

V. A. Kuzmin[a)]
Institute for Nuclear Research, Russian Acadmey of Sciences, 117312 Moscow, Russia

I. I. Tkachev[b)]
Institute for Nuclear Research, Russian Acadmey of Sciences, 117312 Moscow, Russia; Department of Physics, Purdue University, West Lafayette, IN 47907, USA

(Submitted 2 June 1998; resubmitted 24 July 1998)
Pis'ma Zh. Éksp. Teor. Fiz. **68**, No. 4, 255–259 (25 August 1998)

Cosmic rays of the highest energy, above the Greisen–Zatsepin–Kuzmin (GZK) cutoff of the spectrum, may originate in decays of superheavy long-lived particles. We conjecture that these particles may be produced naturally in the early Universe from vacuum fluctuations during inflation and may constitute a considerable fraction of cold dark matter. We predict a new cutoff in the ultrahigh-energy cosmic ray spectrum $E_{\rm cutoff}<m_{\rm inflaton}\approx 10^{13}$ GeV, the exact position of the cutoff and the shape of the cosmic ray spectrum beyond the GZK cutoff being determined by the QCD quark/gluon fragmentation. The Pierre Auger Project installation may in principle observe this phenomenon.
 [S0021-3640(98)00116-9]

PACS numbers: 98.70.Sa, 95.85.Ry

According to the Greisen–Zatsepin–Kuzmin (GZK) observation,[1] the energy spectrum of ultrahigh-energy (UHE) cosmic rays produced at far extragalactic distances should exhibit an exponential cutoff at energy $E\sim 5\times 10^{10}$ GeV. However, a number of cosmic ray events with energies well beyond the predicted GZK cutoff have been observed recently by various experimental groups.[2] This is an obvious contradiction with the standard cosmological and particle physics models and clearly requires some new physics beyond the standard model.

A number of possible solutions to the problem have been suggested. One solution to the problem might be provided, for example, by the existence of some exotic particles which are able to propagate (evading the GZK bound) from cosmological distances and yet interact in the Earth's atmosphere like a hadron. A particle with such conflicting properties has been found in a class of supersymmetric theories.[3] Alternatively, the high-energy cosmic rays may have been produced locally within the GZK distance. One possibility is connected with the destruction of topological defects,[4] while another one is connected with decays of primordial long-lived heavy particles.[5,6] The candidate X particle must obviously obey constraints on mass, density, and lifetime.

In order to produce cosmic rays in the energy range $E\gtrsim 10^{11}$ GeV, the mass of X particles has to be very large, $m_X\gtrsim 10^{13}$ GeV.[5,6] The lifetime τ_X cannot be much smaller

than the age of the Universe, $\tau \approx 10^{10}$ yr. With such a short lifetime, the observed flux of UHE cosmic rays will be generated at a rather low density of X particles, $\Omega_X \sim 10^{-12}$, where $\Omega_X \equiv m_X n_X / \rho_{\rm crit}$, n_X is the number density of X particles, and $\rho_{\rm crit}$ is the critical density. On the other hand, the X particles must not overclose the Universe: $\Omega_X \lesssim 1$. At $\Omega_X \sim 1$ the X particles may play the role of cold dark matter, and the observed flux of UHE cosmic rays can be matched if $\tau_X \sim 10^{22}$ yr. The allowed windows are quite wide,[5] but on the exotic side, which may give rise to some problems.

The problem of a particle-physics mechanism responsible for a long but finite lifetime of very heavy particles can be solved in several ways. For example, an otherwise conserved quantum number carried by X particles may exhibit a very weak nonconservation due to instanton transitions[5] or quantum gravity (wormhole) effects.[6] If instantons are responsible for X-particle decays, the lifetime is estimated as $\tau_X \sim m_X^{-1} \times \exp(4\pi/\alpha_X)$, where α_X is the coupling constant of the relevant gauge interaction. The lifetime will fit the allowed window if the coupling constant (at the scale m_X) is $\alpha_X \approx 0.1$ (Ref. 5).

The X particles might be produced in the proper amount by collision and decay processes in cosmological plasma if the reheating temperature after inflation never exceeds m_X, but the temperature should be in the range $10^{11} \lesssim T_r \lesssim 10^{15}$ GeV, depending on m_X (Refs. 5,6). This is a rather high value of the reheating temperature, which may lead to the gravitino problem in generic supersymmetric models.[7]

In the present paper we propose a quite different mechanism of X-particle creation, namely, their direct production by vacuum fluctuations during inflation.

Any viable modern cosmological model invokes the hypothesis of inflation.[8] During inflation the Universe expands exponentially, which solves the horizon and flatness problems of the standard big bang cosmology. Inflation is generally assumed to be driven by the special scalar field ϕ known as the *inflaton*. Fluctuations generated in the inflationary stage may have the strength and the power spectrum suitable for generation of the large scale structure. This fixes the range of parameters of the inflaton effective potential. For example, the mass of the inflaton field has to be $m_\phi \sim 10^{13}$ GeV. During inflation, the inflaton field slowly rolls down towards the minimum of its potential. Inflation ends when the potential energy associated with the inflaton field becomes smaller than the kinetic energy. Coherent oscillations of the inflaton field contained all the energy of the Universe at that time. It is possible that a significant fraction of this energy was released to other boson species after only a dozen oscillations of the inflaton field, in the regime of a broad parametric resonance.[9] This process has been studied in detail.[10,11] It was shown that even rather heavy particles with masses an order of magnitude larger than the inflaton mass can be produced quite copiously. Applying these results to the case of our interest, we find that the stable very heavy particles, $m_\phi \lesssim m_X \lesssim 10\, m_\phi$, will generally be produced in excess and will overclose the Universe.

However, if the parametric resonance is ineffective for some reason, and one estimates the particle number density after inflation at the level of the initial conditions used in Refs. 10 one finds that Ω_X might prove to be of the acceptable magnitude. This level is saturated by the fundamental process of particle creation during inflation from vacuum fluctuations, and it is the same process which generated primordial large scale density perturbations. Parametric resonance for X particles is turned off if the X field either is a

fermion field or its coupling to the inflaton is small, $g^2 \ll 10^4 (m_X/m_\phi)^4 (m_\phi/M_{Pl})^2$ (Ref. 10).

At the epoch close to the end of inflation, the metric of the Universe is conformally flat, $ds^2 = a(\eta)^2 (d\eta^2 - d\mathbf{x}^2)$. We normalize the scale factor by the condition $a(0) = 1$, with $\eta = 0$ corresponding to the end of inflation. The number density of particles created in a time-varying cosmological background may be written as

$$n_X = \frac{1}{2\pi^2 a^3} \int |\beta_k|^2 k^2 dk \ , \tag{1}$$

where β_k are the Bogoliubov coefficients, which relate ''in'' and ''out'' mode functions, and k is the co-moving momentum. Massless conformally coupled quanta (for scalars this means that $\xi = 1/6$ in the direct coupling to the curvature) are not created. For massive particles conformal invariance is broken. Therefore, for the power-law (e.g., matter- or radiation-dominated) period of expansion of the Universe, one expects on dimensional grounds that $n_X \propto m_X^3/a^3$ at late times. Indeed, it was found in Ref. 12 that

$$n_X \approx 5.3 \times 10^{-4} m_X^3 (m_X t)^{-3/2} \tag{2}$$

for the radiation-dominated Universe, and $n_X \propto m_X^3 (m_X t)^{-3q}$ for $a(t) \propto t^q$. Note that all particle creation occurs at $mt \simeq qm/H \lesssim 1$. When $mt \ll 1$, the number density of created particles remains at the constant level $n_X = m_X^3/24\pi^2$ independently of q (Ref. 12), while for $qm/H \gg 1$ the particle creation is negligible. Here H is the Hubble constant, $H \equiv \dot{a}/a$.

For the radiation-dominated Universe one finds $\Omega_X \sim (m_X^2/M_{Pl}^2)\sqrt{m_X t_e}$, where t_e is the time of equal densities of radiation and matter in the $\Omega = 1$ Universe. This gives $\Omega_X \sim m_9^{5/2}$, where $m_9 \equiv m_X/10^9$ GeV. Stable particles with $m_X \gtrsim 10^9$ GeV will overclose the Universe even if they were created from the vacuum during the regular Friedmann radiation-dominated stage of the evolution. (It is possible to separate the vacuum creation from the creation in collisions in plasma, since X particles may be effectively sterile.)

However, this restriction will not be valid if the evolution of the Universe, as it is believed, was more complicated than the simple radiation-dominated expansion from a singularity. The Hubble constant may have never exceeded m_X, which is the case of inflationary cosmology, $H(0) \approx m_\phi$. Moreover, compared to the case considered above, the density of X particles created during inflation is additionally diluted by the late entropy release in reheating processes after inflation.

Particle creation from vacuum fluctuations during inflation (or in the de Sitter space) has been extensively studied (see, e.g., Refs. 13 and 14). The characteristic quantity which is usually cited, namely the variance $\langle X^2 \rangle$ of the field, is defined by an expression similar to Eq. (1). In the typical case $\alpha_k \approx -\beta_k$ the difference reduces to a factor $2\sin^2(\omega_k \eta)/\omega_k$ in the integrand, where $\omega_k^2 = k^2 + a^2 m_X^2$. If $m_X \sim H(0) \approx m_\phi$, we find using dimensional arguments that $n_X = C m_\phi^3/2\pi^2 a^3$, where the coefficient C is expected to be somewhat smaller than unity. Both fermions and bosons are produced by this mechanism, the exact numerical value of C being dependent on the spin statistics. In general, C is a function of the ratio $H(0)/m_X$, of the self-coupling of X, and of the coupling constant ξ and depends on details of the transition between the inflationary and matter-dominated (or radiation-dominated) phases, etc. For example, for a scalar Bose field with minimal

coupling to the curvature one has $\langle X^2\rangle = 3H(0)^4/8\pi^2 m_X^2$ if $m_X \ll H(0)$.[13,14] For a massless self-interacting field $\langle X^2\rangle \approx 0.132 H(0)^2/\sqrt{\lambda}$ (Ref. 15). C is expected to decrease exponentially when $m_X > m_\phi$. Particle creation in the case of a Hubble-dependent effective mass, $m_X(t) \propto H(t)$, was considered in Ref. 16.

Let us estimate the present-day number density of X particles. We consider a massive inflaton, $V(\phi) = m_\phi^2 \phi^2/2$. In this case inflation is followed by the matter-dominated stage. If the theory includes the presence of light bosons, $m_B \ll m_\phi$, even relatively weakly coupled to the inflaton, $g^2 \gtrsim 10^4 m_\phi^2/M_{Pl}^2 \sim 10^{-8}$, this matter-dominated stage will not last long: the inflaton will decay via parametric resonance, and radiation domination will follow. This happens typically when the energy density in the inflaton oscillations is red-shifted by a factor $r \approx 10^{-6}$ compared to the value $m_\phi^2 M_{Pl}^2$ (Refs. 9 and 10). Matter is still far from being in thermal equilibrium, but it is nevertheless convenient to characterize this radiation-dominated stage by an equivalent temperature, $T_* \sim r^{1/4}\sqrt{m_\phi M_{Pl}}$. At this moment the ratio of the energy density in X particles to the total energy density retains its value reached at the end of inflation, $\rho_X/\rho_R \approx C\, m_\phi m_X/2\pi^2 M_{Pl}^2$. Later on this ratio grows as $\propto T/T_*$ and reaches unity at $T = T_{eq}$, where

$$T_{eq} = \frac{C r^{1/4}}{2\pi^2}\left(\frac{m_\phi}{M_{Pl}}\right)^{3/2} m_X . \tag{3}$$

Using the relation $T_{eq} = 5.6\Omega_X h^2$ eV we find that $10^{-12} \lesssim \Omega_X \lesssim 1$ if

$$10^{-23} \lesssim C r^{1/4} m_X/m_\phi \lesssim 10^{-11} . \tag{4}$$

For m_X of the order of a few times m_ϕ this condition can be easily satisfied, since the coefficient C is exponentially small. This condition may be satisfied even for $m_X \sim m_\phi$, since the coefficient $r^{1/4}$ (or the equivalent reheating temperature) might be small, too.

Our hypothesis has unique observational consequences. If UHE cosmic rays are indeed due to the decay of superheavy particles which were produced from vacuum fluctuations during inflation, there has to be a new sharp cutoff in the cosmic ray spectrum at energies somewhat smaller than m_X. Since the number density n_X depends exponentially upon m_X/m_ϕ, the position of this cutoff is fixed and can be predicted to be near $m_\phi \approx 10^{13}$ GeV, and the shape of the cosmic ray spectrum beyond the GZK cutoff is of a quite generic form following from the QCD quark/gluon fragmentation. The Pierre Auger Project installation[17] may prove to be able to discover this fundamental phenomenon.

We conclude that observations of UHE cosmic rays can probe the spectrum of elementary particles in the superheavy range and can give an unique opportunity for investigation of the earliest epoch of evolution of the Universe, starting with the amplification of vacuum fluctuations during inflation through fine details of gravitational interaction and down to the physics of reheating.

When our paper was at the very end of completion we became aware of the quite recent paper by Chung, Kolb, and Riotto,[18] where similar problems of superheavy dark matter creation were considered.

We are grateful to S. Khlebnikov for helpful discussions. V. A. Kuzmin and I. I. Tkachev thank Theory Division at CERN for hospitality where the major part of this

work was done. The work of V. K. was supported in part by the Russian Fund for Fundamental Research under Grant 95-02-04911a. I. I. T. was supported in part by the U. S. Department of Energy under Grant DE-FG02-91ER40681 (Task B) and by the National Science Foundation under Grant PHY-9501458.

[a)]e-mail: kuzmin@ms2.inr.ac.ru
[b)]e-mail: tkachev@physics.purdue.edu

---

[1] K. Greisen, Phys. Rev. Lett. **16**, 748 (1966); G. T. Zatsepin and V. A. Kuzmin, JETP Lett. **4**, 78 (1966).
[2] N. Hayashida, K. Honda, M. Honda *et al.*, Phys. Rev. Lett. **73**, 3491 (1994); D. J. Bird *et al.*, Astrophys. J. **424**, 491 (1994); **441**, 144 (1995); T. A. Egorov *et al.*, in *Proceedings of the Tokyo Workshop on Techniques for the Study of Extremely High Energy Cosmic Rays*, edited by M. Nagano, ICRR, University of Tokyo, 1993.
[3] G. R. Farrar, Phys. Rev. Lett. **76**, 4111 (1996); D. J. Chung, G. R. Farrar, and E. W. Kolb, http://xxx.lanl.gov/abs/astro-ph/9707036.
[4] C. T. Hill, Nucl. Phys. B **224**, 469 (1983); C. T. Hill, D. N. Schramm, and T. P. Walker, Phys. Rev. D **36**, 1007 (1987); G. Sigl, D. N. Schramm, and P. Bhattacharjee, Astropart. Phys. **2**, 401 (1994); V. Berezinsky, X. Martin, and A. Vilenkin, Phys. Rev. D **56**, 2024 (1997); V. Berezinsky and A. Vilenkin, http://xxx.lanl.gov/abs/astro-ph/9704257.
[5] V. A. Kuzmin and V. A. Rubakov, http://xxx.lanl.gov/abs/astro-ph/9709187.
[6] V. Berezinsky, M. Kachelriess, and A. Vilenkin, Phys. Rev. Lett. **79**, 4302 (1997).
[7] J. Ellis, J. E. Kim, and D. V. Nanopoulos, Phys. Lett. B **145**, 181 (1984).
[8] For a review and list of references see A. D. Linde, *Particle Physics and Inflationary Cosmology*, Harwood Academic, New York, 1990; E. W. Kolb and M. S. Turner, *The Early Universe*, Addison-Wesley, Reading, Mass., 1990.
[9] L. A. Kofman, A. D. Linde, and A. A. Starobinsky, Phys. Rev. Lett. **73**, 3195 (1994).
[10] S. Yu. Khlebnikov and I. I. Tkachev, Phys. Rev. Lett. **77**, 219 (1996); Phys. Lett. B **390**, 80 (1997); Phys. Rev. Lett. **79**, 1607 (1997); Phys. Rev. D **56**, 653 (1997).
[11] L. A. Kofman, A. D. Linde, and A. A. Starobinsky, Phys. Rev. D **56**, 3258 (1997).
[12] S. G. Mamaev, V. M. Mostepanenko, and A. A. Starobinskii, Zh. Éksp. Teor. Fiz. **70**, 1577 (1976) [Sov. Phys. JETP **43**, 823 (1976)].
[13] N. A. Chernikov and E. A. Tagirov, Ann. Inst. Henri Poincaré, **9A**, 109 (1968); E. A. Tagirov, Ann. Phys. **76**, 561 (1973); T. S. Bunch and P. C. W. Davies, Proc. R. Soc. London, Ser. A **360**, 117 (1978).
[14] A. D. Linde, Phys. Lett. B **116**, 335 (1982); A. A. Starobinsky, Phys. Lett. B **117**, 175 (1982); A. Vilenkin and L. H. Ford, Phys. Rev. D **26**, 1231 (1982); B. Allen, Phys. Rev. D **32**, 3136 (1985).
[15] A. A. Starobinsky and J. Yokoyama, Phys. Rev. D **50**, 6357 (1994).
[16] D. Lyth and D. Roberts, http://xxx.lanl.gov/abs/hep-ph/9609441.
[17] M. Boratav, for Pierre Auger Collaboration, *The Pierre Auger Observatory Project: An Overview*, in *Proceedings of the 25th International Cosmic Ray Conference*, Durban (1997), Vol. 5, p. 205.
[18] D. J. H. Chung, E. W. Kolb, and A. Riotto, http://xxx.lanl.gov/abs/hep-ph/9802238.

Published in English in the original Russian journal. Edited by Steve Torstveit.

Local energy density functional and density-dependent pairing in nuclear systems

S. A. Fayans and S. V. Tolokonnikov
Kurchatov Institute Russian Science Center, 123182 Moscow, Russia

E. L. Trykov
Institute of Physics and Power Engineering, 249020 Obninsk, Kaluga Region, Russia

D. Zawischa
Institut für Theoretische Physik, Universität Hannover, D-30060 Hannover, Germany

(Submitted 14 July 1998)
Pis'ma Zh. Éksp. Teor. Fiz. **68**, No. 4, 260–265 (25 August 1998)

An approach based on the local energy density functional method for describing the ground-state properties of superfluid nuclei is presented. A generalized variational principle is formulated which corresponds, in the weak pairing approximation, to a full treatment of the Hartree–Fock–Bogoliubov problem with an effective contact pairing interaction. The Gor'kov equations for generalized Green's functions are treated exactly in the coordinate-space representation. The method is used to calculate the differential observables including odd–even mass differences and odd–even effects in charge radii which turn out to be very sensitive to the density dependence of the effective pairing force. A better knowledge of this density dependence allows one to make predictions for the pairing gap at the Fermi surface as a function of nuclear matter density. © *1998 American Institute of Physics.* [S0021-3640(98)00216-3]

PACS numbers: 21.10.−k, 21.60.Jz, 26.60.+c

The study of pairing correlations is currently one central issue in nuclear structure physics and nuclear astrophysics. For example, the superfluidity of neutron matter is expected to play an essential role in neutron stars,[1] while pairing in neutron-rich nuclei is of importance in a domain close to the drip line[2] and also in light halo nuclei.[3] An effective nucleon–nucleon interaction in the pairing channel suitable for nuclear structure calculations and for obtaining an accurate value of the pairing energy gap in infinite matter has not yet been well established. The major difficulties are connected with consistent allowance for the in-medium renormalizations[4,5] and, particularly in nonuniform systems, for the finite-range and nonlocal effects[6] which should be calculated in a reliable way to elucidate the proper dependence of the effective force on the density ρ and its gradients. At present the pairing gap can not be obtained on a satisfactory level from first-principle approaches with a bare *NN* interaction. The empirical information gained from the studies of laboratory nuclei seems to be indispensable in this respect. The presently most successful *simultaneous* description of the *bulk* nuclear properties, such as

binding energies and radii, is achieved with phenomenological ρ-dependent forces (e.g., Refs. 7 and 8), and so the density dependence of the effective interaction in the particle–hole channel is now fairly well established. In other words, the Hartree–Fock (HF) part of the energy density functional (EDF) is more or less known, though, as one may notice, considerable effort is still continuing to optimize this part.[9] On the same grounds, one would expect that a *simultaneous* description of the *differential* observables, such as odd–even effects in masses and radii, would shed light on the ρ dependence of the effective interaction in the particle–particle (pp) channel and on the pairing part of the EDF.

To reveal the form of Δ as a function of ρ through the ρ dependence of the underlying effective pairing force, one should analyze the observed changes of the geometrical characteristics of nuclei, first of all the odd–even staggering in charge radii.[10] This point may be illustrated by considering how the density changes when the pairing gap appears in nuclear matter.[11] It turns out that the density is sensitive to the derivative $d\Delta/dx$ near the saturation point $\rho \approx 0.16$ fm^{-3}. A negative slope in Δ causes a decrease of ρ, i.e., an expansion of the system. In finite systems this effect leads to an increase of the radii, as has been confirmed by self-consistent EDF calculations.[11–13] Amplified ρ-dependent variations of Δ in odd systems through suppression of the anomalous density by the blocking effect causes an enhancement of the odd–even staggering in radii.[10]

Here we present an EDF approach based on the general variational principle applied to the EDF with a fixed energy cutoff $\epsilon_c > \epsilon_F$ (ϵ_F is the Fermi energy). It involves an integration in the complex energy plane of the Green's functions obtained by exact solution of the coordinate-space Gor'kov equations. This technique is appropriate for the correct treatment of the coupling with the particle continuum, especially in weakly bound nuclei.[14] We extend this approach to systems with odd particle number by using the uniform filling approximation. Compared to Refs. 11, 12, and 15, where the calculations were done mostly in the HF+Bardeen–Cooper–Schrieffer (HF+BCS) framework, the approach formulated here corresponds to a full treatment of the Hartree–Fock–Bogoliubov (HFB) problem and permits direct comparison of the pairing gap extracted from the analysis of nuclear data with nuclear matter calculations.

The energy E of a superfluid nucleus is given by a functional of the generalized density matrix $\hat{R}$, which contains both a normal component $\hat{\rho}$ and an anomalous component $\hat{\nu}$:

$$E[\hat{R}] = E_{\rm kin}[\hat{\rho}] + E_{\rm int}[\hat{\rho}, \hat{\nu}] , \tag{1}$$

where $E_{\rm kin}[\hat{\rho}] = {\rm Tr}(t\hat{\rho})$, and $E_{\rm int}[\hat{\rho}, \hat{\nu}] = E_{\rm int(normal)}[\hat{\rho}] + E_{\rm anom}[\hat{\rho}, \hat{\nu}]$. The anomalous energy $E_{\rm anom}$ is chosen such that it vanishes in the limit $\nu \to 0$. The weak-pairing approximation $|\overline{\Delta}| \ll \epsilon_F$, which is generally the case for nuclear systems, is assumed. That means we need to retain only the first-order term $\sim \nu^2$ in the anomalous part of the EDF:

$$E_{\rm anom}[\hat{\rho}, \hat{\nu}] = \frac{1}{4}(\hat{\nu}^{\dagger} \hat{\mathcal{F}}_a^{pp}[\hat{\rho}] \hat{\nu}) , \tag{2}$$

where $\hat{\mathcal{F}}_a^{pp}$ is an antisymmetrized effective interaction in the pp channel and the parentheses imply integration and summation over all variables. To calculate the ground state properties, one can now use the general variational principle with two constraints,

$$\langle \mathrm{HFB}|\hat{N}(\mu)|\mathrm{HFB}\rangle \equiv N(\mu)=N, \quad \hat{R}^2=\hat{R}\,, \tag{3}$$

leading to the variational functional of the form

$$I[\hat{R}]=E[\hat{R}]-\mu N(\mu)-\mathrm{Tr}\hat{\Lambda}(\hat{R}-\hat{R}^2)\,, \tag{4}$$

where N is the particle number, μ the chemical potential, and $\hat{\Lambda}$ the matrix of Lagrange parameters (see, e.g., Ref. 16).

The anomalous energy (2) can be calculated if one knows a solution of the gap equation for the pairing field $\hat{\Delta}$ and the anomalous density matrix $\hat{\nu}$. In general, the gap equation is nonlocal, and its solution (starting, for example, from a realistic bare NN interaction[6,5]) poses serious problems. It can be shown that in the case of weak pairing $|\overline{\Delta}| \ll \epsilon_F$, the EDF method and the general variational principle can be used with an effective contact density-dependent pairing interaction. The formal development by using the Green's function formalism is described in detail in our forthcoming paper.[17] Here we give only a brief account of the main issues.

We introduce an arbitrary cutoff ϵ_c in energy space, but such that $\epsilon_c > \epsilon_F$, and split the generalized density matrix into two parts, $\hat{R}=\hat{R}_c+\delta_c\hat{R}$ where $\delta_c\hat{R}$ comes from the integration over energies $|\epsilon|>\epsilon_c$. The gap equation is renormalized to yield

$$\hat{\Delta}=\frac{1}{2}\mathcal{F}^{\xi}_{a}\hat{\nu}_c\,, \tag{5}$$

where $\hat{\nu}_c$ is the cutoff anomalous density matrix, and $\mathcal{F}^{\xi}_{a}$ is the effective antisymmetrized pairing interaction in which the contribution coming from the energy region $|\epsilon|>\epsilon_c$ is included by renormalization.

For homogeneous infinite matter it is shown that the variational function $E-\mu N$ does not change in first order in $\hat{\Delta}^2$ upon variation with respect to $\delta_c\hat{R}$. The total energy of the system and the chemical potential also remain the same if one imposes the particle number constraint (3) for the cutoff functional. To a good approximation, as was discussed in Ref. 17, this should be also valid for finite nuclei.

Such an outcome may be understood by noting that the major pairing effects are developed near the Fermi surface and the pairing energy is defined by a sum concentrated near the Fermi surface (see, e.g., Ref. 16). In infinite matter the pairing energy per particle is $E_{\mathrm{pair}}/N=-3\Delta^2(k_F)/8\epsilon_F$. It follows that, with the cutoff EDF, this leading pairing contribution to the energy of the system is taken into account exactly. Thus the nuclear ground state properties can be described by applying the general variational principle to minimize the cutoff functional, which has exactly the same form as (4) with the constraint (3) but with $\hat{R}$ replaced by $\hat{R}_c$. Recalling now the Hohenberg–Kohn theorem,[18] we specify that the EDF can be chosen to be of a local form, i.e., dependent on the normal and anomalous local real densities $\rho(\mathbf{r})$ and $\nu_c(\mathbf{r})$. Then the anomalous energy acquires the simple form

$$E^{c}_{\mathrm{anom}}[\rho_c,\nu_c]=\int d\mathbf{r}\,\nu^{*}_c(\mathbf{r})\mathcal{F}^{\xi}(\mathbf{r};[\rho_c])\,\nu_c(\mathbf{r})\,. \tag{6}$$

This corresponds to the multiplicative gap equation

$$\Delta(\mathbf{r}) = \mathcal{F}^{\xi}(\mathbf{r};[\rho_c])\,\nu_c(\mathbf{r})\,. \tag{7}$$

Having found the pairing field $\Delta(\mathbf{r})$ and the mean-field potential $U(\mathbf{r})$, we can solve the Gor'kov equations exactly by using the coordinate-space technique. The generalized Green's function obtained this way can be integrated over energy up to ϵ_c to yield both the normal and anomalous densities ρ_c and ν_c, which are then used to compute the energy of the system. We stress that our approach does not imply a cutoff of the basis, since the general variational principle is formulated with a ''cutoff'' local functional from which the ground state characteristics of a superfluid system may be calculated by using the generalized Green's function expressed through the solutions of the Bogoliubov equations at the stationary point. To construct the normal and anomalous densities that appear in this local functional, only those solutions from the whole set are needed which corresponds to the eigenenergies E_α of the HFB Hamiltonian, which is a matrix of the first variational derivatives of the EDF, up to the cutoff $\epsilon_c > \epsilon_F$. In contrast to the BCS-like methods in which the presence of an unphysical ''particle gas'' is almost unavoidable, the coordinate-space Gor'kov (or HFB) equations[14] for finite systems naturally give a localized wave function with the correct asymptotic behavior for the normal and anomalous densities.[19,20]

From the Gor'kov equations, after separating angular variables, one gets the following equation for the generalized radial Green's function $\hat{g}_{jl}$

$$\begin{pmatrix} \epsilon - h_{jl} + \mu & -\Delta \\ -\Delta & \epsilon + h_{jl} - \mu \end{pmatrix} \hat{g}_{jl}(r_1, r_2; \epsilon) = \begin{pmatrix} \delta(r_1 - r_2) & 0 \\ 0 & \delta(r_1 - r_2) \end{pmatrix}, \tag{8}$$

where h_{jl} is the single-quasiparticle HF Hamiltonian in the jl channel. The solution of this matrix equation can be constructed by using the set of four linearly independent solutions which satisfy the homogeneous system obtained from (8) by setting the right-hand side to zero and which obey the physical boundary conditions.[14]

The poles (if any) of the generalized Green's function are determined by the zeroes of the generalized Wronskian of the four linearly independent solutions, i.e., from the condition $W(\epsilon) = 0$, which gives the discrete spectrum of the Bogoliubov quasiparticle states. The spectrum is symmetric about $\epsilon = 0$. For bound systems $\mu < 0$. If the system is finite one expects $\Delta_\infty = 0$; otherwise the system would be unstable with respect to two-particle emission. It follows then that the spectrum is discrete within the energy region $|\epsilon| < |\mu|$ (in which case $\hat{g}_{jl}$ is a real function on the axis $\mathrm{Im}\,\epsilon = 0$) and continuous if $|\epsilon| > |\mu|$ (in which case $\hat{g}_{jl}$ is a complex function). These features are reflected in the upper panel of Fig. 1, where the branch cuts are shown by the heavy lines extending symmetrically to the left and to the right from the points $\pm\mu$, respectively. The case with only branch cuts and no poles corresponds to a drip-line even nucleus. Integrating $\hat{g}_{jl}$ along the upper contour C of Fig. 1, one obtains the radial part of the generalized density matrix for a system with even N.

For an odd system the contour for integrating the generalized Green's function in the complex energy plane must be modified. Suppose that the addition of an odd particle leads to the appearance of a quasiparticle with energy E_{α_0} in the ground state of the system and that E_α corresponds to a certain eigenenergy of Eq. (8) and belongs to the discrete spectrum, i.e., $|\mu| > E_{\alpha_0} > 0$ ($\alpha_0 = n_0 j_0 l_0 m_0$ is the usual set of single-particle

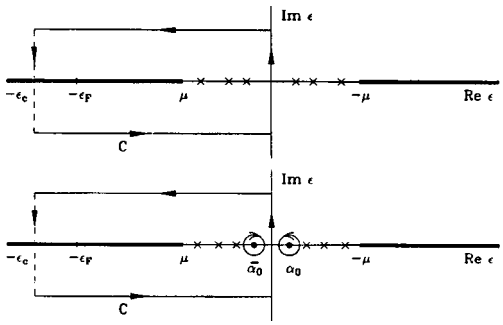

FIG. 1. The contour C in the energy plane for integration of the generalized Green's function for determining the generalized density matrix (top: for even nuclei, bottom: for odd nuclei). The crosses show the positions of the single-particle poles; the heavy lines represent the branch cuts on the $\mathrm{Im}\epsilon=0$ axis, where the energy spectrum is continuous; μ is the chemical potential; ϵ_F is the Fermi energy; ϵ_c is the energy cutoff (see text). The positions α_0 and $\bar{\alpha}_0$ of the poles for the odd quasiparticle are shown by heavy dots. Note that the paths around these poles are traversed in opposite directions.

quantum numbers). As illustrated in Fig. 1, E_{α_0} is located in the vicinity of the point $\epsilon=0$. Generally, E_{α_0} is of the order of $\bar{\Delta}$, the average matrix element of the pairing potential on the the Fermi surface. The case $E_{\alpha_0}\approx-\mu$ determines the position of the drip line for odd nuclei. The lower contour in Fig. 1 clearly illustrates the blocking effect: the presence of the odd particle in the level α_0 prevents it from participating in the pairing correlations, because in this case the ''conjugate'' level $\bar{\alpha}_0$ for an odd system should be empty. The nucleon separation energies S_n are determined by the position of the poles close to $\epsilon=0$. As is easily understood from Fig. 1, since these separation energies are measured from the continuum threshold $\epsilon=-\mu$, for an odd system one gets $S_n^{\mathrm{odd}}\approx-\mu-E_{\alpha_0}$, and, for an even system, $S_n^{\mathrm{even}}\approx-\mu+E_{\bar{\alpha}_0}$. Thus we have $S_n^{\mathrm{even}}-S_n^{\mathrm{odd}}\approx 2E_{\alpha_0}\approx 2\bar{\Delta}$, i.e., the familiar odd–even effect in nuclear masses.

The calculations were performed with the density functional DF3.[13] In the anomalous part of the EDF the ''gradient'' pairing force was used[12] (see Eq. (7))

$$\mathcal{F}^{\xi}(x)=C_0 f^{\xi}(x),\quad f^{\xi}(x)=f_{\mathrm{ex}}^{\xi}+h^{\xi}x^{q}+f_{\mathrm{grad}}^{\xi}r_0^2(\nabla x)^2\,, \tag{9}$$

where $C_0=308\ \mathrm{MeV\cdot fm^{-3}}$, $q=2/3$, and $x=(\rho_n+\rho_p)/2\rho_0$ is the isoscalar dimensionless density. The superscript ξ indicates that the interaction corresponds to an energy cutoff ϵ_c (in our case $\epsilon_c=40$ MeV while the Fermi energy $\epsilon_{0F}=36.6$ MeV).

Typical results obtained for the lead isotope chain are shown in Fig. 2. It is seen that the neutron separation energies S_n are described reasonably well with any set of parameters giving the ''experimental'' average gap at the Fermi surface, but the rms charge radii $\langle r^2\rangle_{\mathrm{ch}}^{1/2}$ and their staggering can be explained only if the pairing force (9) contains density dependence and if its parameters are taken in a certain ratio. The physics behind this is discussed in Ref. 12. The success in the simultaneous description of both observables, S_n and $\langle r^2\rangle_{\mathrm{ch}}^{1/2}$, in finite nuclei is due to the gradient term $\propto f_{\mathrm{grad}}^{\xi}\approx 1$. This term vanishes in infinite uniform matter. Now the sets of the other two deduced parameters $(f_{\mathrm{ex}}^{\xi}, h^{\xi})$ can be used to predict the pairing gap in nuclear matter. This can be done by solving the gap equation (7). The solution is given by

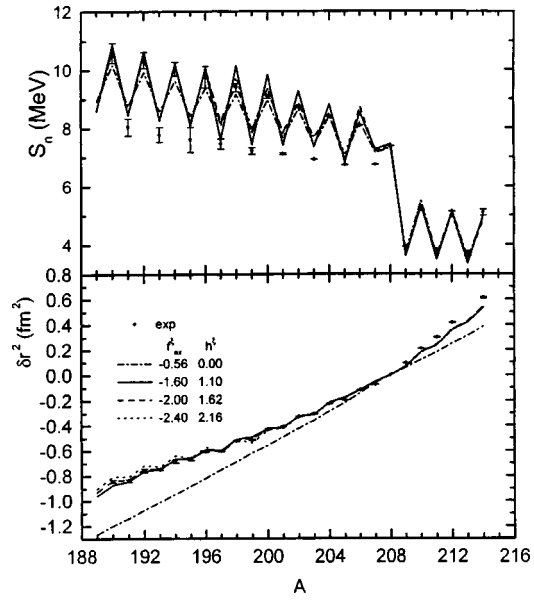

FIG. 2. Calculated neutron separation energies (top) and differences of mean squared charge radii (bottom) for lead isotopes with respect to ^{208}Pb as a reference nucleus in comparison with experimental data. All calculations are done self-consistently using the EDF method with different parameter sets of the pairing force of Eq. (9). The gradient strength $f^{\xi}_{\rm grad}=1$ for all sets except the case of ''constant'' pairing with $f^{\xi}_{\rm ex}=-0.56$.

$$\Delta(x)=8\,\epsilon_F(x)\,\sqrt{\frac{s(x)-1}{s(x)+1}}\exp\left(s(x)-2+\frac{2}{f^{\xi}(x)x^{1/3}}\right), \tag{10}$$

with $s(x)=\sqrt{1+\epsilon_c/\epsilon_F(x)}$ and $\epsilon_F=\epsilon_{0F}x^{2/3}$. The obtained pairing gap as a function of the Fermi momentum (to facilitate the comparison with nuclear matter calculations, e.g., Ref. 5) is shown in Fig. 3. The curve for ''constant'' pairing $f^{\xi}_{\rm ex}=-0.56$ stands by itself with a positive derivative everywhere. In this case no acceptable description of $\langle r^2\rangle^{1/2}_{\rm ch}$ is obtained (see Fig. 2). An interesting observation is that all sets of the deduced parameters which give a satisfactory description of S_n and $\langle r^2\rangle^{1/2}_{\rm ch}$ yield about the same value of $\Delta\approx 3.3$ MeV at $k_F\approx 1.16$ fm^{-3} (at ≈ 0.66 of the equilibrium density). These sets produce for $\Delta(k_F)$ the characteristic bell shape known from the calculations for infinite matter. Our preferred set which gives a slightly better fit compared to others is ($f^{\xi}_{\rm ex}=-1.6$, $h^{\xi}=1.10$). The corresponding pairing gap, shown by the solid curve in Fig. 3, turns out to be in qualitative agreement with the most recent calculations.[5]

The formulated approach based on the local energy density functional method with the coordinate-space technique is shown to be quite successful in describing the ground state properties of superfluid finite nuclear systems. The combined analysis of the differential observables such as neutron separation energies and isotopic shifts in charge radii with this approach holds forth the hope of constructing a universal density-dependent effective interaction which would allow one to predict pairing properties both for exotic nuclei very far from stability and for nuclear matter.

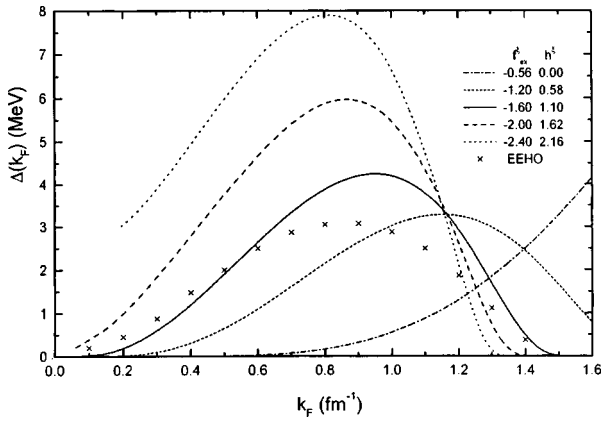

FIG. 3. Pairing gap at the Fermi surface in infinite nuclear matter as a function of the Fermi momentum for different parameter sets deduced from the EDF calculations for the lead isotopes. The crosses represent nuclear matter calculation from Ref. 5.

This work was supported in part by the Deutsche Forschungsgemeinschaft and by the Russian Fund for Fundamental Research through Grant 98-02-16979.

[1] C. J. Pethick and D. G. Ravenhall, Annu. Rev. Nucl. Part. Sci. **45**, 429 (1995).
[2] A. C. Müller and B. M. Sherill, Annu. Rev. Nucl. Part. Sci. **43**, 529 (1993).
[3] G. F. Bertsch and H. Esbensen, Ann. Phys. (N.Y.) **209**, 327 (1991).
[4] J. Wambach, T. L. Ainsworth, and D. Pines, Nucl. Phys. A **555**, 128 (1993).
[5] Ø. Elgarøy, L. Engvik, M. Hjorth-Jensen, and E. Osnes, Nucl. Phys. A **604**, 466 (1996).
[6] M. Baldo, U. Lombardo, E. E. Saperstein, and M. V. Zverev, Phys. Lett. B **350**, 135 (1995).
[7] D. Vautherin and D. M. Brink, Phys. Rev. C **5**, 626 (1972).
[8] J. Dechargé and D. Gogny, Phys. Rev. C **21**, 1568 (1980).
[9] E. Chabanat, P. Bonche, P. Hansel *et al.*, Nucl. Phys. A **627**, 710 (1997).
[10] U. Regge and D. Zawischa, Comments At. Mol. Phys. **23**, 257 (1989).
[11] S. A. Fayans, S. V. Tolokonnikov, E. L. Trykov, and D. Zawischa, Phys. Lett. B **338**, 1 (1994).
[12] S. A. Fayans and D. Zawischa, Phys. Lett. B **383**, 19 (1996).
[13] E. Krömer, S. V. Tolokonnikov, S. A. Fayans, and D. Zawischa, Phys. Lett. B **363**, 12 (1995).
[14] S. T. Belyaev, A. V. Smirnov, S. V. Tolokonnikov, and S. A. Fayans, Yad. Fiz. **45**, 1263 (1987) [Sov. J. Nucl. Phys. **45**, 783 (1987)].
[15] A. V. Smirnov, S. V. Tolokonnikov, and S. A. Fayans, Yad. Fiz. **48**, 1661 (1988) [Sov. J. Nucl. Phys. **48**, 995 (1988)].
[16] P. Ring and P. Schuck, *The Nuclear Many-Body Problem*, Springer, New York, 1980.
[17] S. A. Fayans, E. Krömer, S. V. Tolokonnikov *et al.*, to be submitted to Nucl. Phys. A.
[18] P. Hohenberg and W. Kohn, Phys. Rev. B **136**, 864 (1964).
[19] A. Bulgac, Preprint FT-194-1980, Central Institute of Physics, Bucharest, 1980.
[20] J. Dobaczewski, W. Nazarewicz, T. R. Werner *et al.*, Phys. Rev. C **53**, 2809 (1996).

Published in English in the original Russian journal. Edited by Steve Torstveit.

Four-photon polarization spectroscopy of water in a millimeter-wave radiation field

A. F. Bunkin, V. I. Grachev,[a)] G. A. Lyakhov, and A. A. Nurmatov
Institute of General Physics, Russian Academy of Sciences, 117942 Moscow, Russia

(Submitted 1 July 1998)
Pis'ma Zh. Éksp. Teor. Fiz. **68**, No. 4, 266–268 (25 August 1998)

Resonance (frequency 1.4 cm^{-1}) changes induced in the four-photon optical spectrum of water by a millimeter-wave electromagnetic field are observed experimentally. Comparison with the spectrum of ice in the range $0-2\ cm^{-1}$ shows that the action of such a field is of a structure-forming character. © *1998 American Institute of Physics.* [S0021-3640(98)00316-8]

PACS numbers: 33.20.Bx, 39.30.+w

Four-photon polarization spectroscopy (FPPS)[1,2] has made it possible to obtain newer results in the investigation of long-wavelength resonances of liquid water.[3,4] A triplet structure, apparently due to collective quasirotational modes of water molecules or dynamic molecular complexes, has been observed[5,6] in the range $10-100\ cm^{-1}$ by this method. The existence of a band near $6\ cm^{-1}$, observed previously in neutron scattering[4,8] and probably attributable to vibrations of the proton along the hydrogen bond, has been confirmed[7] by an optical method. Interference of the Brillouin and Kerr modes has been observed[9,10] by FPPS in the region $0-1\ cm^{-1}$.

Further investigations[9] in the Rayleigh line wing reveal another feature — a clearly distinguished peak near $1.4\ cm^{-1}$. Its presence in the spectrum of water cannot, at present, be reliably attributed to a definite physical mode. One possibility for making progress in the interpretation of this peak is to observe its behavior in response to a controllable external influence on a water medium.

The use of a resonance action appears to be most promising. Such an action is provided, in particular, by electromagnetic radiation at a wavelength of about 7 mm.

The experiment was performed on a previously developed setup.[5] The master oscillator consisted of a single-frequency YAG:Nd laser, whose radiation after three amplification cascades was converted to the second harmonic in thermally stabilized CDA crystals. Radiation at the third harmonic was used for pumping a narrow-band Coumarin-500 (Exciton Inc.) dye laser. The dye laser radiation (tuning range 483–565 nm), together with the second-harmonic radiation of the master laser ($\lambda = 532$ nm), served for parametric excitation of resonances of the medium in the range of frequency detunings from -1000 to $2000\ cm^{-1}$, including the region near $0\ cm^{-1}$, which makes it possible, for example, to study the low-frequency vibrational and librational resonances, relaxation of anisotropy (Rayleigh line wing), and the Brillouin lines. Good reproducibility of the detected four-photon spectra (not worse than 5%) is accomplished by completely auto-

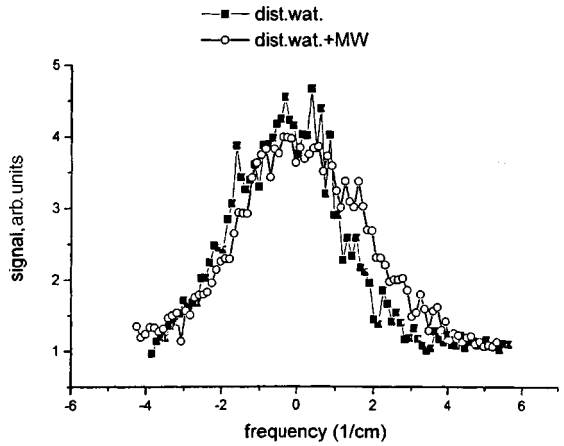

FIG. 1. Four-photon spectrum of water in the absence of an external field (■) and in the presence of irradiation by a 7.1 mm source (○).

mating the process of detecting and performing statistical analysis of the signal as well as by the high spectral and amplitude stability of the laser beams employed, which makes it possible to perform a detailed quantitative comparison of spectra obtained under different experimental conditions over a period of several years.

A modification of the serially produced Yav' generator[11] with working wavelengths 7.1 mm ($1.4\ \mathrm{cm}^{-1}$) and 5.6 mm ($1.8\ \mathrm{cm}^{-1}$) and power flux density from the radiating surface of the generator head of about $10\ \mathrm{mW/cm}^2$ was used as the source of the millimeter-wave radiation. The measurements were performed in twice-distilled deionized water.

The results of the measurements of the four-photon spectrum of distilled water in the absence of an external field as compared with the spectra obtained by simultaneously irradiating water (generator head 1 cm above the free surface of the water) by a millimeter-wave source show appreciable differences (Fig. 1). The effect of the millimeter wave field is to decrease the intensity of the spectrum near zero frequency by approximately 10%. Conversely, the peak at $1.4\ \mathrm{cm}^{-1}$ increases by $\sim 15\%$. The entire band shifts in the direction of positive frequency detunings by a fraction of an inverse centimeter, while the background level (frequencies above $4\ \mathrm{cm}^{-1}$) does not change. Significantly, irradiation of water at $5.6\ \mathrm{cm}^{-1}$ does not produce any appreciable changes in its four-photon spectrum. This fact rules out thermal action as the reason for the changes occurring in the spectrum, confirming that the action is of a resonance character.

We note that for the wavelength 7.1 mm the thickness of the skin layer of water with conductivity $\sigma \sim 75$ S/m equals about 0.4 mm. Water is opaque to millimeter-wave radiation, and the mechanism of the effect of this radiation on the four-photon optical spectrum, i.e., on the optical parameters of water in the interior of the cell, is nontrivial. Specifically, it cannot be attributed to a localized mode.

The FPPS of ice provides additional information. The spectrum of ice in this region (Fig. 2), obtained by the same method as in Ref. 4, actually shows the same, but much more pronounced, differences from the spectrum of liquid water as those induced by

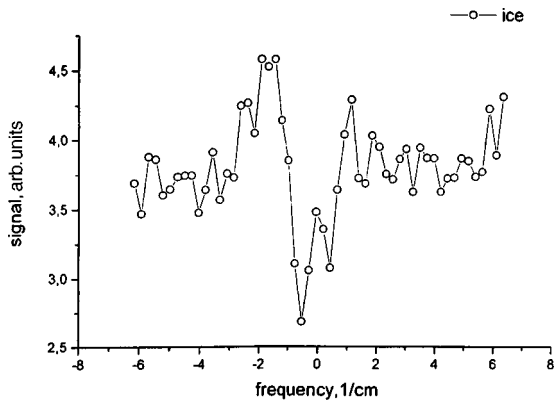

FIG. 2. Four-photon spectrum of ice.

millimeter-wave irradiation. The intensity of the ice spectrum near zero frequency decreases, while the intensity at 1.4 cm^{-1} increases, and in a manner such that their ratio is reversed: $I(1.4\ cm^{-1},\ \text{ice})/I(0,\text{ice})>1$, while $I(1.4\ cm^{-1},\ \text{water})/I(0,\text{water})<1$.

Comparing the data shown in Figs. 1 and 2 gives, in our opinion, a basis for hypothesing that the action of a millimeter-wave field on liquid water is of a structure-forming character. Being absorbed in the skin layer, millimeter-wave radiation apparently triggers a mechanism of mutual orientation of neighboring water molecules. The field of partial orientational ordering field that arises in this manner propagates to depths which are much greater than the thickness of the skin layer. Significantly, the corresponding scale of the changes is related to the value of the conductivity. This mechanism is qualitatively reminiscent of the mechanism of orientational ordering in liquid-crystal samples of finite length under prescribed conditions of mechanical treatment of their surface. Of course, in reference to water one can talk only about a dynamic ordering, and only with the tetrahedral motifs which are characteristic of water molecules.

We thank V. V. Kolesov (Institute of Radio Engineering and Electronics, Russian Academy of Sciences, Moscow) for providing the millimeter-wave radiation source and the materials.

[a)]e-mail: grant.k2peak@relcom.ru

[1] A. F. Bunkin, D. V. Mal'tsev, and K. O. Surskiĭ, JETP Lett. **47**, 657 (1988).
[2] A. F. Bunkin, S. A. Gnedoy, G. A. Lyakhov *et al.*, Opt. Acoust. Rev. **1**, 29 (1990).
[3] A. F. Bunkin, G. A. Lyakhov, A. A. Nurmatov, and A. V. Rezov, Izv. Ross. Akad. Nauk, Ser. Fiz. **59**, 12, 19 (1995).
[4] A. F. Bunkin, G. A. Lyakhov, A. A. Nurmatov, and N. V. Suyazov, *Laser Methods of Investigation of Water and Water Solutions* [in Russian] (Trudy IOFAN, Vol. 54), Nauka, Moscow, 1997, p. 5.
[5] A. F. Bunkin, G. A. Lyakhov, A. A. Nurmatov, and A. V. Rezov, Phys. Rev. B **52**, 9360 (1995).
[6] G. A. Lyakhov, Opt. Spektrosk. **78**, 917 (1995) [Opt. Spectrosc. **78**, 829 (1995)].
[7] A. F. Bunkin, G. A. Lyakhov, A. V. Rezov, and K. O. Sursky, J. Mod. Opt. **37**, 1155 (1990).
[8] D. Eisenberg and W. Kauzmann, *The Structure and Properties of Water*, Oxford University Press, New York, 1969.
[9] A. F. Bunkin, G. A. Lyakhov, A. A. Nurmatov, and N. V. Suyazov, Opt. Spektrosk. **82**, 638 (1997) [Opt. Spectrosc. **82**, 589 (1997)].

[10] A. F. Bunkin, G. A. Lyakhov, A. A. Nurmatov, and N. V. Suyazov, Appl. Phys. B **65**, 91 (1998).
[11] Yu. V. Dedik, N. A. Kruglyakov, T. B. Rebrova *et al.*, Elektron. Tekh. Ser. Elektronika SVCh **6**, 61 (1984).

Translated by M. E. Alferieff

Suppression of coherent inelastic Mössbauer scattering of synchrotron radiation at grazing angles of incidence

V. A. Belyakov[a)]

L. D. Landau Institute of Theoretical Physics, Russian Academy of Sciences, 117334 Moscow, Russia

(Submitted 30 June 1998)
Pis'ma Zh. Éksp. Teor. Fiz. **68**, No. 4, 269–274 (25 August 1998)

Coherent inelastic Mössbauer scattering (CIMS) of synchrotron radiation (SR) by an isotopic interface (a flat interface between two regions of matter differing in the concentration of the Mössbauer isotope) at grazing angles of incidence of the SR beam is investigated theoretically. The qualitative features of CIMS as compared with conventional optics at small grazing angles of the SR beam are determined. Specifically, it is shown that for CIMS by an isotopic interface, instead of the phenomenon of total external (internal) reflection well known in optics, total suppression of reflection of the CIMS beam occurs at grazing angles of the SR beam less than a critical angle, and a maximum of the transmission and reflection at distinguished CIMS frequencies appears near the critical angle. © *1998 American Institute of Physics.* [S0021-3640(98)00416-2]

PACS numbers: 76.80.+y, 07.85.Qe, 78.70.Ck

Introduction

In view of recent progress in Mössbauer spectroscopy using synchrotron radiation (SR) in investigations of phonon spectra of condensed media,[1–3] it is of topical interest to make detailed investigations of the Mössbauer optics of synchrotron radiation. Coherent inelastic Mössbauer scattering (CIMS) of SR, specifically, forward scattering, which is investigated theoretically in Ref. 4, is of special interest. In Ref. 4 it was shown that of special interest for the Mössbauer optics of SR is CIMS, in the first stage of which — resonance nuclear absorption of a SR photon — the absorption process is accompanied by the emission or absorption of a lattice phonon, while the second stage of the scattering, i.e., re-emission of the photon, occurs without recoil, specifically, without the absorption or emission of phonons. This CIMS channel leads to pumping of radiation from a wide SR line into a narrow Mössbauer emission line.

An isotopic interface (IIF) is a convenient object for investigating Mössbauer scattering of SR. The point is that for radiation which does not undergo resonance interaction with Mössbauer nuclei this interface simply is not manifested in the optical properties, since the optical characteristics of matter, which are determined by the interaction of

radiation with electrons, are identical on both sides of the IIF. An IIF separates spatial regions of matter with different optical characteristics only for a narrow spectral band of SR near the Mössbauer transition frequencies, where resonance interaction of the SR with Mössbauer nuclei is significant. In this spectral region, all optical phenomena known in optics for a dielectric interface are manifested in the CIMS. For this reason, the optics of an IIF is of interest for experiments studying the interaction of SR with Mössbauer nuclei,[5] specifically, Mössbauer filtering of SR, since it makes it possible to eliminate the background due to the interaction of SR with the electrons of the material.

The present letter is devoted to analysis of the optical characteristics of CIMS by an isotopic interface in the region of total external (internal) reflection (TE(I)R), i.e., in the region of grazing angles of incidence of the SR beam on the IIF. The emphasis is on the analysis of the CIMS component that corresponds to the resonance nuclear scattering of SR photons, in which process the creation or annihilation of lattice phonons occurs in the stage of absorption of the primary photon, while the stage of re-emission of the photon by the nucleus occurs without the participation of phonons. It is shown that the optics of CIMS in the region of grazing angles of incidence of the SR beam is qualitatively different from the conventional optics. In contrast to the latter, in the case of CIMS suppression of reflection of the CIMS beam as well as suppression of the refracted CIMS beam propagating behind the IIF occur at grazing angles of incidence of the SR. In addition, the angular regions of suppression of reflection and propagation of the CIMS beam behind the IIF are not the same in the general case.

Basic equations

Let us consider the CIMS processes occurring as a SR pulse propagates in a sample containing nuclei of a Mössbauer isotope, i.e., nuclear resonance scattering processes accompanied by the creation or annihilation of lattice phonons. The generation of CIMS is described by the inhomogeneous Maxwell equation[4]

$$-\nabla\times\nabla\times\mathbf{E}_1=c^{-2}(\epsilon_0+\epsilon_1)\partial^2\mathbf{E}_1/\partial t^2+\chi^N\mathbf{E}_0(\omega_s,z)\,\delta(z-v_g t), \tag{1}$$

where ϵ_0 is the dielectric constant in the absence of the nuclear interaction and ϵ_1 is the correction to it due to the nuclear interaction, χ^N is the analog of the nonlinear susceptibility, well known from nonlinear optics,[4] ω_s is the frequency of the SR, v_g is the group velocity of the SR pulse, and z is the coordinate in the direction of propagation of the pulse, while the electromagnetic field in the sample is represented as a sum of two components $\mathbf{E}=\mathbf{E}_0+\mathbf{E}_1$, where $\mathbf{E}_0$ is the unperturbed SR field and $\mathbf{E}_1$ is a perturbation due to the interaction of the SR with the Mössbauer nuclei. To solve Eq. (1) we shall assume that only the process of absorption of the primary SR photon occurs with recoil, while re-emission of secondary photons by the nuclei occurs without recoil.

To describe the CIMS on an IIF or on a slab bounded by two IIFs, the solution of Eq. (1) must satisfy boundary conditions on the IIF or on the two IIFs in the case of a slab (see Fig. 1). Assuming for simplicity that the density of the Mössbauer isotope on one side of the IIF equals zero, we shall seek the solution for the CIMS field in the form

$$\mathbf{E}_r\exp(i\mathbf{k}_r\cdot\mathbf{r}) \quad \text{for } z>0,\ \epsilon_1=0;$$

$$\mathbf{E}_t\exp(i\mathbf{k}_t\cdot\mathbf{r}) \text{ for } z<-L,\ \epsilon_1=0,$$

$$\mathbf{E}_p\exp(i\mathbf{k}_p\cdot\mathbf{r})+\mathbf{E}_f\exp(i\mathbf{k}\cdot\mathbf{r})+\mathbf{E}_{2r}\exp(i\mathbf{k}_{2r}\cdot\mathbf{r}) \quad \text{for } 0>z>-L,\ \epsilon_1\neq 0, \tag{2}$$

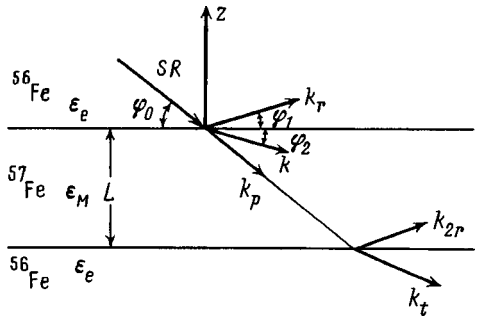

FIG. 1. Illustration of the geometry of CIMS at an isotopic interface.

where $\mathbf{k}_r$ and $\mathbf{k}_t$ are wave vectors of the CIMS photons which are reflected and transmitted by the slab, respectively; $\mathbf{k}$ and $\mathbf{k}_{2r}$ are the wave vectors of the transmitted beam in the slab and the beam reflected from the second IIF in the slab; $\mathbf{k}_p$ is the wave vector in the particular solution of the inhomogeneous equation (1); and, $\mathbf{E}_r$, $\mathbf{E}_t$, $\mathbf{E}_p$, $\mathbf{E}_f$, and $\mathbf{E}_{2r}$ are the amplitudes of the corresponding plane waves.[4] The moduli of the wave vectors are determined by the frequency of the CIMS photons and the dielectric constants:[4]

$$k_r = k_t = (\omega/c)(\epsilon_e)^{1/2}, \quad k = k_{2r} = (\omega/c)(\epsilon_M)^{1/2}, \quad k_p = (\omega/c)(\epsilon_e)^{-1/2}, \tag{3}$$

where ϵ_M and ϵ_e are the dielectric constants at the radiation frequencies near Mössbauer resonance on the side of the IIF containing the Mössbauer isotope and on the side of the IIF which does not contain the Mössbauer isotope.

Boundary conditions

On account of the boundary conditions on the wave vectors the tangential components of all wave vectors are identical and can be expressed in terms of the grazing angle of the SR beam as $k_p \cos\varphi_0$ (see Fig. 1).

The boundary conditions on the electric and magnetic fields in the case where the linear polarization of the waves is orthogonal to the scattering plane yield the following system of equations for the wave amplitudes:

$$\begin{aligned}
&\mathbf{E}_p + \mathbf{E}_f + \mathbf{E}_{2r} = \mathbf{E}_r,\\
&\mathbf{k}_{pz}\cdot\mathbf{E}_p + \mathbf{k}_z\cdot\mathbf{E}_f + \mathbf{k}_{2rz}\cdot\mathbf{E}_{2r} = \mathbf{k}_{rz}\cdot\mathbf{E}_r,\\
&\mathbf{E}_p\exp(i\mathbf{k}_{pz}L) + \mathbf{E}_f\exp(i\mathbf{k}_z L) + \mathbf{E}_{2r}\exp(i\mathbf{k}_{2rz}L) = \mathbf{E}_t\exp(i\mathbf{k}_{tz}L),\\
&\mathbf{k}_{pz}\cdot\mathbf{E}_p\exp(i\mathbf{k}_{pz}L) + \mathbf{k}_z\cdot\mathbf{E}_f\exp(i\mathbf{k}_z L) + \mathbf{k}_{2rz}\cdot\mathbf{E}_{2r}\exp(i\mathbf{k}_{2rz}L) = \mathbf{k}_{tz}\cdot\mathbf{E}_t\exp(i\mathbf{k}_{tz}L),
\end{aligned} \tag{4}$$

where the index z labels the normal components of the wave vectors.

Isotopic interface

To describe CIMS by an IIF it is sufficient to use the first pair of equations of the system (4), setting in it the amplitude $\mathbf{E}_{2r}$ equal to zero. The boundary conditions on the wave vectors yield (see Fig. 1)

$$\cos\varphi_1 = \cos\varphi_0 / \epsilon_e , \tag{5}$$

for the angle of ''reflection'' of the ICMS beam and

$$\cos\varphi_2 = (\epsilon_e \epsilon_M)^{-1/2} \cos\varphi_0 \tag{6}$$

the angle of refraction φ_2. We shall consider theses expressions for extremely small angles of incidence of the primary SR beam.

Since the denominator ϵ_e in expression (5) is less than 1, there always exists a critical value of the grazing angle φ_s of the SR beam such that $\varphi_1 = 0$, i.e., the reflected CIMS beam propagates along the IIF, while for grazing angles φ_0 less than the critical angle φ_s there is no CIMS beam reflected from the IIF.

Since the denominator $(\epsilon_e \epsilon_M)^{1/2}$ in expression (6) is less than 1, except possibly at frequencies close to the Mössbauer resonance frequency, there exists a certain critical value of the grazing angle φ_c of the SR beam for which $\varphi_2 = 0$, i.e., the refracted CIMS beam propagates along the IIF, while for grazing angles φ_0 less than the critical value φ_c there is no CIMS beam refracted by the IIF.

From Eqs. (5) and (6) we have for the critical angles for the reflection and refraction of the CIMS beam

$$\cos\varphi_s = \varphi_e ; \quad \varphi_s = [2(1-\epsilon_e)]^{1/2} = (\omega_p / \omega)^{1/2}, \tag{7}$$

$$\cos\varphi_c = (\epsilon_e \epsilon_M)^{1/2}; \quad \varphi_c = (2(1-(\epsilon_e \epsilon_M)^{1/2})^{1/2}, \tag{8}$$

where ω_p is the plasma frequency.

Therefore, in the region of small grazing angles of the SR beam — the region which in conventional optics corresponds to the ordinary phenomenon of TE(I)R — the behavior of the CIMS is completely different from that of TE(I)R. Specifically, reflection of the CIMS beam from an IIF is completely suppressed, so that the corresponding region of angles for CIMS corresponds not to TE(I)R but rather to total suppression of reflection (TSR), and it would be correct to replace the acronym TE(I)R by TSR.

In contrast to ordinary optics, in the case of CIMS the angular regions of TSR and of the absence of a beam penetrating behind the IIF are different, since they are determined by different conditions (see Fig. 2). It is important that the existence of the CIMS beam propagating behind the IIF depends on the CIMS frequency. For sufficiently high Mössbauer isotope density, such that in the region of frequencies near the Mössbauer resonance frequency the quantity $(\epsilon_e \epsilon_M)^{1/2}$ can reach and exceed 1, there is no critical angle for the propagation of a CIMS beam at the corresponding frequencies behind the IIF, i.e., for these frequencies a CIMS beam propagates behind the IIF for any angles of incidence of the SR beam. Specifically, the fact that there is a CIMS beam propagating behind an IIF only for some interval of frequencies opens up new possibilities for Mössbauer filtering of SR at grazing angles of incidence of the SR in the transmission geometry.

Thick slab

The angular distribution of the reflected and transmitted CIMS beams at grazing angles of incidence in the limiting case of a thick slab is a topic of interest. Here the term ''thick'' is understood to be a sample whose thickness is such that the characteristic

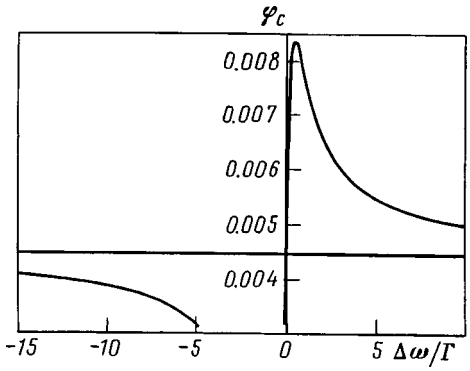

FIG. 2. Computed frequency dependence of the critical angle φ_c of refraction (radians): The horizontal line corresponds to φ_s.

Mössbauer solutions die out in it because of strong resonance nuclear absorption, but in view of the much weaker electronic absorption the intensity of the SR beam has not yet decreased strongly. In this case the reflected CIMS beam at the entrance surface of the slab for angles of incidence $\varphi_0 > \varphi_s$ is described by the formulas for an IIF which follow from Eq. (4):

$$E_r = E_p([\epsilon_M/\epsilon_e - (\cos\varphi_0/\epsilon_e)^2]^{1/2} - \sin\varphi_0/\epsilon_e)/([1-(\cos\varphi_0/\epsilon_e)^2]^{1/2} + [\epsilon_M/\epsilon_e - (\cos\varphi_0/\epsilon_e)^2]^{1/2}). \quad (9)$$

We have for the amplitude of the CIMS beam transmitted through the exit surface

$$\exp(ik_{tz}L)E_t = E_p[([\epsilon_M/\epsilon_e - (\cos\varphi_0/\epsilon_e)^2]^{1/2} + \sin\varphi_0/\epsilon_e)/([1-(\cos\varphi_0/\epsilon_e)^2]^{1/2} + [\varphi_M/\epsilon_e - (\cos\varphi_0/\epsilon_e)^2]^{1/2}). \quad (10)$$

It follows from Eqs. (9) and (10) that for $\varphi_0 > \varphi_s$ sharp maxima of the intensity of the reflected CIMS beam and the CIMS beam transmitted through the slab (see below Figs. 3 and 4) appear in direct proximity to the angle φ_s. We note that a similar maximum was observed in the angular distribution of the reflected beam in an experiment on Mössbauer filtering of SR.[6] A satisfactory interpretation of this maximum has never been found.

Computational results

We shall illustrate the qualitative analysis, performed above, of the TSR phenomenon by the results of numerical calculations. The parameters employed in the calculations approximately correspond to the case of the interaction of SR with an IIF with a highly ^{57}Fe-enriched iron sample. The corresponding Mössbauer transition energy equals 14.4 keV. The following values of the other parameters were used in the calculations: $\mathrm{Re}(1-\epsilon_e) = 10^{-5}$, $\mathrm{Im}(1-\epsilon_e) = 2\times10^{-7}$, $\max \mathrm{Re}(\epsilon_M - 1) = 10\,\mathrm{Re}(1-\epsilon_e)$.

Figure 2 shows the computed spectral dependence of the critical angle φ_c for refraction. The figure shows that for CIMS frequency below the resonance frequency there exists a range of frequencies where the critical angle equals zero, while immediately

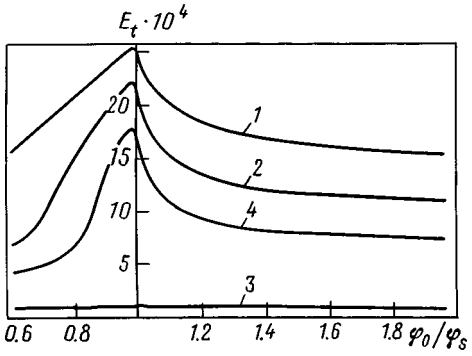

FIG. 3. Computed angular dependence of the amplitude (arbitrary units) of a CIMS beam transmitted through a thick slab for CIMS frequencies $\Delta\omega/\Gamma$ equal to -2 (curve *1*), -5 (curve *2*), 0 (curve *3*), -10 (curve *4*).

above the resonance frequency there exists approximately the same interval of frequencies where the critical angle for refraction is appreciably greater than the critical angle for reflection. In addition, the difference of the corresponding angles reaches values of the order of 3 mrad, i.e., fully amenable to experimental observation.

Figures 3 and 4 show the computed angular dependences of the amplitudes of the transmitted and reflected CIMS waves (for a thick sample) for several values of the CIMS frequency. The curves presented demonstrate that the maxima of the intensity in the transmitted and reflected CIMS beams are reached for angles of incidence of the SR beam near the critical angle in reflection φ_s, that the value of the maximum depends strongly on the frequency, and that the intensity in the forward CIMS beam is much higher than in the reflected beam.

The computed spectral distribution of the amplitude of the CIMS beam which has passed through a thick slab is shown in Fig. 5 for three values of the angle of incidence of the SR beam. The figure demonstrates the phenomenon of Mössbauer filtering of SR

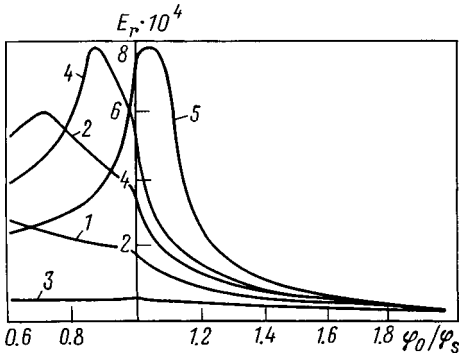

FIG. 4. Angular dependence of the amplitude (arbitrary units) of the CIMS beam reflected from an isotopic interface for CIMS frequencies $\Delta\omega/\Gamma$ equal to -2 (curve *1*), -5 (curve *2*), 0 (curve *3*), -10 (curve *4*), 10 (curve *5*).

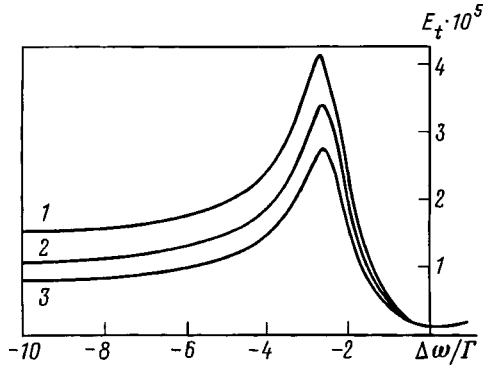

FIG. 5. Computed frequency dependence of the amplitude (arbitrary units) of the CIMS beam transmitted through a thick slab enriched with a Mössbauer isotope, for several values of the grazing angle of the SR beam near the critical angle of reflection (curve *1* — $\varphi_0 = 1.01\varphi_s$; *2* — $\varphi_0 = 1.1\varphi_s$; *3* — $\varphi_0 = 1.5\varphi_s$).

with a displacement of the maximum of the CIMS distribution from the resonance frequency by several energy widths of the Mössbauer line into the region of the frequency of phase synchronism,[4] where the amplitude of the CIMS wave reaches a substantial maximum.

Conclusions

The foregoing analysis of the suppression of the reflection of CIMS beam for grazing angles of incidence demonstrates that this phenomenon is accessible to experimental observation, since the corresponding angular intervals can be easily resolved experimentally. Moreover, the CIMS maxima observed in reflection and especially in transmission could be of interest for Mössbauer filtering of SR. We note that for a sample in the form of a slab and for grazing angles of the SR beam less than the critical angle in reflection, i.e., $\varphi_0 < \varphi_s$, there is no CIMS beam transmitted through the slab. However, if the sample is made in the form of a wedge whose angle is greater than the critical angle in reflection φ_s, then a CIMS beam emerging from the sample does exist right down to zero grazing angle φ_0 of the SR beam for the distinguished CIMS frequencies (see Fig. 2). This opens up additional possibilities for Mössbauer filtering of SR.

The phenomenon studied above occurs not only for IIF but also for a sample placed in vacuum. The difference consists in the fact that now a nonresonance reflection of the SR beam occurs at the boundaries for all frequencies represented in the beam. This reflection is a source of background. Moreover, the expression for the critical angle in reflection of a CIMS beam changes form (for a slab in vacuum $\cos\varphi_s = \epsilon_e^{1/2}$): here $\varphi_s = (1-\epsilon_e^{1/2})^{1/2} = \omega_p/\omega$ and is now equal to the critical angle of TE(I)R for a SR beam at the sample–vacuum interface without regard to Mössbauer scattering.

I thank S. V. Semenov for a discussion of the subject of this work. This work was supported by Russian Fund for Fundamental Research Grant 96-02-18812 and a Grant from the Russian State Scientific Program Fundamental Metrology, Project ''Synchrotron Radiation.''

[a)]e-mail: bel@landau.ac.ru

---

[1] M. Seto, Y. Yoda, S. Kikuta *et al.*, Phys. Rev. Lett. **74**, 3828 (1995).
[2] A. I. Chumakov, A. Q. R. Baron, R. Ruffer *et al.*, Phys. Rev. Lett. **76**, 4258 (1996); A. I. Chumakov, R. Ruffer, A. Q. R. Baron *et al.*, Phys. Rev. B **54**, R9596 (1996).
[3] B. Fultz, C. C. Ahn, E. E. Alp *et al.*, Phys. Rev. Lett. **79**, 937 (1997).
[4] V. A. Belyakov, Zh. Éksp. Teor. Fiz. **108**, 741 (1995) [JETP **81**, 405 (1995)]; JETP Lett. **67**, 8 (1998).
[5] V. A. Belyakov, *Diffraction Optics of Complex-Structured Periodic Media*, Springer, New York, 1992, Chap. 10, p. 333 [supplemented translation of the Russian edition, Nauka, Moscow, 1988].
[6] A. Q. R. Baron, J. Arthur, S. L. Ruby *et al.*, Phys. Rev. B **50**, R10354 (1994).

Translated by M. E. Alferieff

On the ferromagnetism of high-spin states

R. O. Zaĭtsev
Kurchatov Institute Russian Science Center, 123182 Moscow, Russia

(Submitted 26 June 1998)
Pis'ma Zh. Éksp. Teor. Fiz. **68**, No. 4, 275–280 (25 August 1998)

It is established on the basis of the idea of strong interaction within the unit cell that ferromagnetic instability is possible in a system with hopping between *d*-electron states of atoms that are in high-spin states and form a bcc lattice. The phase diagram of the existence of ferromagnetic ordering as a function of the degree of filling of the *d* shell is constructed. © *1998 American Institute of Physics.*
[S0021-3640(98)00516-7]

PACS numbers: 75.10.Jm, 75.30.Cr

A strong intra-atomic electron–electron interaction causes a large increase in the spin part of the magnetic susceptibility. However, an attempt to explain the appearance of ferromagnetism in iron and cobalt on the basis of the Stoner theory leads to contradictory results involving large noninteger values of the saturation magnetic moment.[1] In the present letter the possibility of ferromagnetism arising in iron is analyzed on the basis of the assumption that high-spin hole states $e_g^2 t_{2g}$ $(S=3/2)$ which resonate with two-hole states e_g^2 $(S=1)$ are realized.

We study the simplest model of electronic transitions to a neighboring atom in a bcc lattice with no change in spin projection, so that the interaction Hamiltonian is determined by a single hopping integral t.

Since the Hubbard energy is the largest energy parameter, we will assume it to be infinite.

The equations for the variations δn_N^s of the N-particle occupation numbers, where $s=1,2,\ldots,m$ are the numbers of the N-particle states of lowest energy, can be obtained from the general equation for the averages of T-products of the annihilation operator $\hat{a}_\nu$ times a linear combination of m conjugate X operators with arbitrary coefficients β_s:

$$\hat{a}_\nu=\sum_{s=1}^{m} g_s \hat{X}_{\boldsymbol{\alpha}}^{(N-1,N(s))}, \quad \sum_s g_s\beta_s n_N^{(s)}=T\sum_{s,k} g_k\beta_s\sum_{\omega,\mathbf{p}} G_\omega^{k,s}(\mathbf{p}) f_s \exp(i\omega\delta). \tag{1}$$

Here g_k are prescribed genealogical coefficients, δ is a positive infinitesimal, and $G_\omega^{k,s}(\mathbf{p})$ are the Fourier components of the single-particle Green's function, which in the zero-loop approximation is given in terms of its inverse matrix. For a bcc crystal in neglect of hybridization it can be written as[2]

$$\hat{G}_\omega^{k,s}(\mathbf{p})=[\,\delta_{k,s}(i\omega-\Sigma_s+\mu+\sigma H)-f_k g_k t_{\mathbf{p}} g_s\,]^{-1}. \tag{2}$$

In the particular case of transitions between high-spin states, it is convenient to replace the indices s by the numbers of the levels of the Zeeman multiplets S_z, split by a weak magnetic field δH.

It is evident that the variations of the occupation numbers of individual components of a multiplet are related with one another by the very simple relation[3]

$$\delta n^{(S_z)} \approx \delta(n_0 \exp(wS^z H)) = w n_0 S^z \delta H n^{(S_z)}, \quad S_z = -S, -S+1, \ldots, S.$$

Hence we obtain relations which depend on neither the gyromagnetic factor w nor the ''zeroth'' occupation numbers n_0:

$$\delta n^{(k\sigma)} = k\,\delta n^{(\sigma)}, \quad \sigma = \pm 1; \quad k = 0, \pm 1, \pm 2, \ldots, \pm S \tag{3a}$$

for integer values of the total spin S and

$$\delta n^{((k+1/2)\sigma)} = (2k+1)\,\delta n^{(\sigma/2)}, \quad \sigma = \pm 1; \quad k = 0, \pm 1, \pm 2, \ldots, \pm (S-1/2) \tag{3b}$$

for half-integer values of the total spin S.

We shall now establish a relation between the variations of the different high-spin multiplets formed by particles the number of which is different from 1. We confine ourselves to the zero-loop approximation (Hubbard I approximation[2]), where all of the self-energy parts Σ in the definition (2) are assumed to be constant and are simply added to the chemical potential.

Let us assume first that the coefficients β_s satisfy the orthogonality conditions: $\Sigma_s g_s \beta_s = 0$. As a result of varying the occupation numbers with respect to the magnitude of the external field and taking the limit $H \to 0$, we obtain relations which do not depend explicitly on the magnitude of the applied external field:

$$\sum_{k=1}^{m} g_k \beta_k \delta n_N^k = \frac{T}{g^2} \sum_{k,n} \sum_{\omega, \mathbf{p}} g_s g_n G_\omega^{s,n}(\mathbf{p}) \exp(i\omega\delta) \sum_k g_k \beta_k \delta f_N^k = K_0 \sum_k g_k \beta_k \delta f_N^k. \tag{4}$$

Here K_0 is the average value of the virtual Green's function (2), calculated in a zero external magnetic field, and f_N^k are the so-called terminal factors, equal to the sum of the occupation numbers corresponding to the prescribed transition between individual multiplets. Correspondingly, for $N = 2S$ and integer-valued spin S we have[3,4]

$$|g_k| = \sqrt{(S+k)/2S}, \quad \delta f_N^k = \delta n_N^{(k\sigma)} + \delta n_{N-1}^{((k-1/2)\sigma)}, \tag{5a}$$

where $k = 1-S,\ 2-S,\ \ldots,\ S$. Substituting this definition into Eq. (4) and using relation (3a) together with the orthogonality condition, we obtain

$$(1-K_0)\,\delta n_{2S}^{(\sigma)} = 2K_0\,\delta n_{2S-1}^{(\sigma/2)}. \tag{6a}$$

However, if $N = 2S$ but the total spin is half-integer, then we rewrite Eq. (4) in terms of the occupation numbers $\delta n_N^{((k+1/2)\sigma)}$, the genealogical coefficients g_k, and the terminal factors:

$$|g_k| = \sqrt{(S+k+1/2)/2S}, \quad \delta f_N^k = \delta n_N^{((k+1/2)\sigma)} + \delta n_{N-1}^{(k\sigma)}, \tag{5b}$$

where $k = -S+1/2,\ -S+3/2,\ \ldots,\ S-1/2$. Substituting into Eq. (4) and summing over the integer values of k from $-S+1/2$ to $S+1/2$, we find a relation similar to (6a):

TABLE I.

Interval	f	g^2	$S_{[n_d]}$	$R_{[n_d]+1}$	γ_d	HSS	Ferro ($n_d<n_*$)
$1<n_d<2$	$(4-n_d)/18$	3	1/2	9	1/3	t_{2g}^2	$1<n_d<1.24$
$2<n_d<3$	$(5n_d-6)/36$	2	1	4	2/3	t_{2g}^3	$2<n_d<2.15$
$3<n_d<4$	$(14-3n_d)/20$	5/2	3/2	10	1	$t_{2g}^3e_g$	$3<n_d<3.55$
$4<n_d<5$	$(2n_d-5)/30$	3	2	6	4/3	$t_{2g}^3e_g^2$	$4<n_d<4.25$
Interval		g^2	$S_{[h_d]}$	$R_{[h_d]+1}$	γ_d	HSS	Ferro ($h_d<h_*$)
$4<h_d<5$	$(3h_d-10)/30$	3	2	6	4/3	$t_{2g}^3e_g^2$	$4<h_d<4.18$
$3<h_d<4$	$(8-h_d)/60$	5	3/2	15	1	$t_{2g}^2e_g^2$	$3<h_d<3.38$
$2<h_d<3$	$(10-3h_d)/12$	2	1	12	2/3	$t_{2g}e_g^2$	$2<h_d<2.61$
$1<h_d<2$	$(2+h_d)/12$	3/2	1/2	3	1/3	e_g^2	$1<h_d<1.14$

$$2(1-K_0)\,\delta n_{2S}^{(\sigma/2)}=K_0\,\delta n_{2S-1}^{(\sigma)}. \tag{6b}$$

Relations (3) and (5) make it possible to express all variations in terms of one another and substitute them into the equation of state, which we obtain from Eq. (1) with the condition $\beta_s=g_s$:

$$\sum_{s=1}^{m} g_s^2\,\delta n_N^{(s)}=T\sum_{s,k} g_s g_k \sum_{\omega,\mathbf{p}} \delta\{G_\omega^{s,k}(\mathbf{p})f_k\}\exp(i\omega\delta)$$

$$=(K_0+g^2fD_1)\sum_k g_k^2\,\delta f_N^{(k)}-g^2f_0\sigma D_0\,\delta H. \tag{7}$$

Here all coefficients are calculated at zero magnetic field and are expressed in terms of the integrals of the Fermi function $n_F(\epsilon)$ and its derivative $n_F'(\epsilon)$:

$$K_0=\sum_{\mathbf{p}} n_F(\xi(\mathbf{p}));\quad D_n=\sum_{\mathbf{p}} t^n(\mathbf{p})n_F'(\xi(\mathbf{p}));\quad \xi(\mathbf{p})=g^2ft(\mathbf{p})-\mu. \tag{8}$$

The chemical potential μ is given for $H=0$ in terms of the total number of n_s and n_d states, which is determined by the condition of electrical neutrality for each transition-group element:

$$n_d=[n_d]+fR_{[n_d]+1}K_0,\quad h_d=[h_d]+fR_{[h_d]+1}K_0. \tag{9}$$

Here the brackets denote the integer part of the average number of particles (n_d) or holes ($h_d=10-n_d$) in an incompletely filled d shell. The terminal factors f in zero field and all the coefficients are given for each integer interval of variation of the variables n_d or h_d and are summarized in Table I (HSS denotes high spin states).

The final equation for finding the magnetic susceptibility can be obtained by substituting into Eq. (7) all the variations for all possible values of the spin projection — from Eq. (6a) or (6b). Ultimately, the condition that the magnetic susceptibility is positive assumes the very simple form

$$K_0(1-K_0)>g^2fD_1(\gamma_d+K_0). \tag{10}$$

In this relation the dimensionless quantity γ_d can be expressed in terms of the squared genealogical coefficients g_k^2. In the case of a transition between a high-spin state with a lower N and half-integer spin S ($N-1=2S'=2S-1$) and one with a higher N and integer spin ($N=2S$) we have

$$\gamma_d=g^{-2}\sum_{k=-S+1}^{S}(2k-1)g_k^2, \quad g^2=\sum_{k=-S+1}^{S}g_k^2. \tag{11a}$$

For transitions between high-spin states with smaller N and integer spin $N-1=2S'=2S-1$ and larger N and half-integer spin $N=2S$

$$\gamma_d=g^{-2}\sum_{k=-S+1/2}^{S-1/2}2kg_k^2, \quad g^2=\sum_{k=-S+1/2}^{S-1/2}g_k^2. \tag{11b}$$

Specific values of g^2 and γ_d are presented in Table I.

In studying the single-loop self-energy diagrams, it is sufficient to calculate the individual loops and then sum them taking into account the commutation rules determining the nonzero vertex parts of the kinematic interaction.[3] In the simplest model without hybridization we have only diagonal self-energy parts. For the most important case $2<h_d<3$, pertaining to α iron, we have

$$\Sigma_1^{(\sigma)}=2W_1^{(\sigma)}+3W_3^{(-\sigma)}, \quad \Sigma_2^{(\sigma)}=2W_2^{(\sigma)}+3W_2^{(-\sigma)}-W_3^{(-\sigma)},$$
$$\Sigma_3^{(\sigma)}=3W_1^{(-\sigma)}-W_2^{(-\sigma)}+2W_3^{(\sigma)}. \tag{12}$$

Here

$$W_s^{(\sigma)}=T\sum_{k,\omega,\mathbf{p}}t_{\mathbf{p}}^{s,k}G_{\omega}^{k,s}(\mathbf{p})$$

is the sum of products of matrix elements of the transition matrix $g_s t(\mathbf{p}) g_k$ by elements of the virtual Green's function matrix (2) pertaining to a given spin projection.

It is obvious that in the absence of a field the integrals $W_k^{(\sigma)}$ differ only by factors: $W_k^{(\sigma)}(0)=g_k^2\nu$, so that in this approximation the inclusion of the self-energy parts reduces to a change of the chemical potential.

The next problem is to calculate the corrections $\delta\Sigma_k$, which are proportional to the first power of the magnetic field.

The equation relating the variations of the occupation numbers now also contains variations of the self-energy parts. Thus, for $g_3\beta_3=g_1\beta_1$, $g_2\beta_2=-2g_1\beta_1$, we have instead of Eq. (3b) the expression

$$(1-K_0)(\delta n_{\mathrm{III}}^{(3/2)}-3\,\delta n_{\mathrm{III}}^{(1/2)})=A(\mu)(\delta\Sigma_1-2\,\delta\Sigma_2+\delta\Sigma_3). \tag{13}$$

Setting $\beta_2=0$, $g_3\beta_3=-g_1\beta_1$, we have

$$(1-K_0)(\delta n_{\mathrm{III}}^{(3/2)}+\delta n_{\mathrm{III}}^{(1/2)})-2K_0\delta n_{\mathrm{II}}=A(\mu)(\delta\Sigma_1-\delta\Sigma_3). \tag{14}$$

Here

$$A(\mu)=\sum_{\mathbf{p}}\frac{n_F(\xi_{\mathbf{p}})-n_F(-\mu)}{g^2 t_{\mathbf{p}}}.$$

Variations of the terminal factors can be expressed by means of the general relations (5a) and (5b) in terms of variations of the occupation numbers.

The variation δG of the virtual Green's function acquires new terms:

$$g_1^2\delta n_{\rm III}^{(3\sigma/2)}+g_2^2\delta n_{\rm III}^{(\sigma/2)}+g_3^2\delta n_{\rm III}^{(-\sigma/2)}=K_0\sum_{k=1,2,3}g_k^2\delta f_k^{(\sigma)}+f\sum_{k=1,2,3}g_k^2\delta\Sigma_k^{(\sigma)}D_0$$
$$+g^2f\sum_{k=1,2,3}g_k^2\delta f_k^{(\sigma)}D_1-g^2f\sigma\delta HD_0. \qquad (15)$$

We obtain three additional equations for $\delta\Sigma_k$ directly from their definition in terms of the integrals of the Green's function (11), which corresponds to the one-loop approximation:

$$\delta\Sigma_k^{(\sigma)}=-\delta\Sigma_k^{(-\sigma)}=-[F_{k,n}^{(0)}-D_{k,n}^{(1)}]\delta\Sigma_n^{(\sigma)}+g^2D_{k,n}^{(2)}\delta f_n^{(\sigma)}-\sigma\delta HR_kD_1. \qquad (16)$$

The matrices

$$\hat D^{(n)}=\sum_{\mathbf p}t_{\mathbf p}^n n_F'(\xi_{\mathbf p})\hat U$$

differ in the temperature factor and are proportional to the same matrix $\hat U_{n,m}=R_ng_m/g^2$, which can be expressed in terms of the numerical values of the matrix $\hat S$ constructed in accordance with the definition (12) of the self-energy matrix:

$$\hat S=\begin{pmatrix} 2g_1^2=2; & 0; & -3g_3^2=-1\\ 0; & -g_2^2=-2/3; & g_3^2=1/3\\ -3g_1^2=-3; & g_2^2=2/3; & 2g_3^2=2/3\end{pmatrix},\quad R_k=\sum_n S_{k,n}=\left(1,-\frac{1}{3},-\frac{5}{3}\right). \qquad (17)$$

The matrix $\hat U$ can be represented in the form of products

$$U_{k,n}=R_kg_n/g^2=\sum_m S_{k,m}g_n/g^2,\quad g^2=\sum_k g_k^2=2. \qquad (18)$$

The operator $\hat F^{(0)}=Q(\mu)\hat W$, where $Q(\mu)=[K_0-n_F(-\mu)]/fg^2$. In the matrix $\hat W$ the elements of each row sum to zero:

$$W_{n,m}=U_{n,m}-S_{n,m}=\sum_p S_{n,p}g_m/g^2-S_{n,m}. \qquad (19)$$

As a result, we obtain an equation for determining the limit of ferromagnetic stability:

$$Q=1\ \text{ or }\ h_*^*=8/3; \qquad (20a)$$

$$\{3K_0(1-K_0)-2fD_1(2+3K_0)\}\{9(1+2Q)+D_1(-1+6Q)\}$$
$$=2D_2\{fD_0(2+3K_0)(1-6Q)-20A(\mu)\}. \qquad (20b)$$

The region of ferromagnetic instability ($14/5>h_d>8/3$), obtained according to the condition (20a), exists completely independently of the region $2<h_d<h_*$, obtained from

the solution of Eq. (20b). Since $h_* < 8/3$, the ferromagnetic instability corresponding to the solution of Eq. (20b) that adjoins the approximate solution of Eq. (10) is examined below.

The calculations of the points of critical density n_* and h_*, below which ferromagnetic instability arises at $T=0$, were performed in a model of semielliptic initial density of states in the variable t_p (see Table I). On the basis of the criterion (10), ferromagnetic instability was observed inside each integer interval of variation of the *d*-electron density, where electrons (or holes) resonate between high-spin states (see Table I). Exceptions are regions of low particle density $n_d < 1$ and hole density $h_d = 10 - n_d < 1$, where the system resonates between empty and single-particle or single-hole states. The appearance of separate regions of ferromagnetic instability is due to the possibility of a change in the sign of the scattering amplitude for Fermi excitations with opposite spins.

Of greatest interest for comparing with experiment is the electronic interval $7 < n_d < 8$, which corresponds to ferromagnetic α iron, which possesses a bcc lattice. In the hole representation $2 < h_d < 3$, so that here the two-hole e_g^2 and three-hole $e_g^2 t_g$ states resonate.

For the simplest model of a semielliptic band, we find the following region of existence of a ferromagnetic instability: $2 < h_d < 2.61$ in the zero-loop approximation and $2 < h_d < 2.52$ in the one-loop approximation.

The observed value of the saturation magnetic moment $\approx 2.2\mu_B$ corresponds to a density value located inside the ferromagnetic region.

This work was supported by the Russian Fund for Fundamental Research and was carried out under an agreement with Project 98-02-17388.

[1] J. Goodenough, *Magnetism and the Chemical Bond*, Interscience, New York, 1963 [Russian translation, Metallurgiya, Moscow, 1988].
[2] J. Hubbard, Proc. R. Soc. London, Ser. A **277**, 237 (1964).
[3] R. O. Zaĭtsev, Zh. Éksp. Teor. Fiz. **112**, 2223 (1997) [JETP **85**, 1218 (1997)].
[4] D. E. Smirnov and Yu. F. Smirnov, *The Theory of the Optical Spectra of Transition-Metal Ions* [in Russian], Nauka, Moscow, 1977.

Translated by M. E. Alferieff

Nonlinear low-temperature magnetization of the quasi-one-dimensional charge-density-wave conductor $K_{0.3}MoO_3$

D. V. Eremenko and A. V. Kuznetsov
Moscow Engineering-Physics Institute, 115409 Moscow, Russia

S. V. Zaĭtsev-Zotov[a)]
Institute of Radio Engineering and Electronics, Russian Academy of Sciences, 103907 Moscow, Russia

V. N. Trofimov
Joint Institute of Nuclear Research, 141980 Dubna, Moscow Region, Russia

(Submitted 2 July 1998)
Pis'ma Zh. Éksp. Teor. Fiz. **68**, No. 4, 281–286 (25 August 1998)

A study is made of the temperature and field dependences of the anisotropic magnetization of a quasi-one-dimensional charge-density-wave conductor — the blue bronze $K_{0.3}MoO_3$. Nonlinearity of the magnetization curves is observed at temperatures below 100 K. The temperature and field dependences of the magnetic moment show the effect to be of a collective nature. © *1998 American Institute of Physics.* [S0021-3640(98)00616-1]

PACS numbers: 75.45.+j, 71.45.Lr, 75.60.Ej

Questions concerning macroscopic quantum phenomena in charge-density waves (CDWs) have been drawing increased interest in recent years. Although the possibility of observing such effects has been discussed for more than 20 years,[1–5] only comparatively recently has it been possible to show experimentally that they actually can be observed in quasi-one-dimensional CDW conductors.[6,7] For example, the observation of oscillations of the nonlinear conductivity in a magnetic field in $NbSe_3$ samples with columnar defects was reported in Ref. 7. It is believed that this effect is an analog of the Aharonov–Bohm effect for collective conductivity due to the motion of a CDW.[2–5,7,8] The existence of the Aharonov–Bohm effect raises the question of the possibility of observing persistent currents in systems with CDWs.[3,5] The objective of our investigation was to search experimentally for the contribution of persistent currents to the magnetization of a quasi-one-dimensional CDW conductor. Unfortunately, the most direct methods (studying the magnetization of a ring consisting of a quasi-one-dimensional conductor or a sample with columnar defects) are not easily accessible because of the lack of an appropriate technology for producing ring structures and also because of the need to perform measurements in high magnetic fields (>100 kOe) when studying samples with columnar defects. Nonetheless, since a CDW is not uniform because of the random nature of the distribution of pinning centers and can contain topological defects (dislocations, solitons),

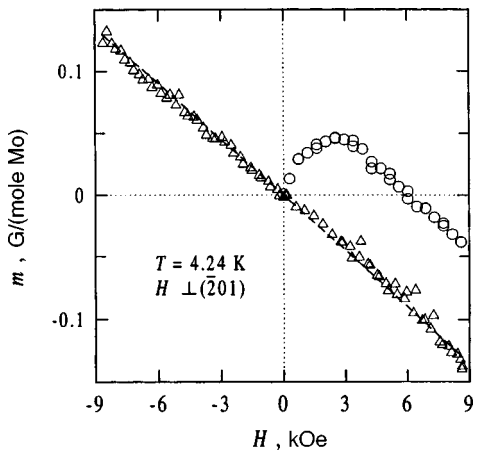

FIG. 1. Magnetization curves for a $K_{0.3}MoO_3$ crystal in a field perpendicular to the MoO_6 layers in the absence (△) and presence (○) of nonlinear magnetization. The slope of the dashed straight line corresponds to the susceptibility measured at $T=4.24$ K (Fig. 3).

one expects[3,9] that a persistent-current contribution to the magnetization should exist for quasi-one-dimensional conductors of arbitrary shapes and sizes.[b)] In the present work we performed precise investigations of the dependence of the magnetization m of $K_{0.3}MoO_3$ single crystals on the temperature, magnetic field intensity, magnetic field orientation relative to the crystal lattice, and the dimensions of the samples.

$K_{0.3}MoO_3$ was chosen as the object of investigation because this quasi-one-dimensional conductor has been studied comparatively well[10] and is readily available in the form of large crystals. $K_{0.3}MoO_3$ is highly anisotropic,[10,11] possesses a monoclinic unit cell, and consists of metallic chains oriented in the direction of the monoclinic b axis, which is the direction of highest conductivity. The chains consist of MoO_6 octahedra, which are arranged in layers parallel to the (201) plane of the reciprocal lattice. At a temperature $T_P=182$ K it passes into the Peierls state with the formation of an incommensurate CDW with a temperature-dependent period somewhat greater than $4b$. Vanishing of the Fermi surface as a result of the formation of a CDW decreases the electronic contribution to the magnetic susceptibility, the decrease being observed in the form of a step in the temperature dependence $\chi(T)$.[11]

The magnetization was measured with a SQUID magnetometer[12] in stationary magnetic fields H up to 9 kOe in the temperature range 4.2 K $\leqslant T \leqslant$ 300 K. Samples with typical dimensions $2\times2\times2$ mm were cut from comparatively large single crystals. $K_{0.3}MoO_3$ cleaves easily along the MoO_6 layers, and for this reason one face of the samples was parallel to the (201) plane. The measurements were performed with field orientations parallel to the chains, perpendicular to the planes, and also parallel to the planes but perpendicular to the chains. Several single crystals demonstrating qualitatively identical behavior were investigated.

The field dependence of the magnetization is linear in the metallic state at temperatures $T>T_P$. In the CDW state at temperatures $T<100$ K we observe both linear and nonlinear $m(H)$. Figure 1 shows typical magnetization curves in a field applied perpen-

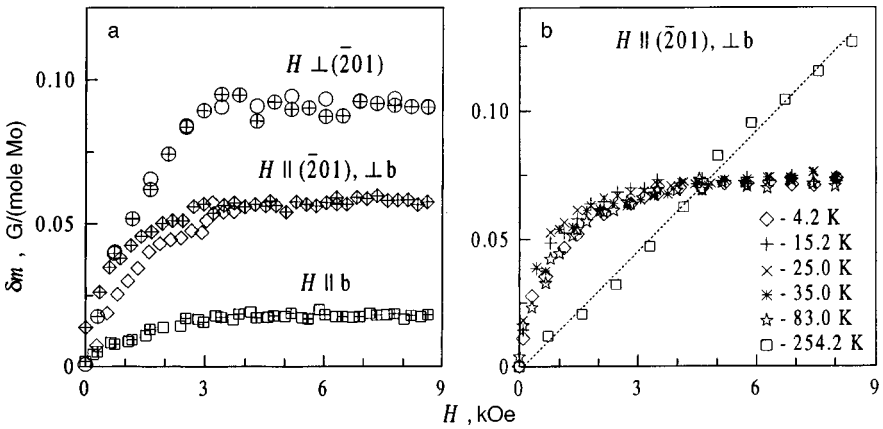

FIG. 2. Nonlinear contribution of the magnetization of a $K_{0.3}MoO_3$ single crystal (a) for different field orientations at $T=4.2$ K and (b) in a field perpendicular to the MoO_6 layers at different temperatures. The unfilled and cross-filled symbols in part a correspond to the initial introduction and withdrawal, respectively, of the magnetic field.

dicular to the planes. Immediately after cooling in zero field a linear magnetization was observed in the sample. The strong nonlinearity of $m(H)$, as a rule, arising abruptly after some time has passed, was later reproducible. Similar behavior was observed for all field orientations,[c)] and for most single crystals the nonlinear magnetization was observed more often than linear magnetization. As one can see from the figure, the slopes of the curves are virtually identical for $H>4$ kOe. Therefore a nonlinear contribution to the magnetization, saturating in high fields, arises in the sample together with a linear contribution.

Figure 2 displays the form of the nonlinear contribution $\delta m(H)$ obtained after the linear part of the susceptibility is subtracted out. Comparing the curves for different field orientations (Fig. 2a) shows that the nonlinear contribution is anisotropic. In a field $H\|(\bar{2}01)$, $\perp b$, the dependence $\delta m(H)$ exhibits pronounced hysteresis and an accompanying nonzero magnetization in zero field. The accuracy of our experiment did not make it possible to determine unequivocally the presence or absence of hysteresis for other orientations, but a remanent magnetization of very low amplitude was detected for them also. We note that the field in which $\delta m(H)$ saturates and the magnitude of the saturation magnetization are virtually independent of temperature (Fig. 2b).

We studied the temperature behavior of the magnetization. Figure 3 shows the typical dependences $m(T)/H$ in a 8.5 kOe field. In the absence of a nonlinear contribution, the curves correspond to temperature dependences of the anisotropic magnetic susceptibility $\chi(T)$ that agree with published data.[11] At low temperatures the dependences containing a nonlinear contribution differ from the corresponding $\chi(T)$ curves by an approximately constant amount. This confirms the weak temperature-dependence of the saturated nonlinear magnetization (Fig. 2b), at least at temperatures $T\lesssim 100$ K.

To determine the influence the surface and the dimensions of the sample, we performed measurements of the magnetization of powder prepared from a portion of the single crystal. It was found that at low temperatures it also consists of linear and nonlin-

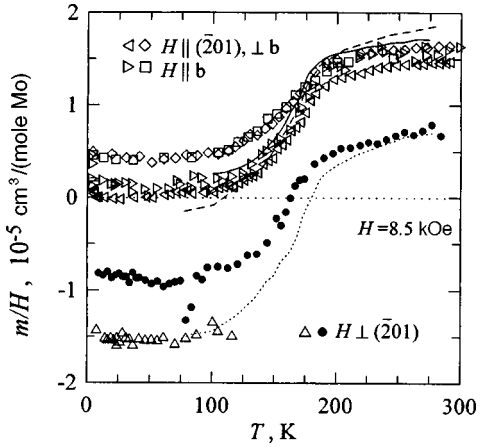

FIG. 3. Temperature dependences $m(T)/H$. The triangles correspond to the anisotropic susceptibility of a $K_{0.3}MoO_3$ single crystal in the absence of nonlinear magnetization. All other symbols reflect the temperature behavior of the magnetization including a nonlinear contribution. The continuous curves show the $\chi(T)$ curves published in Ref. 11; solid curve — Johnston, dashed curve — Kwok *et al.*, dotted curve — Morris and Wold.

ear contributions. At temperatures $T>50$ K the magnitude of the linear contribution corresponded approximately to the orientation-averaged linear magnetization of the single crystal. At $T<20$ K the linear contribution demonstrated close-to-Curie temperature behavior. At $T=4.2$ and 61 K the nonlinear contribution saturated in fields of 2 kOe and 4 kOe, respectively, and it had amplitudes of 19 ± 2 and 15 ± 1 mG/(mole Mo).

The results presented above show that the low-temperature magnetization of $K_{0.3}MoO_3$ contains a contribution that is nonlinear in the field and does not depend on the ratio of the volume to surface area, so that it must reflect the bulk properties of the samples. The nonlinearity of the magnetization was noted earlier[11] in investigations of the susceptibility of $K_{0.3}MoO_3$ and was attributed to ferromagnetic contamination. Although we observed ferromagnetic contamination of some samples, their behavior is different from that described above. For contaminated samples a substantial nonlinear magnetization is present both above and below the Peierls transition temperature, and above the transition $m(T)/H$ is greater than the known values of the susceptibility.

Let us analyze the possible origin of δm. The possibility of abrupt onset of a nonlinear contribution shows that the effect is associated with the electronic superstructure. At the same time, it is unlikely to be associated with persistent currents. The contribution of persistent currents of CDWs or normal electrons[9] to the magnetization should be of an oscillatory character with period $\Delta H=\Phi_0/2S_\perp$, where Φ_0 is the magnetic flux quantum and $S_\perp$ is the projection of the area of a closed trajectory of the carriers on a plane orthogonal to the direction of the magnetic field. When the variance in the forms and orientations of the trajectories is taken into account, the trajectory-averaged contribution should have a maximum at $H\sim\Phi_0\langle 1/S_\perp\rangle$ and should vanish for $H \gg \Phi_0\langle 1/S_\perp\rangle$, which does not correspond to the behavior of $\delta m(H)$ (Fig. 2a).

For every ten Mo ions there are three $4d$ electrons which are not bound by oxygen orbitals, so that the nonlinear magnetization may reflect the onset of correlations of the

electronic structure with the formation of antiferromagnetic ordering or spin-density waves.[13] Such an explanation is at variance with the low value of the moment per Mo ion, $\mu \sim 2 \times 10^{-5} \mu_B$ (μ_B is the Bohr magneton), which is three orders of magnitude smaller than the moments characteristic for spin-density waves[14] or uniaxial antiferromagnets.[15]

We attribute the abrupt onset of nonlinear magnetization to the relaxation of metastable states of CDWs. As is well known, the magnitude of the wave vector of a CDW in $K_{0.3}MoO_3$ is temperature-dependent.[16] The change produced in the wave vector by the phase slip of CDWs is accompanied by the overcoming of energy barriers $\sim 10^3$ K which depend on the magnitude of the deviation from equilibrium and lead to the appearance of long-lived metastable states.[17] The pinning of CDWs is an additional factor promoting the formation of metastable states. Relaxation of metastable states can arise under the action of vibrations, electromagnetic pulses, and other poorly controllable influences, which apparently occurs when the samples are allowed to stand for a long time at low temperature. The hysteresis of the field dependence of the nonlinear magnetization signifies that the interaction with the magnetic field provides sufficient energy to transfer a portion of the CDW into a new long-lived metastable state.

The CDW itself, interpreted as being due to singlet pairing of an electron and a hole, does not possess magnetic properties, but charge and spin density oscillations arising around pinning centers[13] can give rise to a magnetic moment at pinning centers. For typical atomic impurity density $\sim 10^{-3}$, in our samples there is a moment $\mu \sim 10^{-2} \mu_B$ for each pinning center, corresponding in order of magnitude to the moment characteristic for the period of a spin-density wave.[13,14] This value of the moment is a very reasonable estimate for the spin polarization arising around a pinning center.

The form obtained for $\delta m(H)$ attests to a correlated state of magnetic moments. In the case of independent moments the experimentally observed remanent magnetization is absent because of the thermal disorientation of the moments. Moreover, saturation in a system of independent moments is observed when the moment–field interaction energy becomes of the order of the thermal energy. For the measured saturation field and the moment μ estimated above, the interaction energy is $\sim 10^{-3}$ K $\ll T$, so that saturation should not occur in such weak fields.

We note that the average distance between pinning centers and therefore between moments also is of the order of tens of lattice periods. The phase correlation length in $K_{0.3}MoO_3$ (not less than 1000 Å[16]) is much greater than the distance between the moments. It has not been ruled out that the interaction of the magnetic moments via a coherent CDW is responsible for the onset of a correlation of the moments. Further investigations are required in order to determine the structure of the magnetic order that arises and the mechanism of interaction of the moments.

In summary, the low-temperature magnetic susceptibility of $K_{0.3}MoO_3$ is a nonlinear function of the magnetic field and exhibits hysteresis. The results obtained show the effect to be of a collective nature.

We thank R. E. Thorne for providing the $K_{0.3}MoO_3$ single crystals and K. V. Klement'ev for developing the program for processing SQUID magnetometer signals. This work was supported by the Russian Fund for Fundamental Research (Grant No.

98-02-16667) and the International Science and Technology Program ''Physics of Solid-State Nanostructures'' (Grant No. 97-1052).

[a)]e-mail: serzz@mail.cplire.ru

[b)]It can be expected that at sufficiently low temperatures the motion of electrons along the centers of the dislocation loops of CDWs with metallization of the cores[9] will give rise to persistent currents.

[c)]For the orientation $H \| b$ the linear magnetization is paramagnetic, while for $H \| (\bar{2}01)$, $\perp b$, the susceptibility is close to zero (see Fig. 3 below).

[1] A. I. Larkin and P. A. Lee, Phys. Rev. B **17**, 1596 (1978); K. Maki, Phys. Rev. Lett. **39**, 46 (1977); Phys. Rev. B **18**, 1641 (1978); J. Bardeen, Phys. Rev. Lett. **42**, 1498 (1979); **45**, 1978 (1980).
[2] I. O. Kulik, A. S. Rozhavskiĭ, and E. N. Bogachek, JETP Lett. **47**, 303 (1988).
[3] É. N. Bogachek, I. V. Krive, I.O. Kulik, and A. S. Rozhavskiĭ, Zh. Éksp. Teor. Fiz. **97**, 603 (1990) [Sov. Phys. JETP **70**, 336 (1990)].
[4] A. S. Rozhavskiĭ, Fiz. Nizk. Temp. **22**, 462 (1996) [Low Temp. Phys. **22**, 360 (1996).
[5] M. F. Visscher, B. Rejaei, and G. E. W. Bauer, Europhys. Lett. **36**, 613 (1996).
[6] S. V. Zaitsev-Zotov, Phys. Rev. Lett. **71**, 605 (1993); S. V. Zaitsev-Zotov, G. Remenyi, and P. Monceau, Phys. Rev. B **56**, 6388 (1997).
[7] Yu. I. Latyshev, O. Laborde, P. Monceau, and S. Klaumünzer, Phys. Rev. Lett. **78**, 919 (1997).
[8] A. A. Zvyagin and I. V. Krive, Fiz. Nizk. Temp. **21**, 697 (1995) [Low Temp. Phys. **21**, 533 (1995)].
[9] S. N. Artemenko and F. Gleisberg, Phys. Rev. Lett. **75**, 497 (1995).
[10] J. Dumas and C. Schlenker, Int. J. Mod. Phys. B **7**, 4045 (1993).
[11] L. F. Schneemeyer, F. J. DiSalvo, R. M. Fleming, and J. V. Waszczak, J. Solid State Chem. **54**, 358 (1984); D. C. Johnston, Phys. Rev. Lett. **52**, 2049 (1984); R. S. Kwok, G. Grüner, and S. E. Brown, Phys. Rev. Lett. **65**, 365 (1990); B. L. Morris and A. Wold, Rev. Sci. Instrum. **39**, 1937 (1968).
[12] V. N. Trofimov, Cryogenics **32**, 513 (1992).
[13] G. Grüner, Rev. Mod. Phys. **66**, 1 (1994).
[14] K. Mortensen, Y. Tomkiewicz, and K. Bechgaard, Phys. Rev. B **25**, 3319 (1982).
[15] K. Miyagawa, A. Kawamoto, Y. Nakazawa, and K. Kanoda, Phys. Rev. Lett. **75**, 1174 (1995); A. Zheludev, S. Maslov, G. Shirane *et al.*, Phys. Rev. Lett. **78**, 4857 (1995).
[16] J. P. Pouget, S. Girault, and A. H. Moudden, Phys. Scr. **T25**, 58 (1989).
[17] D. V. Borodin, S. V. Zaĭtsev-Zotov, and F. Ya. Nad', Zh. Éksp. Teor. Fiz. **93**, 1394 (1987) [Sov. Phys. JETP **66**, 793 (1987)].

Translated by M. E. Alferieff

Effect of optical radiation on magnetic resonance in Fe/Si/Fe trilayer films

G. S. Patrin[a)]
Krasnoyarsk State University, 660041 Krasnoyarsk, Russia

N. V. Volkov and V. P. Kononov
L. V. Kirenskiĭ Institute of Physics, Siberian Branch of the Russian Academy of Sciences, 630036 Krasnoyarsk, Russia

(Submitted 3 July 1998)
Pis'ma Zh. Éksp. Teor. Fiz. **68**, No. 4, 287–290 (25 August 1998)

A photoinduced change in the magnetic resonance parameters is observed in trilayer films of the system Fe/Si/Fe. The shifts of the resonance field and the character of the interlayer interaction are investigated as functions of the temperature, illumination of the films, and thickness of the silicon interlayer. It is found that at low temperatures the photoinduced contribution to the exchange interaction constant between the iron layers is antiferromagnetic. © *1998 American Institute of Physics.* [S0021-3640(98)00716-6]

PACS numbers: 75.70.Cn, 76.50.+g

The production of multilayer magnetic films has opened up wide prospects for developing magnetic materials with prescribed properties. Varying the chemical components and thicknesses and the manner of stacking of the components sometimes leads to unexpected effects. In multilayer metal films with a nonmagnetic interlayer the main features are giant magnetoresistance and an exchange parameter which oscillates as a function of the thickness of the nonmagnetic interlayer.[1] The characteristic period of the spatial variations for these films is 10–20 Å, and the magnitude of the oscillations depends on the interlayer material, i.e., essentially, on the characteristic features of the conduction-electron density-of-states function. The diversity of observed effects is enriched even more by using combined methods of acting on the material. In this respect, it is very tempting to study systems with a semiconductor interlayer, since here the charge-carrier density can be controlled by varying the temperature or by implanting dopants or by optical irradiation.

In the present letter we report the results of investigations of the change produced in the magnetic state in the Fe/Si/Fe film system by optical irradiation, as detected by electron magnetic resonance.

Fe/Si/Fe trilayer films were obtained by molecular-beam epitaxy on the Angara apparatus, modified for depositing magnetic materials.[2] Four samples with different silicon interlayer thicknesses t_{Si} were prepared in one deposition cycle. In all the experimental samples the iron layer was 50 Å thick. The thicknesses were monitored with a quartz meter for measuring thickness and rate of film growth. In each deposition cycle

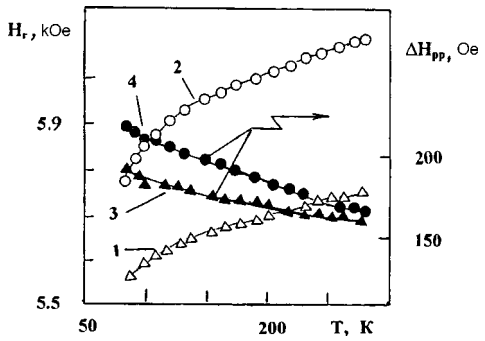

FIG. 1. Temperature dependences of the magnetic-resonance parameters: *1,3* — Reference film, *2,4* — with a silicon interlayer $t_{Si}=20$ Å, ΔH_{pp} — the magnetic resonance linewidth.

one reference film with iron thickness $t_{Fe}=100$ Å was prepared. All these films were also compared with one another in respect to the microwave absorption intensity for the purpose of determining the difference in the mass of the magnetically active material. According to the magnetic resonance parameters, the best films were obtained on a mica substrate. The measurements of the magnetic-resonance parameters were performed on the apparatus described in Ref. 3. The microwave frequency was $f=35$ GHz. The magnetic field lay in the film plane. An Ar laser operating in the range $\lambda=0.49-0.514$ μm served as the source of optical radiation.

It has been established[4] from data on direct measurements of the magnetization on a SQUID magnetometer and on the magnetooptic Kerr effect that ferromagnetic iron layers interact antiferromagnetically at room temperature, and on cooling to $T\geqslant 80$ K they become virtually uncoupled and the entire system shows ferromagnetic behavior. Under laser irradiation ($\lambda=0.5145$ μm) the system once again shows indications of antiferromagnetic coupling between iron layers.

Since the conditions of magnetoresonance absorption are determined by the effective internal fields, the magnitude and sign of the exchange coupling constant,[5] both with and without optical irradiation, can be judged according to the shift of the resonance field of a film with a semiconductor interlayer relative to a film without such an interlayer.

Figure 1 illustrates the temperature behavior of the magnetic resonance parameters of the reference film (curves *1,3*) and a film with silicon interlayer thickness $t_{Si}=20$ Å (curves *2,4*). One can see that the silicon layer induces an appreciable change in the resonance conditions. As the temperature increases, the difference of the resonance fields of these two films increases, which can be interpreted as an increase in the interaction between the iron layers. Conversely, the difference of the linewidths of the magnetoresonance peaks decreases, apparently because of the decrease in the stresses in the films at the iron–silicon interfaces.

The change in the shift of the resonance field (δH_r) as a function of the silicon layer thickness is shown in Fig. 2. The intensification of the ferromagnetic interaction (negative shift δH_r) for small silicon thicknesses ($t_{Si}^{*}\leqslant 15$ Å) is interesting. For silicon interlayers $t_{Si}^{0}>70-80$ Å the sign of the exchange interaction depends on the temperature. In the

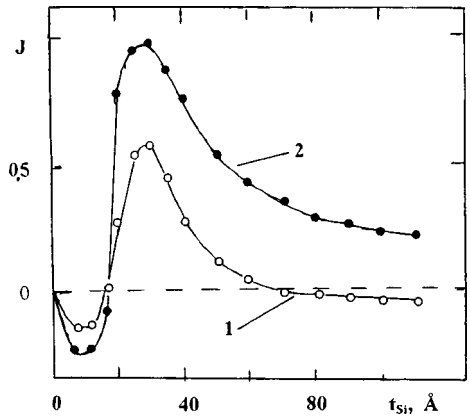

FIG. 2. Normalized shift of the resonance field as a function of the silicon interlayer thickness: $J=\delta H_r/\delta H_r^{\max}$; curve *1* — $T=80$ K, *2* — $T=300$ K.

region $t_{Si}^{*}\leqslant t_{Si}\leqslant t_{Si}^{0}$ the interaction of the layers is of an antiferromagnetic character at all temperatures investigated.

In the case of an intermediate layer prepared from a semiconductor material, it is obvious that the shifts of the resonance field under optical irradiation, as a result of the appearance of photoelectrons in the conduction band, and under trivial heating should be of the same sign. When light is absorbed in the substrate and iron layers, a portion of the energy of the optical radiation is dissipated in the form of heat. For this reason, we measured the heating-induced shift (δH_r^h) of the resonance field in the reference sample as function of temperature (Fig. 3a). It was then subtracted from the total shift of the resonance field in the sample under irradiation. The remainder $\delta H_r^{\text{ind}}=\delta H_r-\delta H_r^h$ was

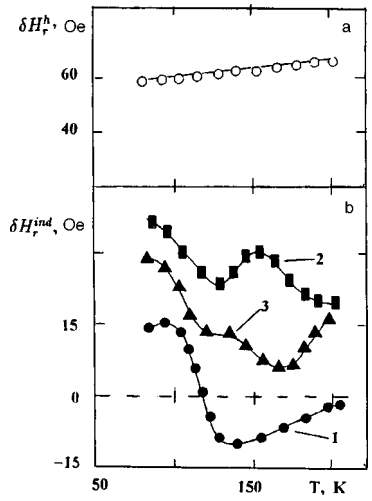

FIG. 3. Temperature dependences of the photoinduced shift of the resonance field: a — Reference film, b — Fe/Si/Fe film, curve *1* — $t_{Si}=5$ Å, *2* — $t_{Si}=10$ Å, *3* — $t_{Si}=20$ Å; $S_{opt}=2.8$ W/cm^2.

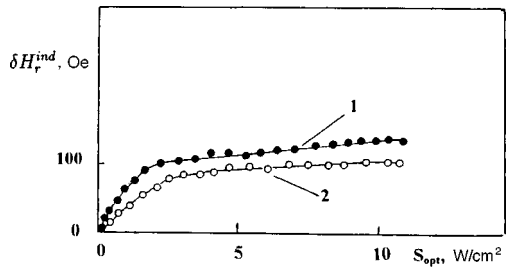

FIG. 4. Shift of the resonance field of Fe/Si/Fe films as a function of the irradiance: *1* — $t_{Si}=10$ Å, *2* — $t_{Si}=20$ Å; $T=80$ K.

attributed to the action of light on the semiconductor material. The temperature dependences of the photoinduced shifts δH_r^{ind} of the resonance field for samples with different silicon thicknesses are presented in Fig. 3b. Here a nonmonotonic variation of δH_r^{ind} is present. In the temperature range $T\cong 80-100$ K, for small silicon thicknesses, specifically, $t_{Si}<t_{Si}^*$, the photoinduced shift of the resonance field increases as t_{Si} increases, while for $t_{Si}>t_{Si}^*$ it decreases somewhat. For larger semiconductor interlayer thicknesses ($t_{Si}>t_{Si}^0$) the effect can be attributed almost entirely to the thermal action of the radiation.

For $T\leqslant 120$ K the photoinduced changes in the exchange interaction are exclusively of an antiferromagnetic character, and a change in sign of the exchange parameter in the region $T\approx 120$ K is observed only for very thin silicon interlayers (Fig. 3b, curve *1*). In the latter case, as the temperature increases further, the photoinduced changes in the magnetic system tend to zero. As a function of the irradiance (S_{opt}), the photoinduced shift of the resonance field saturates, for example, at $S_{opt}=2$ W/cm^2 for $t_{Si}=10$ Å and at $S_{opt}=3.5$ W/cm^2 for $t_{Si}=20$ Å (see Fig. 4).

We do not attribute the observed properties in Fe/Si/Fe layered structures to the formation of Fe–Si compounds, since it is well known[6] that silicon doping of iron always decreases the magnetic moment and weakens the exchange interaction. Here, however, we have an increase in the effective internal field, which can be explained by assuming that the exchange coupling between the iron layers intensifies.

At present the ''quantum well'' model is most widely used to describe the magnetic properties of multilayer magnetic structures.[7,8] In this model the oscillations of the exchange interaction parameter in the case of a metal interlayer are determined by the oscillations of the spectral density of the electronic states, which depends on the number of planes of the intermediate layer. In application to our case, the situation must be corrected, since, most likely, for the present technological regime the silicon interlayer has an amorphous structure, and this means that short-range order is only approximately preserved in the interlayer, and the spectral density of electronic states is not necessarily periodic.[9] Here the characteristic thickness of the silicon interlayer at which the maximum interaction of the iron layers is observed should be related with the electron mean free path in amorphous silicon. This fact can explain the absence of clearly expressed oscillations of the exchange parameter and consequently of a shift of the resonance field as a function of the thickness of the semiconductor. The sign of the exchange parameter (phase of the oscillations) at the start of the dependence on the interlayer thickness is

determined both by the type of extremum on the Fermi surface and by the character of the line-up of the bands at the interfaces.[8]

The change in the magnetic state under irradiation is primarily due to the change in the density of the charge carriers in the semiconductor, which are carriers of the interaction between the magnetically active layers, and to the restructuring of the electron density of states. We note once again that at low temperatures the photoinduced contribution is always antiferromagnetic. The temperature-induced changes in the magnetic properties in the system Fe/Si/Fe can be understood by assuming that the chemical potential is temperature-dependent.

We thank G. V. Bondarenko for performing the x-ray analysis of the experimental samples.

These investigations are conducted with the support of the Russian Fund for Fundamental Research (Project 96-02-16546-a) and as part of the program ''Integration.''

[a)]e-mail: pat@iph.krasnoyarsk.su

---

[1] P. Grunberg, R. Schreiber, Y. Pang *et al.*, Phys. Rev. Lett. **57**, 2442 (1986).
[2] E. G. Eliseeva, V. P. Kononov, V. M. Popel *et al.*, Prib. Tekh. Eksp., No. 2, 141 (1997).
[3] N. V. Volkov and G. S. Patrin, Preprint No. 635F [in Russian], Institute of Physics, Siberian Branch of the Russian Academy of Sciences, Krasnoyarsk, 1990.
[4] J. E. Mattson, E. E. Fullerton, S. Kumar *et al.*, J. Appl. Phys. **75**, 6169 (1994).
[5] A. Laude, J. Magn. Magn. Mater. **92**, 143 (1990).
[6] E. P. Elsukov, Author's Abstract of Doctoral Dissertation [in Russian], Moscow State University, Moscow, 1994.
[7] D. M. Edwards, J. Mothon, R. B. Muniz, and M. S. Pan, J. Phys.: Condens. Matter **3**, 4941 (1991).
[8] J. Mothon, M. Willert, D. M. Edwards, and R. B. Muniz, Fiz. Met. Metalloved. **79**, 9 (1995).
[9] N. F. Mott and E. A. Davis, *Electronic Processes in Non-Crystalline Materials*, Clarendon Press, Oxford, 1971 [Russian translation, Mir, Moscow, 1974].

Translated by M. E. Alferieff

Flux noise near the Berezinskiĭ–Kosterlitz–Thouless transition

K.-H. Wagenblast
Institut für Theoretische Festkörperphysik, Universität Karlsruhe, D-76128 Karlsruhe, Germany

R. Fazio
Istituto di Fisica, Università di Catania, I-95129 Catania, Italy;
Istituto Nazionale di Fisica della Materia (INFM), Unità di Catania, Italy

(Submitted 6 July 1998)
Pis'ma Zh. Éksp. Teor. Fiz. **68**, No. 4, 291–295 (25 August 1998)

The flux noise in Josephson junction arrays is studied in the critical regime above the Berezinskiĭ–Kosterlitz–Thouless transition. In proximity-coupled arrays a local Ohmic damping for the phases is relevant, giving rise to anomalous vortex diffusion and a dynamic scaling of the flux noise in the critical region. The flux noise exhibits a crossover from white to $1/f$ noise at a frequency $\omega_\xi \propto \xi^{-z}$ with a dynamic exponent $z=2$. © *1998 American Institute of Physics.* [S0021-3640(98)00816-0]

PACS numbers: 74.40.+k, 74.60.Ge, 74.50.+r

Various two-dimensional systems undergo the Berezinskiĭ–Kosterlitz–Thouless (BKT) pair-unbinding transition.[1,2] The transition between the high-temperature (disordered) and the low-temperature (coherent) phase is driven by the thermally excited vortices. These topological excitations form a two-dimensional Coulomb gas. Below the BKT transition temperature T_{BKT} they are bound in vortex–antivortex pairs. Above the critical temperature the pairs dissociate and form a vortex plasma. In the plasma phase the vortex–vortex interaction is screened at a distance of the order of the correlation length ξ, which diverges at T_{BKT}.

Arrays of Josephson junctions are prototype systems for studying the BKT transition. Below the BKT transition the array is phase coherent and thus superconducting. In the plasma phase, on the contrary, free vortices destroy the coherence and the system is resistive, although each island remains superconducting. In the last decade there has been a great amount of work on the various aspects of the BKT transition in Josephson arrays (see Ref. 3 for an overview). Experimental studies are based on electrical resistance,[4] two-coil inductance,[5,6] and superconducting quantum interference device (SQUID)[7,8] measurements.

Anomalous suppression of the vortex mobility has been observed in proximity-coupled Josephson junction arrays by Théron *et al.*[6] The vortex mobility vanishes logarithmically at low energies, showing that vortex motion in these arrays cannot be described by a Drude model with a constant mobility. This behavior has been explained

either introducing a local Ohmic damping for the phases of the superconducting wave function[9,10] or by invoking long-range vortex interactions.[11] More recently a regime interpretation of the vortex dynamics was given in Ref. 12.

In a recent letter, Shaw *et al.*[7] investigated the magnetic flux noise close to the BKT transition in an overdamped Josephson junction array by means of a SQUID. The flux-noise spectrum is defined as

$$S_\Phi(\omega)=\int dt e^{i\omega t}\langle\Phi(t)\Phi(0)\rangle, \tag{1}$$

where $\Phi(t)$ is the flux detected by the SQUID and is proportional to the vortex density integrated over the SQUID area. Near the transition the flux noise is white for frequencies $\omega<\omega_\xi$ and crosses over to $1/f$ noise for $\omega>\omega_\xi$. The crossover frequency ω_ξ vanishes as the transition is approached from above as $\omega_\xi\propto\xi^{-z}$, where ξ is the correlation length and $z\approx 2$ is the dynamic exponent. All the data obtained at different temperatures collapse to a single scaling curve when plotted as a function of ω/ω_ξ. The problem was studied by numerical simulations[13,14] of both the time-dependent Ginzburg–Landau (TDGL) and the resistive shunted junction (RSJ) models.

In this letter we study theoretically the flux noise in the TDGL model near the BKT transition. We determine the scaling function of the flux noise analytically in the limit in which the SQUID size is much smaller than the correlation length.

In order to study the flux noise we map the XY model with a local damping onto a 2D (dynamic) Coulomb gas.[15] We determine the dynamic correlation functions using an improved Debye–Hückel (DH) approach for the Coulomb gas in the same spirit as in Ref. 16.

The Euclidean action for the XY model with local damping for the phases φ is

$$S[\varphi]=E_J\int_0^\beta d\tau\sum_{\langle ij\rangle}[1-\cos(\varphi_i(\tau)-\varphi_j(\tau))] + \frac{\alpha}{8\beta^2}\int_0^\beta d\tau d\tau'\sum_i\left(\frac{\varphi_i(\tau)-\varphi_i(\tau')}{\sin[\pi(\tau-\tau')/\beta]}\right)^2, \tag{2}$$

where E_J is the Josephson coupling between neighboring sites. The local Ohmic damping introduces an interaction of the phase of a single grain at different times. In proximity-coupled arrays, which consist of superconducting island on top of a metallic film, the local damping parameter α is related to the shunting resistance R of one island to the substrate, $\alpha=h/4e^2R$.

A Villain transformation[17] is used to derive an effective dynamic action for the vortices. Here we follow the method described in Ref. 18 and obtain the dynamic action for the vortex degrees of freedom $v_i(\tau)$:

$$S[v]=\frac{1}{2}\int_0^\beta d\tau d\tau'\sum_{i,j} v_i(\tau)D_{ij}(\tau-\tau')v_j(\tau'). \tag{3}$$

The kernel D has the form

$$D(k,\omega_\mu)=\frac{4\pi^2 E_J}{k^2}\,\frac{k^2+2|\omega_\mu|/\omega_\alpha}{k^2+|\omega_\mu|/\omega_\alpha}, \tag{4}$$

with $\omega_\alpha=2\pi E_J/\alpha$, and ω_μ are the Matsubara frequencies. We choose the lattice spacing as the unit of length scales. In the static case this yields the standard 2D Coulomb gas.

The evaluation of the flux noise is done by means of a two-step procedure in the spirit of Ref. 16. i) The physics taking place at length scales shorter than ξ is taken into account by using the scaling properties of the flux noise. ii) At a scale of the order of the correlation length, all the dipoles have been integrated out, and, since the physics above T_{BKT} is dominated by screening, a DH approximation (with renormalized parameters) is used.[19,16]

The effect of bound pairs up to distances of the order of the correlation length can be taken into account by means of the scaling behavior of the flux noise

$$S_\Phi(\omega,l,T')=e^{z\delta}S_\Phi(\omega e^{z\delta},le^{-\delta},T'(\delta))\,. \tag{5}$$

At $\delta^*=\ln(\xi/\xi_0)$ all the vortices are integrated out up to a distance of the order of ξ. At this scale only free vortices are present, and the DH approximation can be used to calculate the right-hand side of Eq. (5).

The effect of screening due to the presence of free vortices above T_{BKT} is analyzed in the DH approximation. The Matsubara Green's function for the vortices in this approximation is

$$G(k,\omega_\mu)=\langle v\,v\rangle_{k,\omega_\mu}=\frac{1}{4\pi^2E_J\xi^2+D(k,\omega_\mu)}. \tag{6}$$

The Kosterlitz correlation length ξ diverges exponentially near the transition, $\xi=\xi_0\exp(b/\sqrt{T'-T'_{\mathrm{BKT}}})$, with $T'=T/E_J$ (Refs. 2, 7, and 20). An analytical continuation ($|\omega_\mu|\to -i\omega$) yields the retarded vortex propagator $G^R(k,\omega)=G(k,|\omega_\mu|\to -i\omega)$, which is related to the spectral function of vortex density–density correlations by the fluctuation-dissipation theorem $\langle v\,v\rangle_{k,\omega}=\mathrm{Im}\,G^R(k,\omega)\,2T/\omega$, for $\omega\ll T$. This correlation function describes the equilibrium vortex fluctuations in the system and gives rise to the flux noise.

Experiments on the magnetic flux noise detect the fluxes of the vortices from an effective area l^2 (Refs. 6–8). The relevant quantity is the vortex density fluctuation integrated over the pick-up area $\Phi(t)=\int_l d^2x\,v(\mathbf{x},t)$. After having performed the analytical continuation and by combining the scaling arguments (see Eq. (5)) with the DH approximation (see Eq. (6)), we obtain the flux-noise spectrum

$$S_\Phi(\omega)=\Phi_0^2e^{z\delta^*}S_{\Phi,\mathrm{DH}}(\omega e^{z\delta^*},le^{-\delta^*},T'(\delta^*))=\frac{\mathcal{C}\Phi_0^2}{8\pi^3}\,\frac{T'(\delta^*)l^4}{\omega\xi^4}F\left(x=\frac{\omega}{\omega_\xi},y=\frac{4\pi\xi^2}{l^2}\right), \tag{7}$$

where the subscript DH means at at this scale the flux noise can be evaluated by means of the Debye–Hückel approximation. The constant $\mathcal{C}$ takes into account the geometrical details of the experimental setup. We introduced the scaling function F:

$$F\left(x=\frac{\omega}{\omega_\xi}, y=\frac{4\pi\xi^2}{l^2}\right)=-\mathrm{Im}\int_0^y dz\left[1+z\frac{z-ix}{z-2ix}\right]^{-1}, \tag{8}$$

where characteristic frequency is $\omega_\xi=\omega_0(\xi_0/\xi)^2$ (we used a hard cutoff in k space to integrate over the pick-up coil area). The dynamic exponent $z=2$ directly emerges. The frequency scale ω_0 is related to microscopic parameters, $\omega_0=2\pi E_J/(\xi_0^2\alpha)$. The scale of the correlation length, ξ_0, is of the order of the lattice spacing. Close to the transition ($\xi\to\infty$) the scaling function F reduces to

$$F(x,y\to\infty)=\mathrm{Im}\frac{1+3ix}{2Q(x)}\ln\left(\frac{1-ix+Q(x)}{1-ix-Q(x)}\right)-\frac{\pi}{4}, \tag{9}$$

where $Q(x)^2=1-x^2+6ix$. The flux noise in the relevant limits is given by

$$\omega S_\Phi(\omega)\sim\begin{cases}\dfrac{\mathcal{C}\Phi_0^2}{8\pi^3}\dfrac{T'(\delta^*)l^4}{\xi^4} & \text{for } \dfrac{\omega}{\omega_\xi}\gg 1\\[2ex] \dfrac{\mathcal{C}\Phi_0^2}{8\pi^3}\dfrac{T'(\delta^*)l^4}{\xi^4}\dfrac{\omega}{\omega_\xi} & \text{for } \dfrac{\omega}{\omega_\xi}\ll 1\,.\end{cases} \tag{10}$$

The white noise occurs for frequencies $\omega<\omega_\xi$, and $1/f$ noise for $\omega>\omega_\xi$. The $1/f$ noise stems from the superposition of Lorentzian-shaped contributions at all length scales down to the dimension of the SQUID. For finite ξ the $1/f$ noise crosses over to a $1/f^2$ noise. The $1/f$ noise is intermediate in the frequency range $1<\omega/\omega_\xi<4\pi\xi^2/l^2$. Close to the transition this range exceeds several orders of magnitude.

We finally apply our results to the experiment by Shaw *et al.*[7] The critical coupling in the experiment is $T'_{\mathrm{BKT}}=0.06$, and thus the bare fugacity at criticality is $y_0=0.35$. Assuming that the bare fugacity is only weakly temperature dependent, the numerical iteration of the renormalization group equations gives to a good approximation $T'(\delta)\propto\exp(4\delta)$, as upon renormalization the limit $T'(\delta)\gg 2/\pi$ is reached, where $y(\delta)\propto\exp(2\delta)$ (this scaling behavior reflects the fact that the vortex-pair density is constant). Thus $T'(\delta^*)/\xi^4$ is temperature independent, and we can identify our scaling function F with the experimental scaling behavior. These last considerations should be regarded more as additional assumptions whose validity is based mainly on comparison with quantitative experimental data. The characteristic frequency was found to be $f_0=2.1\times10^6$ Hz. With the estimate $E_J=10$ K we can extract $\xi_0^2\alpha=10^6$, corresponding to Ohmic shunts to ground with a resistance $R=6\ \mathrm{m}\Omega\times\xi_0^2$. We expect ξ_0 to be of the order of one lattice spacing. Yet another possibility is to determine the resistance R and deduce the value of ξ_0. The effective shunting resistance of one island to infinity can be estimated be of the order of $10\ \mathrm{m}\Omega$. This also yields the scale of the correlation length to be of the order of one lattice spacing.

In summary, we have calculated the flux noise above the BKT transition and derived its scaling behavior analytically in the case where the correlation length exceeds the size of the pick-up loop. We find a crossover from white to $1/f$ noise. We related the crossover frequency to microscopic parameters of the array. Our results may explain recent experiments by Shaw *et al.*[7]

We are indebted to T. J. Shaw for useful conversations and for helping us compare our work with the experiment. We would like to thank J. Clarke, D.-H. Lee, P. Minnhagen, Gerd Schön, A. Schmid, and M. Tinkham for fruitful discussions. This work was supported by ''SFB 195'' of the ''Deutsche Forschungsgemeinschaft'' and the EU-grant TMR-FMRX-CT-97-0143.

[1] V. L. Berezinskiĭ, Zh. Éksp. Teor. Fiz. **59**, 207 (1970) [Sov. Phys. JETP **32**, 493 (1971)].
[2] J. M. Kosterlitz and D. J. Thouless, J. Phys. C **6**, 1181 (1973); J. M. Kosterlitz, J. Phys. C **7**, 1046 (1974).
[3] *Proceedings of the NATO ARW on Coherence in Superconducting Networks*, edited by J. E. Mooij and G. Schön, Physica B **152**, 1 (1988); *Proceedings of the ICTP Workshop on Josephson Junction Arrays*, edited by. H. A. Cerdeira and S. R. Shenoy, Physica B **222**, 253 (1996).
[4] D. J. Resnik, J. C. Garland, J. T. Boyd *et al.*, Phys. Rev. Lett. **47**, 1542 (1981); D. W. Abraham, C. J. Lobb, M. Tinkham, and T. M. Klapwijk, Phys. Rev. B **26**, 5268 (1982); H. S. J. van der Zant, H. A. Rijken, and J. E. Mooij, J. Low Temp. Phys. **82**, 67 (1991).
[5] Ch. Lehmann, Ph. Lerch, G.-A. Racine, and P. Martinoli, Phys. Rev. Lett. **56**, 1291 (1986).
[6] R. Théron, J.-B. Simond, Ch. Lehmann *et al*., Phys. Rev. Lett. **71**, 1246 (1993).
[7] T. J. Shaw, M. J. Ferrari, L. L. Sohn *et al.*, Phys. Rev. Lett. **76**, 2551 (1996).
[8] Ph. Lerch, Ch. Lehmann, R. Théron, and P. Martinoli, Helv. Phys. Acta **65**, 389 (1992).
[9] H. Beck, Phys. Rev. B **49**, 6153 (1994).
[10] S. E. Korshunov, Phys. Rev. B **50**, 13616 (1994).
[11] J. Houlrik, A. Jonsson, and P. Minnhagen, Phys. Rev. B **50**, 3953 (1994); K. Holmlund and P. Minnhagen, Phys. Rev. B **54**, 523 (1996).
[12] M. Capezzali, H. Beck and S. R. Shenoy, Phys. Rev. Lett. **78**, 523 (1997).
[13] P. H. E. Tiesinga, T. J. Hagenaars, J. E. van Himbergen, and J. V. Jose, Phys. Rev. Lett. **78**, 519 (1997).
[14] I.-J. Hwang, S. Ryu, and D. Stroud, http://xxx.lanl.gov/abs/cond-mat/9704108.
[15] P. Minnhagen, Rev. Mod. Phys. **59**, 1001 (1987).
[16] This procedure was developed to study the specific heat and the superfluid density above T_{BKT} in A. N. Berker and D. R. Nelson, Phys. Rev. B **19**, 2488 (1979).
[17] J. Villain, J. Phys. (Paris) **36**, 581 (1975).
[18] R. Fazio and G. Schön, Phys. Rev. B **43**, 5307 (1991).
[19] B. I. Halperin and D. R. Nelson, J. Low Temp. Phys. **36**, 599 (1979).
[20] This exponential temperature dependence of the correlation length may not directly reflect the critical BKT-behavior in a strict renormalization group sense, as was pointed out by P. Minnhagen and P. Olsson, Phys. Rev. B **45**, 10557 (1992).

Published in English in the original Russian journal. Edited by Steve Torstveit.

On the stability of localized states in nonlinear field models with Lifshitz invariants

A. Bogdanov[a)]

Donetsk Physicotechnical Institute, Ukrainian National Academy of Sciences, 340114 Donetsk, Ukraine

(Submitted 7 July 1998)
Pis'ma Zh. Éksp. Teor. Fiz. **68**, No. 4, 296–298 (25 August 1998)

The static solutions for a nonlinear vector field in models with Lifshitz invariants are investigated. It is shown that in such systems two- and three-dimensional localized states, associated with the relaxation of the modulus of the vector field, are radially unstable. © *1998 American Institute of Physics.* [S0021-3640(98)00916-5]

PACS numbers: 71.23.An, 61.72.Bb, 71.55.−i

Static localized states on defects of a crystal structure in cubic magnets without a center of inversion were investigated theoretically in Ref. 1. Specifically, solutions were obtained for two- (2D) and three-dimensional (3D) localized states at temperatures above the paramagnet–helicoid phase transition temperature. In these structures the modulus of the magnetization vector $\mathbf{m}(\mathbf{r})$ decreases continuously from finite values at the center to zero in the paramagnetic matrix. In the present letter it is shown that such solutions are radially unstable. Moreover, it can be proved for quite general field models with Lifshitz invariants that static localized states which are nonuniform with respect to the modulus of the vector $\mathbf{m}$ and possess spatial nonuniformities of dimension $n \geqslant 2$ are unstable.

Let us consider the vector field $\mathbf{m}(\mathbf{r})$ with the interaction functional

$$\Phi = \int \left[A\left(\frac{\partial m_i}{\partial x_k}\right)^2 + D_{ijk}\left(m_i \frac{\partial m_j}{\partial x_k} - m_j \frac{\partial m_i}{\partial x_k}\right) + f(m_i)\right] d^n x. \tag{1}$$

The first term in Eq. (1) characterizes the stiffness of the system and the second term includes a sum of antisymmetric products linear in the first spatial derivatives (Lifshitz invariants) and describes specific interactions occurring in systems without a center of inversion. Such interactions are encountered in certain classes of magnets,[2] ferroelectrics,[3] and liquid crystals,[4] and they can also be induced in a number of other systems.[5,6] Specifically, for cubic ferromagnets without a center of inversion and cholesterics this part of the functional has the form $\mathbf{m}\,\mathrm{curl}\,(\mathbf{m})$.[4,7] Finally, the last term in Eq. (1) describes uniform interactions in the system.

We shall take multidimensional localized states of the vector field $\mathbf{m}(\mathbf{r})$ to mean nonsingular distributions $\tilde{\mathbf{m}}(\mathbf{r})$ which are extremals of the functional (1), are nonuniform along more than one spatial coordinate ($n \geqslant 2$), and relax at large distances to some equilibrium value. We shall also assume that the energy contributions of different inter-

actions in Eq. (1), taken in the space of variation of the solutions $\tilde{\mathbf{m}}(\mathbf{r})$, also possess finite values:

$$I_A^{(n)}=\int A\left(\frac{\partial\tilde{m}_i}{\partial x_k}\right)^2 d^nx, \quad I_D^{(n)}=\int D_{ijk}\left(\tilde{m}_i\frac{\partial\tilde{m}_j}{\partial x_k}-\tilde{m}_j\frac{\partial\tilde{m}_i}{\partial x_k}\right)d^nx, \quad I_f^{(n)}=\int f(\tilde{m}_i)d^nx, \tag{2}$$

To calculate the multidimensional localized structures and check their stability it is necessary to solve a system of nonlinear differential equations. However, analysis of the energy (1) for deformations of the extremals of the type $\tilde{\mathbf{m}}(\mathbf{r})\rightarrow\tilde{\mathbf{m}}(\mathbf{r}/a)$ (where a is some positive number) makes it possible to draw definite conclusions about the stability of specific structures. In this manner it was proved that there are no multidimensional localized solutions for functionals of a quite general form (the Hobard–Derrick theorem;[8] see also Ref. 9). In Refs. 10 and 11 it was shown that this theorem is inapplicable to functionals containing terms which are linear in the first spatial derivatives. The solutions obtained for 2D localized structures in a number of noncentrosymmetric magnets (magnetic vortices)[10,12,13] as well as in chiral liquid crystals (axial structures)[14] demonstrate that invariants which are linear in the first spatial derivatives play a determining role in the stabilization of such states. To date such 2D localized structures have been observed in the chiral magnet NiMn.[15]

Let us now investigate the stability of localized states which are nonuniform in the modulus of the vector $\mathbf{m}$. We write the energy (1) for 2D ($n=2$) and 3D ($n=3$) vector configurations $\mathbf{m}(\mathbf{r})=\tilde{\mathbf{m}}(\mathbf{r})/(1+k)$:

$$\Phi=\Phi(\tilde{\mathbf{m}}(\mathbf{r}))+(I_D^{(2)}+2I_f^{(2)})k+I_f^{(2)}k^2, \tag{3}$$

$$\Phi=\Phi(\tilde{\mathbf{m}}(\mathbf{r}))+(I_A^{(3)}+2I_D^{(3)}+3I_f^{(3)})k+(I_D^{(3)}+3I_f^{(3)}))k^2+I_f^{(3)}k^3, \tag{4}$$

For the extremals $\tilde{\mathbf{m}}(\mathbf{r})$ to be stable, the coefficients of the terms linear in k in Eqs. (3) and (4) must equal zero, while the coefficients of the quadratic terms must be positive. It follows from these conditions as well as the positivity of $I_A^{(3)}$ that a necessary condition for 2D and 3D localized states to be stable is that the energy contribution associated with invariants which are linear in the first spatial derivatives must be negative ($I_D^{(n)}<0$).[10,11] Two-dimensional localized structures with $I_D^{(2)}=0$ require a special analysis. In this case, according to Eq. (3), the energy (1) for the vector configurations $\mathbf{m}(\mathbf{r})=\tilde{\mathbf{m}}(\mathbf{r})/(1+k)$ which are not solutions of the Euler equations equals the energy for the extremals $\tilde{\mathbf{m}}(\mathbf{r})$, which bring it to a state with a lower energy, and therefore these solutions are unstable.

Introducing spherical coordinates for $\mathbf{m}=(m\sin(\theta)\cos(\psi),\ m\sin(\theta)\sin(\psi),\ m\cos\theta)$, the functional (1) can be represented as

$$\Phi=\int[A(\partial m/\partial x_k)^2+G(m,\theta,\psi,\theta_{x_k},\psi_{x_k})]d^nx. \tag{5}$$

By virtue of the structure of the Lifshitz invariants the functional (5) has no terms which are linear in $(\partial m/\partial x_k)$. For this reason one has $I_D^{(n)}=0$ for deformations of the type $m(\mathbf{r})\rightarrow m(\mathbf{r}/a)$ in expressions (3) and (4), and therefore these localized states are unstable.

Thus the stability of multidimensional localized states in noncentrosymmetric systems is due to the stabilizing role of interactions described by Lifshitz invariants. Since these interactions depend on the spatial derivatives of the angular variables of the vector field and do not depend on the derivatives of the modulus of **m**, only multidimensional localized structures which are nonuniform with respect to the angular variables can be stable. This is confirmed by calculations of 2D localized states in specific systems.[10–14]

I thank the Alexander von Humboldt Foundation for financial support and S. V. Tarasenko for a discussion of this work.

[a)]e-mail: bogdanov@host.dipt.donetsk.ua

[1] A. Buzdin and Y. Meurdeşoif, JETP Lett. **65**, 814 (1997).
[2] I. E. Dzyaloshinskiĭ, Zh. Éksp. Teor. Fiz. **46**, 1420 (1964) [Sov. Phys. JETP **19**, 960 (1964)].
[3] R. Blink and A. P. Levanyuk, *Incommensurate Phases in Dielectrics*, North-Holland, Amsterdam, 1986.
[4] P. G. de Gennes and J. Prost, *The Physics of Liquid Crystals*, Clarendon Press, Oxford, 1993.
[5] T. M. Giebultowicz, H. Luo, N. Samarth *et al.*, IEEE Trans. Magn. **MAG-29**, 3383 (1993).
[6] A. Fert and P. M. Levy, Phys. Rev. Lett. **44**, 1538 (1980).
[7] P. Bak and M. H. Jensen, J. Phys. C: Solid State Phys. **13**, L881 (1980).
[8] G. H. Derrick, J. Math. Phys. **5**, 1252 (1964).
[9] V. G. Makhan'kov, Yu. P. Rybakov, and V. I. Sanyuk, Usp. Fiz. Nauk **164**, 121 (1994).
[10] A. N. Bogdanov and A. Hubert, Phys. Status Solidi B **186**, 527 (1994).
[11] A. Bogdanov, JETP Lett. **62**, 247 (1995).
[12] A. N. Bogdanov and D. A. Yablonskiĭ, Zh. Éksp. Teor. Fiz. **95**, 178 (1989) [Sov. Phys. JETP **68**, 101 (1989)]; A. N. Bogdanov, M. V. Kudinov, and D. A. Yablonskiĭ, Fiz. Tverd. Tela (Leningrad) **31**, 99 (1989) [Sov. Phys. Solid State **31**, 1707 (1989)].
[13] A. N. Bogdanov and A. Hubert, J. Magn. Magn. Mater. **138**, 255 (1994).
[14] A. N. Bogdanov and A. A. Shestakov, Fiz. Nizk. Temp. **23**, 1024 (1997) [Low Temp. Phys. **23**, 769 (1997)]; Zh. Éksp. Teor. Fiz. **113**, 1675 (1998) [JETP **86**, 911 (1998)].
[15] T. Ando, E. Ohta, and T. Sato, J. Magn. Magn. Mater. **163**, 277 (1996).

Translated by M. E. Alferieff

The effects of nonequilibrium charge distribution in scanning tunneling spectroscopy of semiconductors

P. I. Arseyev
P. N. Lebedev Physics Institute, Russian Academy of Sciences, 117924 Moscow, Russia

N. S. Maslova and S. V. Savinov
Department of Physics, Moscow State University, 119899 Moscow, Russia

(Submitted 3 June 1998; resubmitted 8 July 1998)
Pis'ma Zh. Éksp. Teor. Fiz. **68**, No. 4, 299–304 (25 August 1998)

Results are presented from a low-temperature scanning tunneling microscopy (STM) investigation of III–V semiconductor surfaces cleaved *in situ* along a (110) plane. The STM topographic images reveal the presence of surface charge structures. The possibility of their observation depends on the charge state of the apex of the STM tip. Peaks are also observed in the local tunneling conductivity spectra. The energy position of these peaks and the energy position of the edges of the band gap change with distance from the defect. A theoretical model is proposed which demonstrates that the experimental scanning tunneling spectroscopy (STS) data can be explained by effects due to a nonequilibrium electron distribution in the contact area, which gives rise to localized charges. In this model the on-site Coulomb repulsion of localized charges and their interaction with semiconductor electrons are treated self-consistently. © *1998 American Institute of Physics.* [S0021-3640(98)01016-0]

PACS numbers: 68.35.Bs, 07.79.Cz, 61.16.Ch, 81.05.Ea

For a clear understanding of the experimental results, the STM topographic images of surface defects at different values of the tunneling bias voltage must be compared directly with the local spectroscopy data.[1] We present the results of low-temperature STM/STS investigations of atomic defects on the GaAs (110) surface at 4.2 K. The experimental procedure is described in Ref. 2. We have used GaAs single crystals heavily doped with Te ($n=5\times10^{17}\,\mathrm{cm}^{-3}$). The typical STM topography of an atomic defect is depicted in the inset in Fig. 1. According to the common view,[3] this type of defect is a dopant atom residing on the surface.

Normalized conductivity curves measured by means of current-imaging tunneling spectroscopy (CITS) around this kind of atomic defect are presented in Fig. 1. Let us mention the main features of the tunneling conductivity curves. The measured band gap edges are shifted by approximately 200 meV near the defect as compared to the flat surface region. A set of peaks around the defect, which are absent above the flat surface, exists in the voltage range from -1 V to 0 V. There is a peak of the tunneling conductivity in the bias range from -1.5 V to -1 V. The position and height of this peak

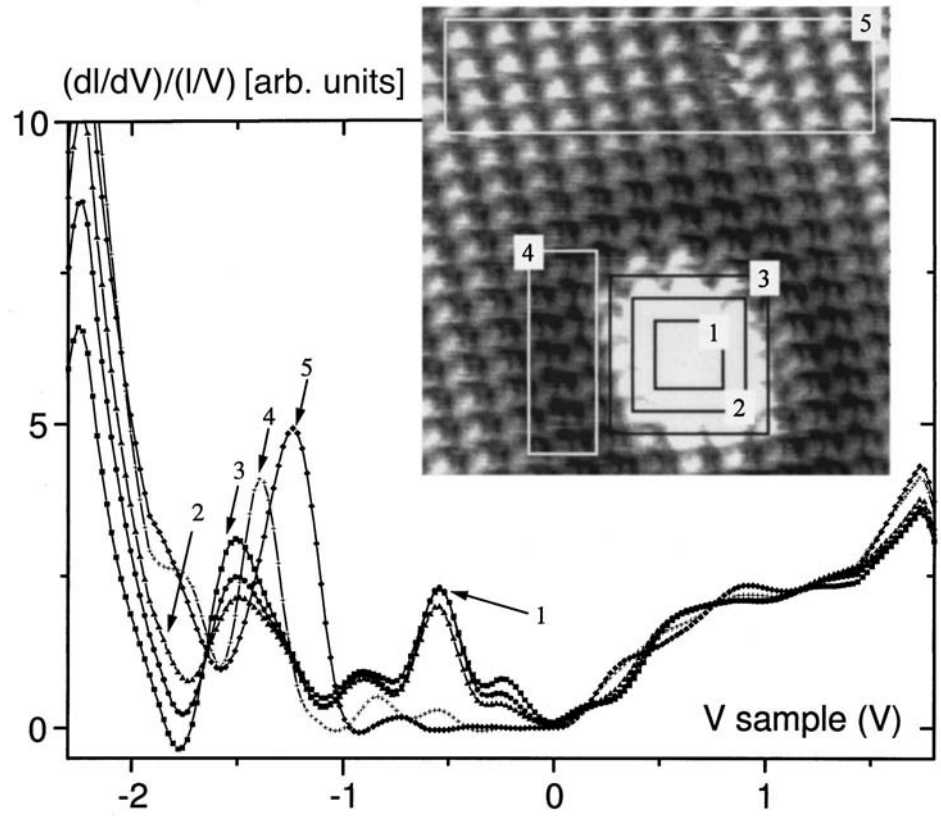

FIG. 1. Tunneling conductivity spectra measured near a tellurium atom residing on the *in situ* cleaved (110) GaAs surface at a temperature of 4.2 K. The inset shows the STM image of the 5.8 nm×5.8 nm surface area from which the spectroscopic data were acquired. Each tunneling conductivity curve is the result of averaging and subsequent numerical differentiation over the surface area which is marked by numbers on the STM topogram.

depend on the distance from the defect; this peak does not disappear above the flat surface region.

We assume that the tunneling conductivity peaks in the band gap can be attributed to the Coulomb interaction of the electrons of the sample and induced charges localized both on the STM tip apex and near the defect. We suppose that in this situation the on-site Coulomb repulsion of localized electrons (Hubbard repulsion) is also very important. Such an interaction can change the energy values considerably even for deep impurity levels. As a result, there is a strong dependence of the level energy on the tunneling bias voltage. The experimentally measured position of the peak of the tunneling conductivity does not coincide with the bulk value of the unperturbed energy levels of the doping impurity.

We have proposed a self-consistent theory for tunneling processes in an STM junction in the presence of impurity states. Various experimental situations can be considered in the framework of this theory. The impurity level can be associated with a surface

defect or with a defect in an intermediate layer. The impurity level can also be connected with several atoms or even a single atom on the apex of the STM tip. The proposed theoretical approach includes the following main points. At low temperature and small contact size the steady-state electron distribution is not the thermal equilibrium distribution because of the finite relaxation rate of tunneling electrons.[5] STM/STS measurements can be strongly influenced by a nonuniform charge distribution and the corresponding additional Coulomb interaction.[1,2] In general, in low-dimensional systems considerable modification of the initial electron spectrum occurs due to the tunneling process itself,[4] and charge effects could become very important.

To describe the tunneling processes in an STM junction in the presence of a localized state we use a model which includes three subsystems: an ideal semiconductor, a localized electronic level-surface impurity or tip apex state, and a normal metal (STM tip). These subsystems are coupled by tunneling matrix elements. We add an interaction of the semiconductor with a heat bath in order to describe finite-relaxation-rate effects. The Hamiltonian $\hat{H}$ of the model is thus

$$\hat{H}=\hat{H}_{sc}+\hat{H}_{d}+\hat{H}_{m}+\hat{H}_{tun}+\hat{H}_{int}+\hat{H}_{hb}\,, \tag{1}$$

where $\hat{H}_{sc}$ is the Hamiltonian of the pure semiconductor:

$$\hat{H}_{sc}=\sum_{\mathbf{k},\sigma}\,(\varepsilon_{k}-\mu)c^{+}_{\mathbf{k},\sigma}c_{\mathbf{k},\sigma}\,, \tag{2}$$

$c_{\mathbf{k},\sigma}$ is the annihilation operator for an electron with momentum $\mathbf{k}$ and spin σ, and μ is the Fermi energy in the semiconductor.

The part $\hat{H}_{d}$ corresponds to the impurity state and takes into account the Hubbard repulsion:

$$\hat{H}_{d}=\varepsilon_{d}\sum_{\sigma}\,d^{+}_{\sigma}d_{\sigma}+U/2\sum_{\sigma}\,n^{d}_{\sigma}n^{d}_{-\sigma}\,, \tag{3}$$

where $n^{d}_{\sigma}=d^{+}_{\sigma}d_{\sigma}$, the operator d_{σ} annihilates an impurity electron with spin σ, and ε_{d} is the impurity energy level (which in the general case is dependent on the bias V). The part $\hat{H}_{int}$ describes the tunneling between the semiconductor and the impurity state:

$$\hat{H}_{int}=T\sum_{\mathbf{k},\sigma}\,(c^{+}_{\mathbf{k},\sigma}d_{\sigma}+\text{h.c.}), \tag{4}$$

with an interaction matrix element T.

The Hamiltonian of the metal tip $\hat{H}_{m}$ is

$$\hat{H}_{m}=\sum_{\mathbf{p},\sigma}\,(\varepsilon_{p}-\mu-eV)a^{+}_{\mathbf{p},\sigma}a_{\mathbf{p},\sigma}\,, \tag{5}$$

where $a_{\mathbf{p},\sigma}$ is the annihilation operator for a tip electron with momentum $\mathbf{p}$ and spin σ, and V is the applied bias voltage.

The part $\hat{H}_{tun}$ corresponds to the impurity–metal-tip hopping (tunneling) term with matrix element T':

$$\hat{H}_{tun} = T' \sum_{\mathbf{p},\sigma} (a^{+}_{\mathbf{p},\sigma} d_{\sigma} + \text{h.c.}). \tag{6}$$

Finally, $\hat{H}_{hb}$ describes the interaction of the semiconductor electrons with a heat bath, which leads to a finite relaxation time of nonequilibrium electrons. The kind of heat bath is not crucial for our purposes and we choose the simplest form:

$$\hat{H}_{hb} = \sum_{\mathbf{k},\mathbf{p}',\sigma} T''(\mathbf{k}-\mathbf{p}')(c^{+}_{\mathbf{k},\sigma} b_{\mathbf{p}',\sigma} + \text{h.c.}), \tag{7}$$

where $b_{\mathbf{p}',\sigma}$ is the annihilation operator for a heat bath electron with momentum $\mathbf{p}'$ and spin σ, and $T''(r)$ is the effective interaction with the heat bath.

As we have said, an additional charge associated with localized states in the contact area can appear if the finite relaxation rate is taken into account. The influence of this charge on the tunneling characteristics can be considered self-consistently in the following way.[6]

a) The Coulomb interaction of the Hubbard type is treated self-consistently in the mean-field approximation. The characteristic scales of the STM junction and the possible radius of a localized state on the apex of the tip have values $a_0 \simeq 5-10$ Å. Thus the Coulomb repulsion $U = e^2/a_0$ should have a value of the order of the semiconductor band gap (0.5–1.0 eV), which is much smaller than bandwidths of the semiconductor and the metallic tip. Thus we suppose that the constraint on double occupancy (of a localized state) is not essential for our problem. It is well known that Coulomb correlations in Hubbard-type systems begin to play a significant role only if U is greater than the bandwidth. For smaller U the mean-field approximation gives satisfactory results. Thus the Coulomb interaction leads to a dependence of the localized state energy on the additional charge density: $\varepsilon_d = \varepsilon_d^0 + U\delta n_d$, where U presumed to lie in the region 0.5–1 eV.

b) A potential W is introduced to describe the interaction of semiconductor electrons with the additional charge δn_d present on the localized state. The corresponding interaction Hamiltonian has the form

$$\hat{H}_W = \sum_{\mathbf{k},\mathbf{k}'} W(\mathbf{k}-\mathbf{k}') c^{+}_{\mathbf{k},\sigma} c_{\mathbf{k}',\sigma}. \tag{8}$$

Exact calculation of the electrostatic potential W is possible only if the exact geometry of the contact is known. Usually the details of the shape of the tip apex and, consequently, the spatial distribution of the electric field cannot be determined. Nevertheless, there are two possible cases for which the analysis can be simplified. If the charge screening in the semiconductor is weak, the effective radius R of the potential is much greater than the interatomic distance $R \gg a$. Then $W(\mathbf{k}-\mathbf{k}') = w \times \delta n_d \delta_{k,k'}$, with the parameter w determined by the particular contact configuration. The potential is almost constant at distances greater than the contact area. This case is similar to band-bending effects in planar tunnel junctions in the presence of an applied bias. In such a situation one can observe a shift of the gap edges in tunneling experiments.[7] The other case is encountered if the geometry of the contact or strong screening in the semiconductor leads to a point-like effective potential — the effective radius R of the potential is of the order of the interatomic distance a. Then $W(\mathbf{k}-\mathbf{k}') = w \times \delta n_d$. In this case we are

interested in the point-like potential caused by the localized charge both on the apex of the STM tip and on semiconductor surface defects. For charge localized on the tip the constant w is determined by the distance from the tip to the semiconductor surface. Typical values of the tip–sample separation d in STM junctions do not exceed 10–15 Å. Thus the simplest estimate of the Coulomb potential (e^2/d) at the semiconductor surface yields $w \simeq 0.3$–0.5 eV. In any case Coulomb effects should be taken into account, because the tip–sample separation and typical radius of a localized state are comparable to the interatomic distance. The extra charge on a localized state and the tunneling conductivity of a system can be determined by means of a self-consistent approach based on a diagram technique for nonequilibrium processes.[8]

The tunneling conductivity $dI/dV(\omega)$ can be determined from the corresponding kinetic equations for Keldysh Green functions in terms of nonequilibrium occupation numbers $n_d(\omega)$ of the localized state:

$$dI/dV(\omega) = -4\gamma_0 \ \mathrm{Im}\ G^R_{d,d}(\omega)(n_d(\omega) - n^0_d(\omega)), \tag{9}$$

where $n^0_d(\omega)$ is the equilibrium occupation number of the localized state, and $G^{R(A)}_{d,d} \times(\omega)$ is the exact retarded (advanced) Green function of the localized state.

The sample and contact characteristics appear in the final expression for the tunneling conductivity as relaxation and kinetic constants (functions):

$$-i\gamma_0(\omega) = -i|T'|^2 \nu_{\mathbf{p}}(\omega) - i\gamma(\omega) = -i|T''|^2 \nu_{\mathbf{p}'}(\omega),$$

$$\Gamma_d = -\gamma_0 \,\mathrm{Im}\, G^R_{dd}\Gamma_k = -\gamma \sum_{\mathbf{k},\mathbf{k}'} \mathrm{Im}\, G^R_{\mathbf{k},\mathbf{k}'}\Gamma = T^2 \nu_k, \tag{10}$$

where ν_k is the conduction-band density of states, and $\nu_{\mathbf{p}}(\omega)$ and $\nu_{\mathbf{p}'}(\omega)$ are, respectively, the densities of states in the metallic tip and in the heat bath connected to the semiconductor.

The final expression for the tunneling conductivity after all substitutions can be written as

$$dI/dV(\omega) = \frac{2\Gamma_d\Gamma_k(\Gamma/T)(Z_2 + Z^0_2)}{\Gamma_d\Gamma_k + \Gamma_k(\Gamma/T)Z_2 + \Gamma_d(\Gamma/T)(Z^0_1 + Z^0_2 + Z_2)}(n^0_p(\omega) - n^0_k(\omega - eV)), \tag{11}$$

where $n^0_p(\omega)$ and $n^0_k(\omega - eV)$ are the equilibrium occupation numbers of the states of the semiconductor and metallic tip, respectively. The dimensionless functions Z are given by

$$Z^0_1 = 2\frac{\gamma}{T}\mathrm{Im}[(G^A_d(\omega)(\omega - \tilde{\varepsilon}_d) - 1)\alpha(\tilde{\varepsilon}_d)],$$

$$Z_2 = 2T \,\mathrm{Im}\, G^R_d(\omega)\mathrm{Im}(\alpha(\tilde{\varepsilon}_d)),$$

$$Z^0_2 = 2\gamma_0 T \,\mathrm{Im}\left[\left(G^R_d(\omega)\left(1 - i\gamma\frac{\omega - \varepsilon_d + i\gamma_0}{T^2}\right) + i\frac{\gamma}{T^2}\right)\frac{\alpha(\tilde{\varepsilon}_d) - \alpha(\omega)}{\omega - \tilde{\varepsilon}_d}\right],$$

$$\alpha(\omega) = \nu_k^{-1}\sum_{\mathbf{k}} \frac{1}{\omega - \varepsilon_{\mathbf{k}} + i\delta}, \tag{12}$$

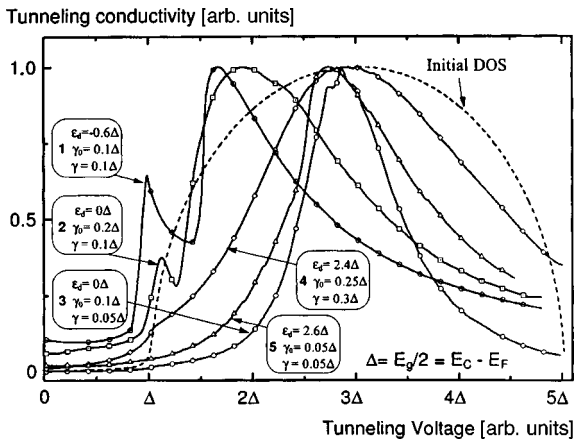

FIG. 2. Tunneling conductivity curves obtained numerically from Eq. (11) for different values of the STM junction parameters: the relaxation rate in the semiconductor γ, the relaxation rate on the localized state γ_0, and initial localized state energy ε_d^0. All quantities are measured in units of one-half the initial band-gap width Δ. The values of Coulomb parameters are: $U=2\Delta$, $w=\Delta$. The unperturbed initial model density of states is shown by the dotted curve.

where $\tilde{\varepsilon}_d=\varepsilon_d+i\gamma_0$.

The additional charge δn_d is determined self-consistently from the exact nonequilibrium occupation numbers and the density of states on the localized state. Both these parameters are functions of the applied bias voltage and the value of the additional charge, since they depend on $\varepsilon_d=\varepsilon_d^0+U\delta n_d$ and the Coulomb potential $W(\delta n_d)$ (Eq. (8)):

$$\delta n_d(V)=\int [(-1/\pi)\mathrm{Im}\, G_{d,d}^R(\omega,V)n_d(\omega,V)-(-1/\pi)\mathrm{Im}\, G_{d,d}^R(\omega,V=0)n_d^0(\omega,V=0)]. \tag{13}$$

The analytical expression for the dependence of the tunneling conductivity on the applied voltage for the two situations described was analyzed numerically. The results for typical parameter values (relaxation rates γ and γ_0, tunneling rate Γ, and initial impurity level ε_d^0) are depicted in Fig. 2. Two different situations were investigated: 1) ε_d^0 lies in the band gap (Fig. 2, curves *1–3*); 2) there is one or a few localized states in the conduction or valence band (Fig. 2, curves *4*,*5*). We present in Fig. 2 the results of calculations for the Coulomb parameters $U=1$ eV and $w=0.5$ eV. The qualitative behavioral features of the tunneling conductivity are insensitive to some variations of the Coulomb parameters within the regions estimated above. The initial model density of states for the semiconductor is shown by the dotted curve. It obviously differs from the tunneling conductivity curves that could be obtained in STS measurements. One can clearly see the shift of the gap edges, which becomes more pronounced with decreasing relaxation rates (Fig. 2, curves *4*,*5*). A nonequilibrium electron distribution leads to charge accumulation on a localized state, with initial energy ε_d^0. Because of Coulomb repulsion this results in a simultaneous change of its energy by an amount $\Delta\varepsilon$ which is comparable to the value of the band gap. In this situation a localized state is often

manifested as a peak occurring near the band edge (Fig. 2 curves *1,2*) regardless of its initial energy. Near the band edge the tunneling current grows rapidly with tunneling bias, thus strongly changing the localized charge. Such a peak can appear above the flat surface area if the localized state is associated with the apex of the STM tip. This can be seen from curve *1* in Fig. 1, which shows the experimental curves of the tunneling conductivity. The peak position is sensitive to variations of the characteristic parameters Γ, γ, γ_0, and ε_d, which determine the value of the additional charge. But the peak is not very sensitive to the position of the Fermi level relative to the band gap edges.

Our model can be generalized for situations in which there are several localized states ε_d^i associated both with the apex of the STM tip and with the defect.

As the charge accumulated in a localized state ε_d is determined by the relaxation and tunneling rates, it depends on the tip–sample and tip–defect separation. By changing the STM tip position one can obtain various tunneling conductivity curves with different peak positions. The shift of the gap edges and the tunneling conductivity peaks that are sensitive to changes in the tip position can be seen in Fig. 1. They can be qualitatively understood in terms of the proposed theoretical model.

The work performed in Moscow has been supported by the Russian Ministry of Research (Surface Atomic Structures, Grant 95-1.22; Nanostructures, Grant 97-1086) and the Russian Fund for Fundamental Research (RFFR, Grants 96-02-19640a and 96-02-16701a).

[1] N. S. Maslova, S. I. Oreshkin, V. I. Panov, S. V. Savinov *et al.*, JETP Lett. **67**, 146 (1998).
[2] N. S. Maslova, V. I. Panov, S. V. Savinov *et al.*, Phys. Low Dim. Struct., to be published.
[3] J. F. Zheng, X. Liu, N. Neuman *et al.*, Phys. Rev. Lett. **72**, 10, 1490 (1994).
[4] P. I. Arseev and N. S. Maslova, Zh. Eksp. Teor. Fiz. **102**, 1056 (1992) [Sov. Phys. JETP **75**, 575 (1992)].
[5] O. Agam, N. S. Wingreen, and B. L. Altshuler, Phys. Rev. Lett. **78**, 1956 (1997).
[6] P. I. Arseev, N. S. Maslova, V. I. Panov, and S. V. Savinov, ''Role of charge effects in tunneling investigations of semiconductors,'' *Semiconductors-97,* Moscow, December 1–5, 1997.
[7] R. M. Feenstra and J. A. Stroscio, J. Vac. Sci. Technol. B **5**, 923 (1987).
[8] L. V. Keldysh, Zh. Eksp. Teor. Fiz. **47**, 1515 (1964) [Sov. Phys. JETP **20**, 1018 (1964)].

Published in English in the original Russian journal. Edited by Steve Torstveit.

Quantized Hall effect in disordered GaAs layers with 3D spectrum in tilted magnetic fields

S. S. Murzin

Grenoble High Magnetic Field Laboratory, Max-Planck-Institut für Festkörperforschung and Centre National de la Recherche Scientifique, B.P.166, F-38042 Grenoble Cedex 9, France; Institute of Solid State Physics, Russian Academy of Sciences, 142432 Chernogolovka, Moscow Region, Russia

I. Claus and A. G. M. Jansen

Grenoble High Magnetic Field Laboratory, Max-Planck-Institut für Festkörperforschung and Centre National de la Recherche Scientifique, B.P.166, F-38042 Grenoble Cedex 9, France

(Submitted 10 July 1998)
Pis'ma Zh. Éksp. Teor. Fiz. **68**, No. 4, 305–308 (25 August 1998)

The quantum Hall effect structure in the transverse magnetoresistance R_{xx} and the Hall resistance R_{xy} of heavily doped GaAs layers with a three-dimensional spectrum of the charge carriers is investigated for different field orientations. The characteristic structures (minima in R_{xx} and plateaus in R_{xy}) shift much more slowly to higher fields and are suppressed much more rapidly in comparison with the expected angular dependence for a two-dimensional system. The results are discussed in terms of the anisotropic change of the three-dimensional conductivity tensor with magnetic field rotation. © *1998 American Institute of Physics.* [S0021-3640(98)01116-5]

PACS numbers: 73.40.Hm, 72.80.Ey, 72.80.Ng

It is well known that in two-dimensional (2D) electron systems the Hall resistance R_{xy} and the Hall conductance G_{xy} are quantized such that $G_{xy}=1/R_{xy}=ie^2/h$ (i is an integer) due to the discrete energy spectrum of the charge carriers in a quantizing magnetic field.[1] In 2D electron systems with a high mobility, electron–electron correlations even lead to a quantum Hall effect (QHE) with fractional i. Recently, a quantization of the Hall conductance has been observed in disordered layers consisting of epitaxial layers of heavily doped *n*-type GaAs.[2] In this case, the electronic system is supposed to have a three-dimensional (3D) single-particle energy spectrum like that for the bulk material. At $T=4.2$ K, the magnetoresistance of the samples shows the typical behavior of the bulk material, with weak Shubnikov–de Haas oscillations with increasing field and a strong monotone upturn in the extreme quantum limit (EQL), where only the lowest Landau level is occupied. The bulk electron densities n determined from the periodicity of the Shubnikov–de Haas oscillations in reciprocal field were close to the nominal values. Below 1 K, the magnetic-field dependence of the Hall conductance G_{xy} shows steps at quantized values ie^2/h ($i=2,4,6$) together with pronounced minima in the transverse conductance G_{xx} in the extreme quantum limit of the applied magnetic field, while the

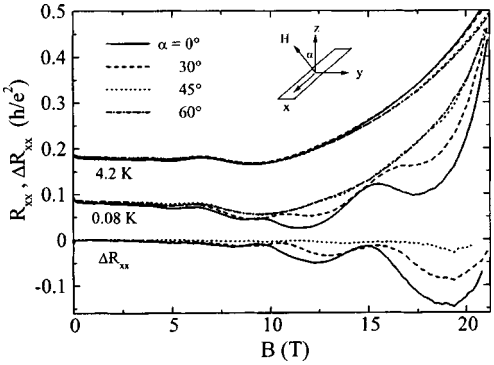

FIG. 1. Magnetic field dependence of the transverse resistance R_{xx} (per square) in magnetic fields at different angles α with respect to the normal of the GaAs layer at $T=4.2$ and 0.08 K. The curves for 4.2 K are shifted vertically by 0.1. ΔR_{xx} shows the difference $R_{xx}(\alpha)-R_{xx}(60°)$ at 0.08 K.

amplitude of the usual Shubnikov–de Haas oscillations does not depend on temperature below 4 K. The minima in G_{xx} and $|dG_{xy}/dH|$ appear in magnetic fields, where $G_{xy}=ie^2/h$ at $T=4$ K.

In this work we study this novel phenomenon of a quantized Hall effect in a disordered GaAs layer in a tilted magnetic field. This study allows for a comparison with the QHE in a 2D system, where the projection of the field perpendicular to the 2D electron system determines the effect in a tilted magnetic field (without taking spin-splitting effects into account). Our experiment reveals a strongly different dependence on the field orientation.

The investigated Si-doped GaAs layers sandwiched between undoped GaAs have been grown by molecular-beam epitaxy as described in Ref. 2. The quantized Hall effect structure has been observed for a perpendicular magnetic field in various samples with thicknesses about 100 nm and electron concentrations from 0.6 to 2.5×10^{17} cm^{-3} (Ref. 2). Here we will present experimental data for different field orientations measured at 4.2 and 0.08 K on a heavily doped GaAs layer (sample 2 in Ref. 2, which showed the most pronounced effect) with a nominal thickness $d=100$ nm, with a bulk electron density $n=1.5\times10^{17}$ cm^{-3} and mobility $\mu=2400$ cm^2/(V$\cdot$ s) at 4.2 K. The estimated mean free path $l=28$ nm and screening length $\lambda_D=7$ nm in zero magnetic field are smaller than the thickness of the layer. Sample 1, with a nominal thickness of 100 nm, a bulk density $n=0.6\times10^{17}$ cm^{-3} and mobility 1900 cm^2/(V$\cdot$ s) was measured only in parallel and perpendicular magnetic fields at $T=0.3$ and 4.2 K. The magnetoresistance R_{xx} and Hall resistance R_{xy} were measured in a Hall-bar geometry by a phase-sensitive detection method for several orientations α of the magnetic field with respect to the normal of the plane of the GaAs layer ($\alpha=0°$ corresponds to the perpendicular orientation). In our convention, the xyz coordinates refer to the frame of the layer. The applied current is along the x axis, the Hall contacts are along the y axis, and the z axis is perpendicular to the layer. The magnetic field is rotated perpendicular to the current direction (see the inset of Fig. 1). The measured resistance was converted to the resistance per square R_{xx} using the lateral dimensions of the Hall bar.

In Fig. 1 the transverse magnetoresistance R_{xx} of sample 2 is plotted for different

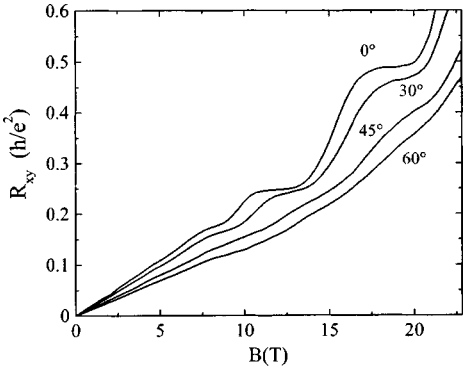

FIG. 2. Magnetic field dependence of the Hall resistance R_{xy} in a tilted magnetic field at different angles α at $T=0.08$ K.

angles α of the applied magnetic field with respect to the normal of the sample plane at temperatures $T=4.2$ K and 0.08 K. At 4.2 K, the characteristic Shubnikov–de Haas oscillations below 8 T and the strong increase in magnetoresistance in the EQL above 8 T are practically independent of the field direction. This is a strong indication of three-dimensionality of the electronic spectrum of the investigated system. At $\alpha=0°$ and $T=0.08$ K, the pronounced minima in R_{xx} coincide with the plateaus in R_{xy} shown in Fig. 2. These structures in the magnetoresistance tensor components resemble the QHE for a 2D electron system, although the plateaus in R_{xy} aren't completely flat nor do the minima in R_{xx} go to zero. As we have shown for samples with the same nominal thickness but different electron density,[2] the quantized structures occur at quantized values ie^2/h of the Hall conductance $G_{xy}=R_{xy}/(R_{xx}^2+R_{xy}^2)$ with $i=2,4,6$.

By rotating the magnetic field away from the perpendicular orientation both the plateaus in R_{xy} and the minima in R_{xx} are strongly suppressed simultaneously. In Fig. 3 we have plotted the field positions $B_{\min}(\alpha)/B_{\min}(0°)$ normalized by the 0° result as functions of the field orientation α. The field positions $B_{\min}(\alpha)$ were extracted from the

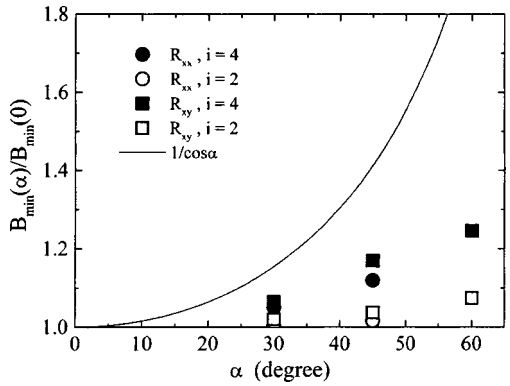

FIG. 3. Normalized magnetic field positions $B_{\min}(\alpha)/B_{\min}(0°)$ of the minima in ΔR_{xx} and dR_{xy}/dB as a function of the field inclination α. The solid curve shows the $1/\cos\alpha$ dependence.

minima in both $\Delta R_{xx}=R_{xx}(\alpha)-R_{xx}(60°)$ and dR_{xy}/dB. These field values are substantially smaller than the $1/\cos\alpha$ dependence expected for a 2D QHE. The discrepancy at higher magnetic fields is more pronounced for the structure at $i=2$ than for the $i=4$ structure. Because of the absence of a $1/\cos\alpha$ angular dependence of the quantized structures in the tensor components, we can exclude any trivial explanation of the observed phenomenon in terms of a hidden 2D electron system in our MBE grown structure.

For an explanation of the quantized phenomenon, we have suggested[2,3] the importance of diffusive corrections to the conductance due to electron–electron interaction.[4] These effects are strongly enhanced in the extreme quantum limit due to the decreasing diffusion perpendicular to the magnetic field and could possibly cause a correlation gap in the density of states at the Fermi level at the lowest temperatures. In the case that the corrections are small (at $T=4.2$ K in our case), the probability $P(t)$ of again finding two diffusing electrons within a distance of the order of the screening length in a time t is given for an anisotropic conductor by

$$P(t)\sim\frac{\lambda_D^3}{d(D_{xx}D_{yy})^{1/2}t}\propto(G_{xx}G_{yy})^{-1/2}, \tag{1}$$

where D_{xx} and D_{yy} are the diffusion coefficients. Within this description of electron–electron interactions in a disordered system, the effect in a rotated magnetic field would depend on the conductance average $\sqrt{G_{xx}(4.2)G_{yy}(4.2)}$. From our previous investigation of the phenomenon on different samples[2] in a perpendicular magnetic field, we concluded that the quantized structure is more pronounced the more closely the conductance $G_{xx}(4.2)=G_{yy}(4.2)$ at $T=4.2$ K comes down to the value e^2/h (Ref. 2). In a tilted field $G_{xx}(4.2)\neq G_{yy}(4.2)$, and one can expect that the strength of the quantized structure depends on the value of $\sqrt{G_{xx}(4.2)G_{yy}(4.2)}$. The suppression of the quantization phenomenon could be explained by the increase of G_{yy}. For a three-dimensional system the angular dependence of the conductivity σ_{yy} can be written as

$$\sigma_{yy}(\alpha)=\sigma_{yy}(0°)\cos^2\alpha+\sigma_{zz}(0°)\sin^2\alpha. \tag{2}$$

The other important (to us) components of the conductivity and resistivity tensor in the tilted field are equal to

$$\sigma_{xx}(\alpha)=\sigma_{xx}(0°),\quad \rho_{xx}(\alpha)=\rho_{xx}(0°),$$
$$\sigma_{xy}(\alpha)=\sigma_{xy}(0°)\cos\alpha,\quad \rho_{xy}(\alpha)=\rho_{xy}(0°)\cos\alpha. \tag{3}$$

$\sigma_{yy}(\alpha)=G_{yy}(\alpha)/d$ is larger than $\sigma_{yy}(0°)$ because of the larger value of $\sigma_{zz}(0°)$ along the magnetic field. We can get an estimate for this from measurements of the longitudinal magnetoresistance of a single crystal with practically the same electron density and mobility as for our layer.[5] At 4.2 K and in a field of 12 T, the value of $\sigma_{zz}(0°)\approx 55$ S/cm while $\sigma_{xx}(0°)=\sigma_{yy}(0°)=9$ S/cm only. For our sample this would lead to an increase in $G_{yy}=\sigma_{yy}d$ upon rotating the sample. The resulting increase of $(G_{xx}G_{yy})^{1/2}$, i.e., the increase of the diffusion in the plane of the layer, could therefore cause the suppression of the quantized Hall effect structures.

We note that Eq.(2) probably gives a not very precise description of the anisotropic transport in our samples because the scattering length l and the magnetic length l_H

($\approx$7 nm at $B=14$ T) are not much less than the layer thickness d. This would lead to an influence of the surface boundaries on the conductance tensor $\hat{G}$. In a tilted magnetic field, the motion of an electron at the top and surface boundaries is absolutely different from the motion inside the layer. The orbits become skipping (classically speaking) at a distance of the order of l_H from the surfaces, leading to a nonuniform current distribution along the thickness of the layer. Therefore, the $\hat{G}$ and, correspondingly, $\hat{R}$ tensor can be rather different from those obtained by the conventional transformation in a tilted field. Indications for this can be seen in the differences at 4.2 K between $R_{xx}(0°)$ and $R_{xx}(\alpha)$ (see Fig. 1) and also between $R_{xy}(\alpha)$ and $R_{xy}(0°)\cos\alpha$, which are rather pronounced at $\alpha=60°$. However, the anisotropic magnetoconductivity would still give $G_{yy}(\alpha) > G_{yy}(0°)$.

We have no explanation for the observed shift of the minima with rotation of the field, but our measurements show that the behavior of our disordered GaAs layer system is definitely different from the behavior of 2D systems.

In summary, the minima in R_{xx} and dR_{xy}/dB in the quantized Hall effect of a disordered heavily doped GaAs layer with a 3D single-particle spectrum have a much weaker shift to higher magnetic fields in a tilted magnetic field than the $1/\cos\alpha$ dependence for the quantum Hall effect measurements in the 2D case. The suppression of the quantized phenomenon in a rotated magnetic field could be related to the mixing of the conductivity tensor component $\sigma_{zz}(0°)$ into the component $\sigma_{yy}(\alpha)$, which would reduce electron–electron interaction effects in the diffusive transport of a disordered system.

This work is supported by the Russian Fund for Fundamental Research (Grant 98-02-16633).

[1] R. E. Prange and S. M. Girven (Eds.), *The Quantum Hall Effect*, Springer-Verlag, 1990.
[2] S. S. Murzin, A. G. M. Jansen, and P. v. d. Linden, Phys. Rev. Lett. **80**, 2681 (1998).
[3] S. S. Murzin, JETP Lett. **67**, 216 (1998).
[4] B. L. Al'tshuler and A. G. Aronov, Zh. Éksp. Teor. Fiz. **77**, 2028 (1979) [Sov. Phys. JETP **50**, 968 (1979)].
[5] Kh. I. Amirkhanov, P. I. Bashirov, and A. Yu. Mollaev, Fiz. Tekhn. Poluprovodn. **4**, 1884 (1970) [Sov. Phys. Semicond. **4**, 1616 (1970)].

Published in English in the original Russian journal. Edited by Steve Torstveit.

Anisotropy of the superconducting properties of $YBa_2Cu_3O_{7-x}$ single crystals with reduced oxygen content

V. N. Zverev,[a] D. V. Shovkun, and I. G. Naumenko
Institute of Solid-State Physics, Russian Academy of Sciences, 142432 Chernogolovka, Moscow Region, Russia

(Submitted 8 July 1998; resubmitted 14 July 1998)
Pis'ma Zh. Éksp. Teor. Fiz. **68**, No. 4, 309–313 (25 August 1998)

In an investigation of the resistivity anisotropy of $YBa_2Cu_3O_{7-x}$ single crystals with suboptimal oxygen content it is observed that the superconducting transition for the component ρ_c of the resistivity tensor is shifted to lower temperatures with respect to the transition for the component ρ_{ab}. A similar shift is also observed for the transition in the temperature dependence of the dynamic magnetic susceptibility. [S0021-3640(98)01216-X]

PACS numbers: 74.72.Bk, 74.25.Fy, 74.62.Bf

Cuprate high-T_c superconductors are highly anisotropic layered compounds characterized by the presence of CuO_2 planes, which are believed to be responsible for the superconductivity.

In Ref. 1, in a study of the temperature dependences of the resistance and magnetic susceptibility of $Bi_2Sr_{3-x}Ca_xCu_2O_{8+y}$ single crystals, it was observed that the superconducting transition temperature was approximately 40 K higher in the case of current flow along the CuO_2 layers ($\mathbf{j} \perp \mathbf{c}$, where $\mathbf{c}$ is the direction of the crystallographic axis perpendicular to the layers) than in the case of current flow perpendicular to the layers ($\mathbf{j} \parallel \mathbf{c}$).

Friedel predicted theoretically a similar behavior of layered superconductors.[2] He proposed a specific mechanism of ''growth'' of ring-shaped Josephson vortices in a certain temperature range $T_f < T < T_c$ below T_c that should suppress superconductivity in this range in the direction perpendicular to the CuO_2 layers. According to Friedel's conjecture, such a temperature interval should exist in any layered superconductor that is described by a model of a stack of superconducting planes between which Josephson links exist. The temperature T_f above which these links are broken is the Friedel transition temperature.

Later, Korshunov and Rodriguez[3] pointed out an error in Friedel's calculations and showed that such a mechanism is not realized in an ideal crystal. However, it was recently shown theoretically in Ref. 4 that a Friedel transition can occur if the layers are not assumed to be ideal and it is assumed that there is a random distribution over superconducting properties of the layers. Specifically, it was assumed that two types of layers with different parameters $J_\parallel$, characterizing the coupling constant inside a layer in

an anisotropic 3D XY model, exist in the crystal. The Friedel transition was obtained only when the distribution of such layers in a crystal was not periodic but random.

The reason for the observed[1] shift of the superconducting transition was not established. In principle, any macroscopic nonuniformity of the sample can lead to a shift of the transition, but the observed phenomenon could have been due to a Friedel transition. In any case, such behavior is a consequence of the layered structure of the single crystals investigated. In this connection, it is of interest to observe the shift of the transition in other layered superconductors.

In the present work, we chose $YBa_2Cu_3O_{7-x}$ single crystals (YBCO) for the investigations. Initially, at optimal doping $x \approx 0.05$ this superconductor possesses a much weaker anisotropy than bismuth or thallium cuprate superconductors, but as the oxygen content decreases, the degree of anisotropy increases rapidly. The behavior of YBCO as a function of oxygen content is reversible and has been rather well studied. For this reason we undertook to observe the shift of the superconducting transition with decreasing oxygen content in high-quality (in the initial state) single crystals for different orientations of the current relative to the CuO_2 layers.

In the experiment, the anisotropy of the electrical resistance and the dynamic magnetic susceptibility was measured on YBCO single crystals in the form of slabs with dimensions of approximately $2 \times 1 \times 0.05$ mm, for which the crystallographic direction **c** was normal to the plane of the slabs.

The $YBa_2Cu_3O_{7-x}$ single crystals were grown in a ZrO_2 crucible by the method described in Ref. 5. The total impurity content in the samples, which was less than 0.005%, was determined by the inductively-coupled plasma method, which consisted of a mass-spectrometric analysis of an argon plasma containing the vaporized sample and ignited by an rf inductor.

After annealing at 500 °C in oxygen, the samples possessed a narrow superconducting transition with $T_c \approx 92$ K and transition width less than 0.5 K. The required reduced oxygen content was achieved by choosing the annealing temperature (up to 820 °C) in air at atmospheric pressure and subsequent quenching in liquid nitrogen in accordance with the data of Refs. 6–8. The samples were annealed in a quartz ampoule and covered with YBCO powder in order to preserve the high quality of the surface. No special measures were taken to detwin the samples.

To measure the real part of the dynamic magnetic susceptibility χ, the sample was placed inside a pair of coaxial coils 6 mm in diameter, one of which served to excite an ac magnetic field, while the other was for measuring. An identical pair of coils, which was used to compensate the signal in the absence of the sample, was placed next to it. Using the standard synchronous detection scheme, we measured the component of the imbalance signal proportional to the real part of the induced magnetic moment M of the sample in an ac magnetic field of frequency 10^5 Hz: $M = \chi h V$. Here h is the amplitude of the magnetic field in the coil and V is the volume of the sample. The amplitude h of the field was chosen to be small, so that the signal was linear in h, and equal to 0.1 Oe. The sample in the coil was placed either perpendicular ($\mathbf{c} \| \mathbf{h}$) or parallel to ($\mathbf{c} \perp \mathbf{h}$) to the magnetic field. For this, the sample was glued to different faces of a sapphire rod, shaped in the form of a rectangular parallelepiped. We denote by χ_{ab} the susceptibility component measured in the first case, since ring currents flow only in the plane of the CuO_2

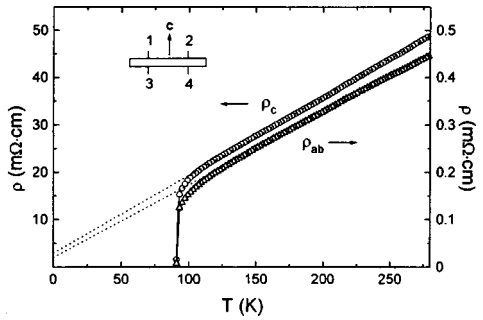

FIG. 1. Temperature dependence of the resistivity components ρ_{ab} and ρ_c of the initial YBCO single crystal. Dotted lines — extrapolations of the linear parts of the temperature dependences of the resistivity to zero temperature. Inset: Geometry of the contacts.

layers, and we denote by χ_c the susceptibility component in the second case, since in this case a portion of the path which the currents must follow to closure is perpendicular to the layers.

The sample together with a thermometer and a heater arranged alongside were placed inside a glass Dewar, which was immersed, upside down, in liquid helium. The measuring coils were wound on the outer surface of the Dewar and were always at liquid helium temperature during the measurements. To prevent a temperature gradient, the sample was placed in a sapphire container.

A four-contact method was used to investigate the electrical resistance of anisotropic single crystals.[9] In this method, two pairs of contacts were placed opposite one another on opposite sides of the sample (see inset in Fig. 1). The contacts were prepared by depositing drops of silver paste on the surface of the sample. The drops were then ''burned in'' by heating the sample in air at 400 °C. The subsequent manipulations of the sample (annealing, remounting) did not change the properties of the contacts. The characteristic size of the contacts did not exceed 0.3 mm, and the accuracy of the placement of the contacts opposite one another on the opposite sides of the sample was not worse than 0.05 mm.

The components of the resistivity tensor ρ_{ab} in the plane of the layers and ρ_c normal to the layers could be calculated numerically, using the formulas of Ref. 9, from the results of two measurements $R_{ab}=V_{12}/J_{34}$ and $R_c=V_{13}/J_{24}$, assuming an infinite sample. This condition limited the applicability of this method to a large anisotropy $\eta=\rho_c/\rho_{ab}$. In our experiments, the calculations of ρ_{ab} and ρ_z were performed only for the initial sample with optimal oxygen content, for which η was of the order of 10^2. For samples with reduced oxygen content, where the anisotropy was much higher, we present only the values of R_{ab} and R_c.

In the present work we investigated two samples in detail. Their behavior was similar overall but different in detail. For the sample whose data are reported in the present letter the resistivities in the state with optimal oxygen concentration were $\rho_{ab}=460\ \mu\Omega\cdot$ cm and $\rho_c=48\ \text{m}\Omega\cdot$ cm at $T=300$ K, and the values decreased linearly with decreasing temperature (but not too close to $T_c\simeq 92$ K; Fig. 1).

Next, the sample was annealed at a fixed temperature, resulting in a lower oxygen

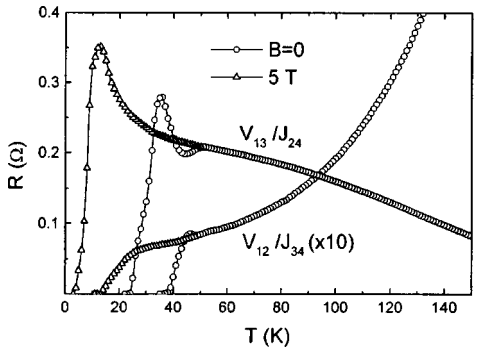

FIG. 2. Temperature dependences $R_{ab}(T)$ ($\mathbf{j}\perp\mathbf{c}$) and $R_c(T)$ ($\mathbf{j}\parallel\mathbf{c}$) in the absence of a magnetic field (○) and in a 5 T field (△).

concentration, after which the temperature dependences of the resistances R_{ab} and R_c and the susceptibilities χ_{ab} and χ_c were measured. Then the procedure was repeated at a higher annealing temperature, all the way up to the temperature ~820 °C at which the sample was no longer a superconductor.[8]

Figure 2 shows the temperature dependences $R_{ab}(T)$ and $R_c(T)$ for a sample annealed at 790 °C for 35 h. As one can see from the figure, the resistances $R_{ab}(T)$ and $R_c(T)$ do not vanish simultaneously as temperature decreases: first R_{ab} vanishes at $T_1 \simeq 40$ K; in the process, $R_c(T)$ increases, reaches a maximum approximately at the point where $R_{ab}(T)$ vanishes, and then decreases and vanishes at $T_2 \simeq 30$ K, i.e., at an approximately 10 K lower temperature. This nonsimultaneous vanishing of R_{ab} and R_c started only when T_c of the sample dropped below ≈60 °C, and it was observed for both experimental samples, though the temperature interval ΔT where $R_{ab}=0$ while $R_c>0$ was different.

The same effect was also observed in the temperature dependences of the dynamic magnetic susceptibility, which were measured for two different orientations of the ac magnetic field h — parallel (χ_{ab}) and perpendicular (χ_c) to the **c** axis (Fig. 3). We note

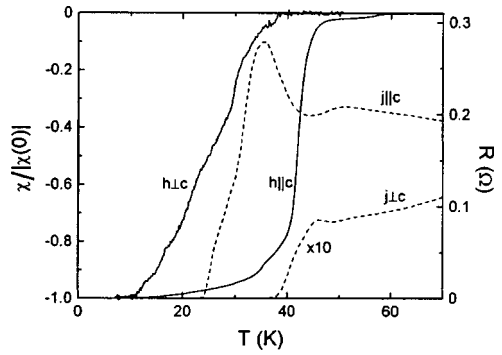

FIG. 3. Comparison of the temperature dependence of the normalized dynamic susceptibility (solid curves) and the resistance (dashed curves) near a superconducting transition.

that Fig. 3 shows the temperature dependences normalized to the susceptibility at zero temperature. In the experiment the ratio $\chi_{ab}(0)/\chi_c(0)=29$, which reflects the anisotropy of the demagnetizing factor of the sample.

As one can see from Fig. 2, applying a magnetic field $\mathbf{B}\|\mathbf{c}$ decreases the values of the characteristic temperatures at which each of the measured quantities $R_{ab}(T)$ and $R_c(T)$ vanishes, but the difference between them remains approximately the same as for $B=0$.

The experimentally observed shift of the superconducting transition means that there exists a temperature interval below T_c where the superconducting current exists only in the plane of the CuO_2 layers and equals zero in the perpendicular direction. As we have said, such behavior could be a manifestation of a Friedel transition but it could also be due to the nonuniformity of the sample. There are two types of nonuniformities which can lead to the effect that we observe:

1) the presence of layers with a higher value of T_c which are separated by layers with a lower value of T_c;

2) the presence of planar defects, playing the role of weak links between layers, where a supercurrent arises (on account of thermal fluctuations) at temperatures less than T_c of the layers (a similar mechanism is realized in granular superconductors[10]).

The effect which we observed cannot be due to defects of the second type. This follows from the experiment in a magnetic field. Actually an external magnetic field should destroy the weak links and therefore shift the transition in $R_c(T)$ more strongly than in $R_{ab}(T)$.

An additional argument supporting the fact that the observed defect is not due to defects of the second type follows from the behavior of the dynamic magnetic susceptibility. The point is that in the geometry $\mathbf{h}\perp\mathbf{c}$, i.e., when the field is parallel to the layers, planar nonsuperconducting defects make virtually no contribution to the susceptibility (provided that their total volume is small compared with that of the sample). For this reason, even though the presence of defects can lead to the phenomenon that we observed in the resistance, it cannot explain the behavior of the susceptibility. For this reason, the nonuniformities of the first type can lead to the observed phenomenon only in the case that the fraction of the higher-temperature layers is small compared with that of the low-temperature layers. In the limiting case, one narrow high-T_c layer can exist in the sample. Although we cannot rule out this variant, it seems unlikely. It would be more natural to infer that the distribution of T_c over the layers is smooth. However, in this case the superconducting transitions should start at the same temperature for different orientations of the current, in contradiction to experiment.

The magnitude of the temperature shift ΔT observed in the experiment depended on the stage of annealing of the sample, and for different samples differed appreciably for approximately equal values of T_c. This shows that the nonuniformity of the sample is still considerable. But, at the present stage of the investigations, it could not be determined unequivocally whether we are dealing with a Friedel transition (with allowance for the fact that the CuO_2 layers are not all identical) or whether the phenomenon is due to a macroscopic nonuniformity of the sample.

In summary, in the present work a shift of the superconducting transition to low

temperatures was observed in oxygen-deficient YBCO single crystals in the case of current flow perpendicular to the CuO_2 layers. This phenomenon could be due to a Friedel transition in a nonuniform layered superconductor.

The authors are grateful to V. F. Gantmakher for his interest in this work and for critical remarks and to V. I. Karandashev for assisting in the elemental analysis of the samples. This work was performed as part of Project 98-02-16636 of the Russian Fund for Fundamental Research and Projects 96-012 and 96-060 of the State Program ''Superconductivity.''

[a)]e-mail: zverev@issp.ac.ru

---

[1] V. L. Arbuzov, O. M. Bakunin, A. É. Davletshin *et al.*, JETP Lett. **48**, 440 (1988).
[2] J. Friedel, J. Phys. (France) **49**, 1561 (1988).
[3] S. T. Korshunov, Europhys. Lett. **11**, 757 (1990); J. P. Rodriguez, Europhys. Lett. **31**, 479 (1995).
[4] M. Dzierzawa, M. Zamora, D. Baeriswyl, and X. Bagnoud, Phys. Rev. Lett. **77**, 3897 (1996).
[5] M. R. Trunin, A. A. Zhukov, G. A. Emel'chenko, and I. G. Naumenko, JETP Lett. **65**, 938 (1997).
[6] A. N. Lavrov and L. P. Kozeeva, Physica C **253**, 313 (1995).
[7] A. N. Lavrov and L. P. Kozeeva, Physica C **248**, 365 (1995).
[8] V. F. Gantmakher, L. P. Kozeeva, A. N. Lavrov *et al.*, JETP Lett. **65**, 870 (1997).
[9] P. Schnabel, Z. Angew. Phys. **22**, 136 (1967).
[10] O. Entin-Wohlman, A. Kapitulnik, and Y. Shapira, Phys. Rev. B **24**, 6464 (1981).

Translated by M. E. Alferieff

Quantum corrections to the conductivity in systems with strong spin–orbit splitting of the spectrum

I. V. Gornyĭ,[a)] A. P. Dmitriev, and V. Yu. Kachorovskiĭ
A. F. Ioffe Physicotechnical Institute, Russian Academy of Sciences, 194021 St. Petersburg, Russia

(Submitted 15 July 1998)
Pis'ma Zh. Éksp. Teor. Fiz. **68**, No. 4, 314–319 (25 August 1998)

Quantum corrections to the conductivity in a 2D system with a smooth random potential and strong spin–orbit splitting of the spectrum are studied. It is shown that the interference correction is positive and, right down to very low temperatures, does not exceed in magnitude the negative correction due to the electron–electron interaction. © *1998 American Institute of Physics.* [S0021-3640(98)01316-4]

PACS numbers: 73.50.Bk, 71.30.+h, 71.70.Ej

Recent experiments on high-mobility Si-MOS structures[1] have demonstrated the possibility of a metal–insulator transition in two-dimensional (2D) systems. It was found that for electron density n greater than a certain critical value n_c the system passes into a metallic phase. This contradicts the generally held view whereby the electronic states in a disordered 2D system must be localized.[2]

A characteristic feature of Si-MOS structures is strong spin–orbit splitting of the electronic spectrum by the built-in electric field of an asymmetric quantum well.[3] This circumstance has stimulated interest in the study of quantum corrections of the conductivity with an arbitrary ratio of the splitting Δ and the elastic collision time τ.[4] Calculations have been performed under the assumption that the impurity scattering potential is short-range. It has been shown that the interference correction even with quite small splitting changes sign and becomes antilocalizing. In the actual situation for the experiment of Ref. 1, $\Delta\tau \gg \hbar$, it is due to interference of two electronic waves with zero total spin and has the form

$$\delta\sigma_{wl} = \frac{e^2}{4\pi^2\hbar} \ln\frac{\tau_\phi}{\tau}. \tag{1}$$

Here τ_ϕ is the phase interruption time, which at low temperatures is governed solely by electron–electron collisions and is inversely proportional to the temperature T (Ref. 5). The result (1) is similar to the well-known result of Ref. 6 for the case of strong spin–orbit scattering by a random potential.

Generally speaking, a change in sign of the quantum correction to the conductivity indicates the possibility of a metal–insulator transition.[2,7] However, as a number of authors have noted,[7–9] the inclusion of the spin–orbit interaction cannot shed light on the

nature of the metallic state observed in Ref. 1. Indeed, besides the positive interference correction (1), there is also a negative quantum correction, due to the electron–electron interaction, to the conductivity:[5]

$$\delta\sigma_{ee} = -\frac{e^2}{2\pi^2\hbar}\ln\frac{\hbar}{T\tau}. \tag{2}$$

This expression does not contain a Hartree contribution, since this contribution derives from the interaction of a particle and a hole with nonzero total spin and is therefore suppressed in the presence of a strong spin–orbit interaction.[10] Even at not very low temperature $\delta\sigma_{ee}$ exceeds the quantity in (1), as a result of which the total correction to the conductivity is negative and grows in magnitude as T decreases, which corresponds to dielectric behavior.

In the presence of valley degeneracy, Eq. (1) holds for $\tau_\phi \gg \tau_v$, where τ_v is the characteristic intervalley scattering time. In the opposite limiting case, $\tau_\phi \ll \tau_v$, the interference corrections to the conductivity from each valley add, and expression (1) is multiplied by the number of valleys N_v. At the same time, the expression for $\delta\sigma_{ee}$ does not contain N_v (Refs. 5 and 11), and the temperature dependence of the total correction has the form

$$\delta\sigma_{\text{tot}} = \frac{e^2}{2\pi^2\hbar}\left(\frac{N_v}{2} - 1\right)\ln\frac{\hbar}{T\tau}. \tag{3}$$

Hence it follows that the presence of several valleys decreases the relative role of localization effects and can lead to antilocalization in the temperature range where $\tau_\phi \ll \tau_v$. However, all the same, for $N_v = 2$ (which corresponds to the experimental situation of Ref. 1) valley degeneracy does not lead to metallic behavior. Indeed, one can see from Eq. (3) that the total correction to the conductivity in this case does not depend on temperature. This result is correct if intervalley transitions are completely neglected, i.e., to zero order in τ_ϕ/τ_v. However, it can be shown that even in first order in this parameter the conductivity decreases slowly as the temperature decreases, i.e., the taking into account of arbitrarily weak intervalley transitions leads to dielectric behavior.

In the present letter we investigate the effect of strong spin–orbit splitting of the spectrum ($\Delta\tau \gg \hbar$) on quantum corrections to the conductivity of electrons moving in a *smooth* random potential. We do not claim to explain the metal–insulator transition observed in Ref. 1, but rather we study only the quantum corrections to the conductivity in the region of high conductances, i.e., far from the metal–insulator transition ($n \gg n_c$).

The results obtained differ considerably from the results for the case of a *short-range* impurity potential: For sufficiently strong splitting the interference correction to the conductivity is positive, and all the way down to very low temperatures it is two times greater in magnitude than the value given by Eq. (1). As a result, the total correction (with the valley degeneracy taken into account) is *antilocalizing*, and the behavior of the system is of a metallic character. This result is due to the fact that in the case of scattering by a smooth potential, in contrast to the case of a pointlike potential, transitions between spin subbands are strongly suppressed, and each valley decomposes into two independent subsystems. For this reason, in the case of two valleys, N_v in expression (3) effectively

equals 4 instead of 2. We note that in the experiments of Ref. 1 the random potential was produced mainly by distant ionized impurities, and for this reason it was a long-range potential.

We shall confine our attention to the high-density region, where the kinetic energy E_F of the electrons is higher than their Coulomb interaction energy. We consider the case of a single valley first. We write the term in the Hamiltonian that is responsible for spin–orbit splitting in the form $\alpha([\hat{\sigma}\times\mathbf{k}]\cdot\mathbf{n})$. Here α is a constant characterizing the spin–orbit interaction force, $\hat{\sigma}$ is a vector consisting of the Pauli matrices, $\hbar\mathbf{k}$ is the momentum measured from the valley bottom, and $\mathbf{n}$ is the normal to the plane of the well. The energy spectrum and wave functions of an electron with effective mass m have the form

$$E^{\pm}(\mathbf{k})=\frac{\hbar^2k^2}{2m}\pm\alpha k:,\quad \phi_{\mathbf{k}}^{\pm}(\mathbf{r})=\exp(i\mathbf{kr})\chi_{\mathbf{k}}^{\pm},\quad \chi_{\mathbf{k}}^{\pm}=\frac{1}{\sqrt{2}}\begin{pmatrix}1\\ \pm ie^{i\varphi_{\mathbf{k}}}\end{pmatrix}. \tag{4}$$

The spinors $\chi_{\mathbf{k}}^{\pm}$ depend on the angle $\varphi_{\mathbf{k}}$ of the wave vector $\mathbf{k}$ and describe two states with spins polarized parallel to the vectors $\pm[\mathbf{k}\times\mathbf{n}]$, respectively. Therefore the system decomposes into two subsystems (branches), $+$ and $-$, in each of which the electron spin is rigidly coupled with the momentum.

We shall assume that the random smooth impurity potential $U(\mathbf{r})$ with correlation function $K(\mathbf{r})=\langle U(\mathbf{r})U(0)\rangle$, decaying on a scale $d\gg k_F^{-1}$, is sufficiently weak so that $E_F\tau\gg\hbar$ and $\tau\gg d/v_F$. The presence of this potential leads both to intrabranch and interbranch transitions. The corresponding times are given by the expression

$$\frac{1}{\tau_{\mu\nu}}=\frac{2\pi}{\hbar}\int\frac{d^2\mathbf{q}}{(2\pi)^2}K_{\mu\nu}(\mathbf{q})\,\delta[E^{\mu}(\mathbf{k})-E^{\nu}(\mathbf{k}-\mathbf{q})], \tag{5}$$

where $K_{\mu\nu}(\mathbf{q})=|\langle\chi_{\mathbf{k}}^{\mu}|\chi_{\mathbf{k}-\mathbf{q}}^{\nu}\rangle|^2K(q)$, the indices μ and ν assume the values $+$ and $-$, and $K(q)$ is a Fourier component of the correlation function of the potential and decays with a characteristic scale d^{-1}. We assume below that the spin–orbit splitting $\Delta=2\alpha k_F$ is small compared with E_F and we set $\tau_{++}=\tau_{--}=\tau$, while $\tau_{+-}=\tau_{-+}=\tau_*$. For interbranch transitions the minimum momentum transfer is dictated by the δ function in Eq. (5) and equals $2m\alpha/\hbar$. If, besides the inequality $\Delta\tau\gg\hbar$, the more stringent condition

$$m\alpha d\gg\hbar^2 \tag{6}$$

holds, then interbranch transitions are strongly suppressed compared with intrabranch transitions. Specifically, for the potential produced by ionized impurities located a distance d from the 2D layer, the correlation function $K(q)\sim\exp(-2qd)$, and we have for the interband-transition time

$$\tau_*=4(k_Fd)^2\exp(4m\alpha d/\hbar^2)\,\tau. \tag{7}$$

The factor $(k_Fd)^2$ in this expression is due to the orthogonality of the spinors corresponding to different branches and to identically directed momenta. We note that in the case of scattering by a short-range potential any momentum transfer ($K(q)=$ const) and τ_* of the same order of magnitude as the intrabranch scattering time are possible.

On time scales less than τ_* interbranch transitions are absent, and we can assume that we have two independent subsystems corresponding to these branches. For this reason, for $\tau_\phi \ll \tau_*$ the interference correction to the conductivity is a sum of corrections from the two branches. In each branch the correction equals $\delta\sigma_{wl}^+ = \delta\sigma_{wl}^- = (1/2) \times (e^2/2\pi^2\hbar)\ln(\tau_\phi/\tau_{tr})$, where $\tau_{tr} \sim (k_F d)^2 \tau$ is the transport time. The calculation is performed just as in the absence of spin splitting,[12] but the result is two times smaller in magnitude and positive. The factor 1/2 arises because summation over the two spin states is not performed when the contribution from one branch is calculated. The difference in sign is due to the fact that under a rotation by an angle of 2π the spin wave function is multiplied by -1. Indeed, the correct $\delta\sigma_{wl}$ is related with the effective change in the backscattering amplitude as a result of interference of two waves traversing closed paths in opposite directions. In our case the spin, always perpendicular to the momentum, rotates adiabatically by an angle of π on one of the interfering paths and by an angle of $-\pi$ on the oppositely directed path. The relative rotation of the spins of the two waves equals 2π, which is why the correction changes sign (Ref. 13).[b)] The total inference correction from the two branches equals

$$\delta\sigma_{wl} = \delta\sigma_{wl}^+ + \delta\sigma_{wl}^- = \frac{e^2}{2\pi^2\hbar}\ln\frac{\tau_\phi}{\tau_{tr}}. \tag{8}$$

For an arbitrary ratio of τ_ϕ and τ_* the calculation can be performed by using the method proposed in Ref. 6 and elaborated in Ref. 14 for solving the equation for a cooperon in multiband systems. The corresponding calculations will be presented in a more detailed publication. The result is

$$\delta\sigma_{wl} = \frac{e^2}{4\pi^2\hbar}\left[\ln\frac{\tau_\phi}{\tau_{tr}} + \ln\frac{\tau_\phi\tau_*}{(2\tau_\phi + \tau_*)\tau_{tr}}\right]. \tag{9}$$

For $\tau_\phi \ll \tau_*$ this expression goes over to Eq. (8). In the limit $\tau_\phi \gg \tau_*$, when a large number of interbranch transitions occur during the phase interruption time, the first terms makes the main contribution in Eq. (8). This contribution is similar to expression (1) for the case of a short-range potential.

The following illustrative considerations should elucidate Eq. (9). Since the spin–orbit splitting is assumed to be large, the waves propagating in opposite directions along a closed path on any section between two successive scatterings should belong the same branch (although on scattering the type of branch can change simultaneously in both waves). In addition, only processes such that each wave at the beginning and end of the path also belongs to the same branch are important. In the opposite case, the waves acquire substantially different phases and do not interfere. In such a situation the correction is proportional to the number of times a particle returns to the initial point and to the initial branch. We shall estimate this number in the diffusion approximation. The corresponding equations are

$$\frac{\partial c}{\partial t} - D\Delta c = \delta(\mathbf{r})\,\delta(t) + \frac{c' - c}{\tau_*} - \frac{c}{\tau_\phi}, \quad \frac{\partial c'}{\partial t} - D\Delta c' = \frac{c - c'}{\tau_*} - \frac{c'}{\tau_\phi}. \tag{10}$$

Here $c(\mathbf{r},t)$ and $c'(\mathbf{r},t)$ are the probability densities of observing a particle at time t at the point $\mathbf{r}$ on the initial and second branches, respectively, and $D=v_F^2\tau_{tr}/2$ is the diffusion coefficient [Note: The symbol Δ here denotes the Laplacian operator]. The Fourier component $c_{q,\omega}$ is the sum of two pole contributions

$$c_{q,\omega}=\frac{1}{2}\left(\frac{1}{Dq^2-i\omega+\tau_\phi^{-1}}+\frac{1}{Dq^2-i\omega+\tau_\phi^{-1}+2\tau_*^{-1}}\right).$$

The number of returns to the initial branch that are of interest to us is proportional to the integral $\int_{\tau_{tr}}^{\infty}c(\mathbf{r}=0,t)dt$, upon calculation of which we obtain the sum of the two logarithms appearing in Eq. (9).

We shall now discuss the role of the electron–electron interaction in our problem. This interaction leads to a quantum correction to the conductivity and determines the phase interruption time. Moreover, electron–electron collisions can give rise to transitions between the branches of the spectrum. It can be shown that the correction to the conductivity $\delta\sigma_{ee}$ for any ratio of T and τ_* is once again given by expression (2). This is due to the fact that it is determined by the total (summed over branches) probability of a diffusing particle reaching the final point from the initial point. This probability does not depend on τ_*, as can be easily verified using Eqs. (10), in which the substitution $\tau_\phi=\infty$ must be made. Indeed, τ_* drops out of the equation for the sum of c and c'. The phase-interruption time is insensitive to the spin–orbit splitting of the spectrum, and the formula proposed in Ref. 5 can be used:

$$\frac{1}{\tau_\phi}\sim\frac{T}{E_F\tau_{tr}}\ln\frac{E_F\tau_{tr}}{\hbar}.$$

Interbranch transitions due to electron–electron collisions can be neglected, since the characteristic time τ_*^{ee} of these transitions at low temperatures is long compared with the times τ_ϕ and τ_*. This explained by the fact that the minimum momentum transfer in a transition to another branch under the condition $\Delta\tau\gg\hbar$ is much larger than the reciprocal of the mean free path, and the ballistic approximation must be used to calculate τ_*^{ee}. As a result, τ_*^{ee} is inversely proportional to the square of the temperature.[5]

We shall now take the valley degeneracy into account, assuming that $\tau_v\gg\tau_*$. Then the total quantum correction to the conductivity is the sum of expression (2) (with τ replaced by τ_{tr}) plus expression (9) multiplied by N_v. At temperatures

$$T>T_*\sim\frac{E_F}{\ln(E_F\tau_{tr}/\hbar)}\,\frac{\tau_{tr}}{\tau_*} \tag{11}$$

the phase-interruption time is shorter than the interbranch transition time ($\tau_\phi<\tau_*$). In this temperature range we obtain for the T-dependent part of the total correction

$$\delta\sigma_{\text{tot}}=\frac{e^2}{2\pi^2\hbar}(N_v-1)\ln\frac{\hbar}{T\tau_{tr}} \tag{12}$$

Hence one can see that for $N_v=2$ the conductivity grows logarithmically as the temperature decreases, i.e., metallic behavior is observed.

As can easily be verified, in the interval $\tau_v > \tau_\phi > \tau_*$ the conductivity continues to increase slowly, reaches a maximum at $\tau_\phi \sim \tau_v$, and then decreases logarithmically only if $\tau_\phi > \tau_v$.

We now present some estimates. In the experimental situation, according to Ref. 15, $\alpha \approx 5 \times 10^{-6}$ K·cm, $m = 0.2 m_e$, and $d \sim 10^{-5}$ cm. Under these conditions the argument of the exponential in Eq. (7) is large, so that $\tau_* \gg \tau_{tr}$. Then for $n = (5-10) \times 10^{11}$ cm^{-2} we obtain for T_* a value of the order of several mK, which is less than the lowest temperatures (20 mK) used in the experiments of Ref. 1. Thus the mechanism proposed above could possibly explain the metallic behavior at low temperatures in the region $n \gg n_c$.

We thank V. M. Pudalov, M. I. D'yakonov, N. S. Averkiev, and L. E. Golub for helpful discussions. This work was supported by the Russian Fund for Fundamental Research (Grants 96-02-17896 and 96-02-17894), the Royal Swedish Academy of Sciences (Grant 1240), and INTAS (Grant 96-196). We also are grateful to the Program for Support of Leading Science Schools and the Program ''Physics of Solid-State Nanostructures'' (Grant 1001).

[a)]e-mail: gorny@vip1.ioffe.rssi.ru

[b)]In Ref. 13, the importance of processes which are not associated with backscattering was underscored. It can be shown that the contribution of such processes likewise changes sign.

[1] S. V. Kravchenko, G. V. Kravchenko, J. E. Furneaux *et al.*, Phys. Rev. B **50**, 8039 (1994); S. V. Kravchenko, W. E. Mason, G. E. Bowker *et al.*, Phys. Rev. B **51**, 7038 (1995).
[2] E. Abrahams, P. W. Anderson, D. C. Licciardello, and T. V. Ramakrishnan, Phys. Rev. Lett. **42**, 673 (1979).
[3] V. M. Pudalov, http://xxx.lanl.gov/abs/cond-mat/9707076; JETP Lett. **66**, 175 (1997).
[4] M. A. Skvortsov, http://xxx.lanl.gov/abs/cond-mat/9712135; Y. Lyanda-Geller, http://xxx.lanl.gov/abs/cond-mat/9801095.
[5] B. L. Altshuler and A. G. Aronov, in *Electron–Electron Interactions in Disordered Systems*, edited by A. L. Efros and M. Pollak (Vol. 10 of Modern Problems in Condensed Matter Sciences Series), North-Holland, Amsterdam–New York, 1985.
[6] S. Hikami, A. I. Larkin, and Y. Nagaoka, Prog. Theor. Phys. **63**, 707 (1980).
[7] V. Dobrosavljevic, E. Abrahams, E. Miranda, and S. Chakravarty, Phys. Rev. Lett. **79**, 455 (1997).
[8] D. Belitz and T. R. Kirkpatrick, http://xxx.lanl.gov/abs/cond-mat/9705023.
[9] C. Castellani, C. DiCastro, and P. A. Lee, http://xxx.lanl.gov/abs/cond-mat/9801006.
[10] B. L. Altshuler and A. G. Aronov, Solid State Commun. **46**, 429 (1983).
[11] H. Fukuyama, in *Electron–Electron Interactions in Disordered Systems*, edited by A. L. Efros and M. Pollak (Vol. 10 of Modern Problems in Condensed Matter Sciences Series), North-Holland, Amsterdam–New York, 1985.
[12] D. Rainer and G. Bergmann, Phys. Rev. B **32**, 3522 (1985).
[13] A. P. Dmitriev, I. V. Gornyi, and V. Yu. Kachorovskii, Phys. Rev. B **56**, 9910 (1997).
[14] G. E. Pikus, N. S. Averkiev, and L. E. Golub, in press.
[15] V. M. Pudalov, G. Brunthaler, A. Prinz, and G. Bauer, http://xxx.lanl.gov/abs/cond-mat/9801077; V. M. Pudalov, private communication.

Translated by M. E. Alferieff

Photoinduced transformations in C_{60} films irradiated by femtosecond laser pulses

V. O. Kompanets and S. V. Chekalin[a)]
Institute of Spectroscopy, Russian Academy of Sciences, 142092 Troitsk, Russia

N. N. Mel'nik
P. N. Lebedev Physics Institute, Russian Academy of Sciences, 117924 Moscow, Russia

B. C. Hess
Brigham Young University, Provo, UT 84602 USA

(Submitted 15 July 1998)
Pis'ma Zh. Éksp. Teor. Fiz. **68**, No. 4, 320–325 (25 August 1998)

Photoinduced polymerization and photoinduced diffusion of molecular oxygen in thin C_{60} films irradiated by femtosecond laser pulses are investigated. A comparison of the Raman scattering and absorbed energy spectra and the irradiation doses required to observe photopolymerization using continuous-wave radiation and femtosecond pulses shows that the efficiency of both photoinduced processes decreases considerably in the latter case. © *1998 American Institute of Physics.* [S0021-3640(98)01416-9]

PACS numbers: 82.50.−m, 81.05.Tp, 78.30.Na

The phototransformation of C_{60} by ultraviolet (UV) and visible radiation leads to the formation of materials with structural, chemical, and electrical properties which are considerably different from those of the initial material.[1] One such process is photopolymerization (PP), occurring in the solid phase of C_{60} (films and crystals) and resulting in the formation of a photoproduct which is insoluble in toluene and consists of dimers and polymers of covalently bonded C_{60} molecules.[2] Photopolymerization of C_{60} in films by continuous-wave (cw) visible- and UV-range light sources has been investigated intensively both under oxygen-free conditions and in the presence of oxygen.[1–5] Most studies have investigated the behavior of the most intense peak in the Raman scattering (RS) spectrum of C_{60} — the tangential mode $A_g(2)$ — whose position has been found to shift from 1469 cm^{-1} to 1458 cm^{-1} and whose intensity to drop severalfold in the PP process.

The well-known $2+2$ cycloaddition reaction leading to covalent bonding of van der Waals molecules in a molecular crystal has been proposed as the mechanism of PP.[4] In order for this reaction to proceed in solid C_{60} it is necessary to have a pair of fullerene molecules with the double bonds lying parallel and located a distance of not more than 0.42 nm from one another, and one molecule must be in the ground state while the other must be in the lowest triplet excited state.[5] The observed decrease in the PP efficiency in the presence of oxygen is attributed to efficient transfer of energy from C_{60} triplets to oxygen molecules, which are also in a triplet ground state. In this case the triplet oxygen

transforms into singlet oxygen (the quantum yield of this process is very high[6]), which in turn reacts with C_{60} in the ground state, forming carbonyl $C_{60}O_2$ (Ref. 6). Moreover, charge transfer between the fullerene and oxygen in octahedral voids[7] causes the free rotation of the C_{60} molecules to ''freeze,'' impeding the PP process, just as in the case of low temperatures. Another process lowering the efficiency of PP is a photoinduced increase of oxygen diffusion inside the sample, observed when films are irradiated by cw light sources.[8] In this case, oxygen filling the octahedral voids in a face-centered lattice between C_{60} molecules likewise impedes PP for the reasons indicated above, and carbonyl $C_{60}O_2$ is formed. As was shown in Ref. 9, the visible-range spectrum of an oxygen-filled sample is the same as that of the initial sample. At the same time, PP increases absorption in the red region, making it possible to detect this process visually according to the appearance of characteristic spots where darkening occurs.[5]

Photopolymerization is most efficient for C_{60} samples irradiated by cw UV sources.[10] The typical average intensities of radiation initiating PP lie in the range $1-100$ W/cm^2. For C_{60} films in air, as the average radiation intensity at 514 nm increases to values above 10^3 W/cm^2 the C_{60} core is destroyed, and amorphous carbon forms.[11] The PP of C_{60} by femtosecond laser pulses has still not been investigated experimentally, though the darkening spots, attributed to PP, in the films have been observed in the course of experiments where the films were irradiated by 230 fs pulses at 590 nm with intensities above 10^{10} W/cm^2 (Ref. 12). Special interest in such investigations arose after the publication of Ref. 13, where acceleration of relaxation of photoinduced absorption under oxygen-free conditions was observed after C_{60} films were irradiated for several minutes by comparatively low-intensity (10^6-10^7 W/cm^2) femtosecond pulses with a pulse repetition frequency of 82 MHz. According to an assertion made by the authors, it is the PP of C_{60} occurring as a result of the action of the femtosecond pulses on the sample in the course of the experiment itself that causes the acceleration of the observed relaxation. Moreover, the authors assert that as the intensity and correspondingly the density of excitations increase, the efficiency of the PP process should increase, so that virtually all of the published results of experiments on femtosecond spectroscopy of fullerene films must be reexamined.[13] Nonetheless, no experimental proof of the presence of PP (changes in the Raman spectra and photodarkening of the sample) was given in Ref. 13.

In contrast to Ref. 13, all of the published works on femtosecond spectroscopy of C_{60} were performed with films exposed to oxygen in air. A number of remarks concerning the interpretation of the results of Ref. 13 were made in Ref. 14, but the question of the efficiency of the PP of fullerenes under irradiation by femtosecond laser pulses has remained open up to now.

In the present letter we report on experiments on observations of PP and other photoinduced processes induced by femtosecond laser pulses in C_{60} films in the presence of oxygen.

C_{60} films ranging in thickness from 140 to 900 nm were investigated in the experiments. Prior to the experiments, the films were held in air under ordinary illumination for more than one year. Six (of eight) H_g and $2A_g$ modes, typical for C_{60} spectra, were observed in the RS spectra of the films in the range $200-1700$ cm^{-1}.

The films were irradiated with a cw argon laser at wavelength 514 nm

($10-1000\ \mathrm{W/cm^2}$) or 82 MHz pulses from a titanium sapphire laser at wavelength 395 nm (pulse duration 100 fs, average power $10-1000\ \mathrm{W/cm^2}$). The dynamics of the appearance of darkening spots, attributed to PP in the irradiated region, was observed under different irradiation conditions. The energy absorbed in the sample was measured at the same time. After irradiation the spots obtained were investigated by means of micro-RS. It should be noted that the observation of darkening spots was found to be a more sensitive method of observing PP than investigation of RS spectra.

We present below the results obtained on the same 150-nm-thick C_{60} film with a 200 μm focal spot. This made it possible to avoid the uncertainties associated with the influence of the film quantity and the size effect. The following observations were made in the experiments.

1. Photopolymerization was observed under irradiation with both cw radiation at 514 nm and femtosecond pulses at 395 nm. The minimum time for appearance of a spot was equal to 1–2 min in the first case and at least 10 min in the second case. The threshold irradiation dose required for PP spots to appear under cw irradiation decreased as the intensity increased from 50 to $300\ \mathrm{W/cm^2}$, and in the latter case it was found to be close to that observed under oxygen-free conditions[5] (about $20\ \mathrm{kJ/cm^2}$). The threshold for the appearance of PP under femtosecond irradiation with average power up to $95\ \mathrm{W/cm^2}$ was equal to $55\pm 5\ \mathrm{kJ/cm^2}$. As the power increased further, the threshold dose increased (by almost a factor of 3 at $130\ \mathrm{W/cm^2}$).

2. The RS spectra taken several weeks after irradiation in the darkening spots in the films showed changes characteristic for PP after both cw and pulsed irradiation. In both cases, a decrease in the intensity of the $H_g(1)$, $H_g(4)$, $A_g(1)$, and $A_g(2)$ lines, an increase in the $H_g(3)$ line, and splitting of all H_g lines were observed. The largest changes were observed in the region of the tangential mode $A_g(2)$ ($1469\ \mathrm{cm^{-1}}$) — its intensity decreased appreciably, the decrease being proportional to the observed darkening in the PP spot. The largest differences in the spectra of the spots obtained with cw and femtosecond irradiation were observed in the same region (see Fig. 1).

3. For the same density of PP spots, the RS spectrum after cw irradiation at 514 nm differed more strongly from the initial spectrum than after femtosecond irradiation. The dropoff in the intensity of the $A_g(2)$ line was found to be greater in the first case, and, in addition, broadening of this line was observed in the region of smaller wave numbers, the broadening increasing as the exposure time increased. In the case of femtosecond irradiation, there was no broadening, even for PP spots obtained with maximum exposures (780 min).

It should be noted that PP was not observed in the case that the samples were irradiated by femtosecond pulses at 790 nm for any powers, right up to powers which damage the samples, and exposures of up to several hours. In this case, up to 25% of the incident energy was absorbed in a film 140 nm thick.

A sum of Lorentzian lines was fit to the experimental spectra (Fig. 1) under the assumption that the investigated region of the spectrum contains lines belonging to the initial fullerene $A_g(2)$ and $H_g(7)$ ($1469\ \mathrm{cm^{-1}}$ and $1425\ \mathrm{cm^{-1}}$) together with lines belonging to the photoproducts: the photopolymer C_{60} ($1459\ \mathrm{cm^{-1}}$) and carbonyl $C_{60}O_2$. The spectrum of the unirradiated region was analyzed first (Fig. 1a). Assuming photopolymers to be absent in the unirradiated region, the best approximation gave a half-

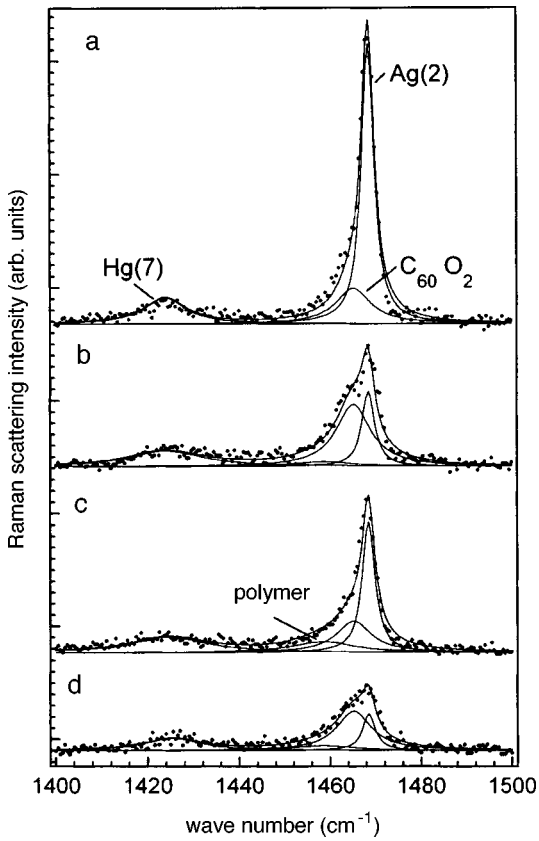

FIG. 1. Raman scattering spectra of unirradiated (a) and irradiated (b)–(d) regions of a 150 nm C_{60} film. All spectra were measured under identical conditions (excitation by cw 488 nm radiation, 50 W/cm^2, excitation spot diameter 50 μm, measurement time of each spectrum 15 min). Irradiation conditions: Pulsed 82 MHz, 100 fs, 395 nm, 95 W/cm^2, 75 min — (c); cw at 514 nm: 85 W/cm^2, 85 min — (b) 200 W/cm^2, 40 min — (d). The dots show the results of the measurements, the solid lines show the results of fitting Lorentzian contours to the experimental data.

width of 3.5 cm^{-1} for the 1469 cm^{-1} line and, for the $C_{60}O_2$ line, a position of 1465 cm^{-1}, in good agreement with the data of Ref. 1, and a half-width of 10 cm^{-1}. These data were then used to fit the spectra of the irradiated regions (Figs. 1b–1d). The position (1459 cm^{-1}) and half-width (17 cm^{-1}) of the photopolymer line were taken from Ref. 5. As one can see from Figs. 1b–1d, in all the spectra the photopolymer line obtained as a result of the fit is at the noise level. This is due to, first, the strong broadening and factor of 3 decrease in the cross section of the RS line $A_g(2)$ accompanying PP and, second, the appearance of the strong carbonyl line at 1465 cm^{-1}, substantially masking the PP line. Nonetheless, the fractions of the photopolymerized molecules estimated assuming that the loss of molecules in the initial state equals the number of $C_{60}O_2$ molecules and photopolymers appearing are 35, 50, and 60% for the spectra b, c, and d, respectively, which agrees qualitatively with the photodarkening observed for these cases. For the RS spectra observed after cw irradiation, an increase is clearly seen

in the intensity of the $C_{60}O_2$ line at 1465 cm^{-1} as compared with the spectrum of the unirradiated sample (Fig. 1a), the increase being all the greater the lower the intensity of the irradiating light and the longer the irradiation time (Figs. 1b and 1d). The greatest difference of the RS spectrum observed after femtosecond irradiation (Fig. 1c) is the absence of such an increase even at the longest irradiation times.

Measurements of the absorbed energy required to observe PP showed that in C_{60} films this process is much less efficient in the case of irradiation by 395 nm femtosecond pulses than for 514 nm cw radiation with the same average intensity ~ 100 W/cm^2, though in the first case the absorption is greater. Estimates based on the experimental data presented above show that the absorption of 2×10^6 photons per molecule is sufficient to observe PP with cw irradiation, while in the case of femtosecond irradiation this number is 7 times larger (with a higher photon energy). The decrease in efficiency in the latter case is due to the high peak power of the femtosecond pulses. Under the conditions of our experiments, the maximum density of the excited molecules for pulsed irradiation is five orders of magnitude higher than for cw irradiation with the same average power. In this case, the intermolecular relaxation (mainly singlet–singlet annihilation[9]) is much more rapid than the transition of molecules into triplet states, which are the initial states for PP. Therefore the assumption[13,15] of efficient formation of C_{60} dimers and photopolymers in the case of a high density of excited molecules is not confirmed by the present experiment.

The difference of the RS spectra for identical PP spots in the case of pulsed and cw irradiations permits drawing some conclusions about the character of the photoinduced diffusion of oxygen in the two cases. The increase in the $C_{60}O_2$ line in the spectrum after cw irradiation is due to the photoinduced diffusion of oxygen into the interior of the sample.[1,8] The absence of such an increase in the spectrum (Fig. 1c) shows that photoinduced diffusion does not occur in the case when the C_{60} film is irradiated with femtosecond pulses. The physical reasons for this phenomenon have yet to be determined. In the case of cw irradiation the photoinduced diffusion of oxygen is due to the excitation of C_{60} molecules (the efficiency is higher for UV irradiation) when the O_2 pressures outside and inside the sample are different (the reverse process is observed in vacuum).[8]

It follows from the experiments performed that the change in the character of the excitation of C_{60} molecules in a film as a result of a change in the temporal structure of the exciting radiation will make it possible to control the course of photochemical reactions. Photoinduced diffusion of oxygen in the presence of cw irradiation results in quenching of C_{60} triplets and subsequent formation of carbonyl $C_{60}O_2$ in the bulk of the sample. Under femtosecond irradiation this reaction channel is blocked. This means that the conditions of PP by femtosecond pulses in sufficiently thick (of the order of several tens of nm) C_{60} films are virtually identical for oxygen-free films and films held in air for a certain time. For this reason, the process leading to a shortening of the relaxation time of photoinduced absorption in C_{60} films in Ref. 13 at a characteristic irradiation dose ~ 1 kJ/cm^2 at 463 nm apparently is not associated with PP, since the PP threshold dose measured in these experiments is several tens of times higher.

The investigations described in the present letter were made possible by Grant RP2-154 from the CRDF.

[a)]e-mail: chekalin@isan.troitsk.ru

[1] A. F. Hebard, K. B. Lyons, and R. C. Haddon, Electrochem. Soc. Proc. **95-10**, 11 (1995).
[2] A. M. Rao, P. Zhou, K.-A. Wang *et al.*, Science **259**, 955 (1993).
[3] P. Zhou, Z.-H. Dong, A. M. Rao *et al.*, Chem. Phys. Lett. **211**, 337 (1993).
[4] Y. Wang, J. M. Holden, Z.-H. Dong *et al.*, Chem. Phys. Lett. **211**, 341 (1993).
[5] L. Akselrod, H. J. Byrne, C. Thomsen *et al.*, Chem. Phys. Lett. **212**, 384 (1993).
[6] C. Taliani, G. Ruani, R. Zamboni *et al.*, J. Chem. Soc. Chem. Commun. **3**, 220 (1993).
[7] B. Pevzner, A. F. Hebard, and M. S. Dresselhaus, Phys. Rev. B **55**, 16439 (1997).
[8] P. Zhou, A. M. Rao, K.-A. Wang *et al.*, Appl. Phys. Lett. **60**, 2871 (1992).
[9] S. R. Flom, F. J. Bartoli, H. W. Sarkas *et al.*, Phys. Rev. B **51**, 11376 (1995).
[10] A. Ito, T. Morikava, and T. Takahashi, Chem. Phys. Lett. **211**, 333 (1993).
[11] M. Manfredini, C. E. Bottani, and P. Milani, Chem. Phys. Lett. **226**, 600 (1994).
[12] S. V. Chekalin, V. M. Farztdinov, E. Okesson *et al.*, JETP Lett. **58**, 295 (1993).
[13] S. B. Fleischer, B. Pevzner, D. J. Dougherty *et al.*, Appl. Phys. Lett. **69**, 296 (1996).
[14] S. V. Chekalin, Appl. Phys. Lett. **71**, 1276 (1997).
[15] V. M. Farztdinov, A. L. Dobryakov, V. S. Letokhov *et al.*, Phys. Rev. B **56**, 4176 (1997).

Translated by M. E. Alferieff

Semiconductor–metal transition in FeSi in ultrahigh magnetic fields up to 450 T

Yu. B. Kudasov, A. I. Bykov, M. I. Dolotenko, N. P. Kolokol'chikov, M. P. Monakhov, I. M. Markevtsev, V. V. Platonov, V. D. Selemir, O. M. Tatsenko, and A. V. Filippov
Russian Federal Nuclear Center, 607190 Sarov, Nizhnegorod Region, Russia

A. G. Volkov, A. A. Povzner, P. V. Bayankin, and V. G. Guk
Ural State Technical University, 620002 Ekaterinburg, Russia

(Submitted 1 July 1998; resubmitted 22 July 1998)
Pis'ma Zh. Éksp. Teor. Fiz. **68**, No. 4, 326–330 (25 August 1998)

The magnetic susceptibility and conductivity of single-crystal iron monosilicide are investigated in ultrahigh magnetic fields up to 450 T at a temperature of 77 K. It is found that the conductivity of iron monosilicide increases continuously by two orders of magnitude as the magnetic field increases. The results obtained can be interpreted as a semiconductor–metal transition induced by the magnetic field. The dependence of the conductivity on the magnetic field is described well on the basis of the spin-fluctuation theory.
 [S0021-3640(98)01516-3]

PACS numbers: 75.30.Cr, 75.50.Pp, 72.20.My

The unusual spectroscopic,[1] thermodynamic,[2] and magnetic properties of iron monosilicide (FeSi) have been attracting the attention of investigators for a long time. Different theoretical models,[3–7] which take into account the strong electronic correlations in the narrow bands formed by the *d* electrons of iron, have been used to explain the observed anomalies. The electron effective masses obtained from band calculations,[8] though quite high, are nonetheless much lower than the experimental values, which indicates strong mass renormalization due to electron–electron interactions. A number of recent theoretical works (see, for example, Refs. 9 and 10) have predicted a metamagnetic transition in FeSi at a magnetic induction B of about 200 T, accompanied by a jump in the magnetic moment by an amount of the order of 1 Bohr magneton μ_B.

In the present letter we report the results of an investigation of the magnetic susceptibility and conductivity of single-crystal FeSi in ultrahigh magnetic fields. Since the Zeeman splitting in magnetic fields with induction of the order of the several hundred tesla is comparable to the band gap δ in the spectrum of the *s*, *p*, and *d* electrons in FeSi ($\delta = 0.11$ eV[11]), it can lead to a radical restructuring of the electronic spectrum. For this reason, ultrahigh magnetic fields are a powerful tool for investigating the electronic structure of this material.

We employed an MK-1 magnetoaccumulation generator to produce magnetic fields with induction up to 450 T.[12] At the present time this is the only setup in the world that

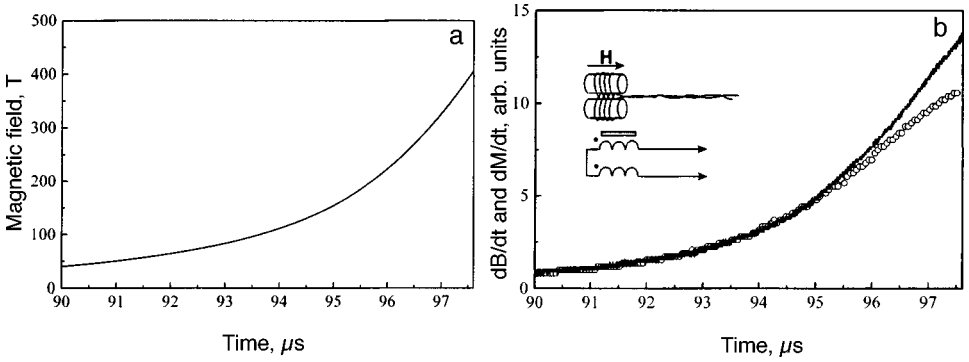

FIG. 1. a) Time dependence of the magnetic field at the final stage of the pulse, b) derivative of the magnetic field according to the magnetic pickup (solid line) and the signal from the compensation sensor (○). Inset: Schematic diagram of the compensation sensor (the arrow marks the direction of the magnetic field) and its electrical circuit.

makes it possible to obtain reproducible uniform magnetic fields with B up to 1000 T in large useful volumes.[12] The initial magnetic field ($B \approx 16$ T), produced in a thin-walled multistart helical solenoid by discharging a high-power capacitor bank, is intensified by using the products of the explosion to compress a conducting cylinder. The compression time of the initial magnetic flux equals about 16 μs. The MK-1 generator was assembled in a single-cascade variant, i.e., without intermediate internal cascades;[12] while this decreased the peak value of the magnetic induction somewhat (to 450 T), it made it possible to obtain a smooth magnetic field pulse (see Fig. 1a). The useful volume with the maximum magnetic field consisted of a cylinder approximately 10 mm in diameter and 100 mm long.

The samples and the magnetic-field pickups were placed on a plate made of fiberglass laminate and immersed in liquid nitrogen in a foam plastic vessel. Since the growth rate of the magnetic field changes strongly in the course of the field generation process (from ≈ 0.5 T/μs at the time when the initial magnetic field is produced, up to $\approx 10^2$ T/μs at the end of the pulse), it is difficult to measure the magnetic field to a high degree of accuracy with a single magnetic pickup during the entire pulse. For this reason, a collection of single-turn magnetic pickups ranging in diameter from 0.8 mm to 14.0 mm, wound with PETV-2 enameled wire ranging in diameter from 71 μm to 0.25 mm, was used. Previous investigations (see, for example, Refs. 12 and 13) showed that this method makes it possible to achieve 5–10% measurement accuracy in fields up to 500 T. The signals were displayed on Tektronix 744 four-channel oscilloscopes.

The FeSi single crystals employed in the experiments were grown in the $\langle 100 \rangle$ direction by the Czochralski method in an atmosphere of spectroscopically pure helium under a pressure of 0.4 atm. The crystal growth rate was equal to 0.4 mm/min with the crucible containing the melt and the crystal rotating in opposite directions at a rate of 3 rpm. Carbonyl iron with a purity of 99.98% and zone-refined semiconductor silicon served as the initial components. The preparation of the FeSi single crystals is described in detail in Ref. 14.

The magnetic susceptibility was measured in a compensation pickup (see inset to

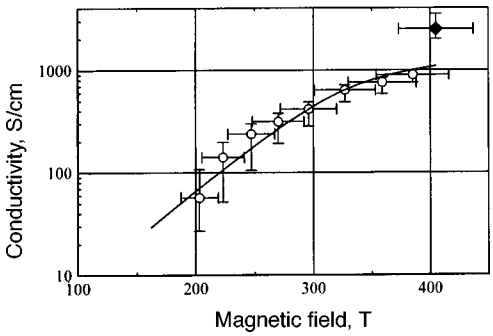

FIG. 2. Conductivity of FeSi powder (○) and a single-crystal slab (◆) in a magnetic field. The solid line is the dependence computed on the basis of the spin-fluctuation theory.

Fig. 1b).[15] PÉTV-2 wire with a diameter of 71 μm was laid in spiral grooves of two caprolon frames 2 mm in diameter, each with $N=9$ turns. The degree of compensation of the coils was tested in a high-frequency magnet. The total areas NS of the coils, where S is the area of one turn, differed by not more than 2%. An opening 1.6 mm in diameter was drilled into one of the frameworks in order to install the experimental sample. The FeSi single crystal was ground in a porcelain mortar to a powder with approximately 100 μm granules and mixed with polymethyl methacrylate, which was then polymerized using dichloroethane. As a result, we obtained single-crystal FeSi powder in a dielectric matrix. This made it possible to avoid the appearance of an additional diamagnetic moment of the sample on account of induction currents during the magnetization measurements. The jumps of the magnetic moment at metamagnetic transitions lead to the appearance of sharp peaks in the signal from the sensor.[15] The sensitivity of the method was equal to about 0.5 μ_B. In the experiment with FeSi powder in a dielectric matrix, no peaks were observed in the signal from the compensation sensor.

An induction measurement of the conductivity was performed in a compensation sensor, similar to the one described above, except that the opening for the sample was densely filled with pure FeSi powder. In a pulsed magnetic field, an additional diamagnetic moment associated with the conductivity of the powder appeared in the powder. In our case the magnetic field was axial and uniform, and the condition $\lambda \gg r$, where λ is the depth of the skin layer and r is the radius of the conducting cylinder, was always satisfied. Then, from the diffusion the equation for the magnetic field $\Delta B=(1/\mu_0\sigma)\partial B/\partial t$, where μ_0 is the magnetic permeability of vacuum and σ is the conductivity of the powder [Note: here Δ denotes the Laplacian operator], we obtain the following expression for calculating the time dependence of the conductivity:

$$\sigma(t)=4\int \Delta U d\tau/a^4\mu_0 B(t)N, \tag{1}$$

where ΔU is the additional emf associated with induction currents in the powder. Figure 1b shows signals from the magnetic pickup and from the compensation sensor with FeSi powder. Here, an additional induction emf is clearly seen against the background decompensation emf of the pickup (derivative of the magnetic field). The conductivity of the powder, calculated from the data in Fig. 1b using Eq. (1), is presented in Fig. 2. An

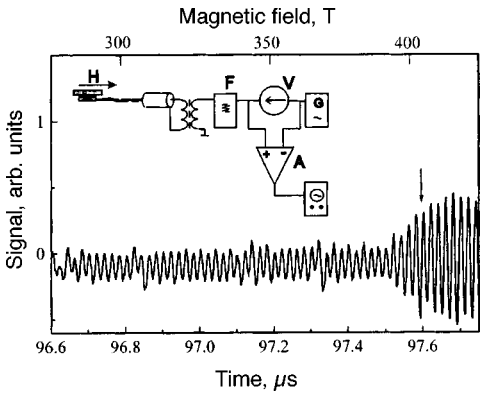

FIG. 3. The rf circuit for measuring the conductivity, and the rf signal obtained in the experiment.

estimate of the heating of the powder by the induction currents up to the time of the maximum magnetic induction equals ~5 K.

We also measured the conductivity of a $4\times4\times0.3$ mm single-crystal FeSi slab. A radio-frequency (rf) method was used for this. The measurement scheme is shown in Fig. 3. A G4-154 generator served as the rf source. The frequency of the oscillations was about 49 MHz. The rf signal was fed through the rectifier *V*, bandpass filter *F*, and dividing transformer to a cable approximately 30 m in length, to whose other end a flat coil 3 mm in diameter, consisting of five turns of PÉTV-2 wire 71 μm in diameter, was connected. The ends of the coil were led out of the MK-1 generator as a twisted pair. The coil axis was perpendicular to the direction of the external magnetic field, thereby decreasing the emf induced by a pulse of this field. The plane of the slab was parallel to the external magnetic field, thereby preventing strong heating of the sample by the induction fluxes (according to our estimates, the maximum heating did not exceed 4 K). The incident rf wave was reflected from the cable end to which the coil was attached; the reflection coefficient depended on the conductivity of the slab. The subtraction circuit *A* made it possible to extract the reflected signal, which was then displayed on an oscillograph. The electrodynamics of this measurement scheme is similar to that used in Ref. 16, but it is more noise resistant than the latter. The rf circuit for conductivity measurements will be published in detail separately.

The dynamic range of the rf method of measuring the conductivity is limited on the low end. For this reason, this method enabled us to fix only the moment at which the conductivity of the single-crystal FeSi slab appears at the level 2×10^4 S/cm (the conductivity was measured by a method similar to the one used in Ref. 16). The rf signal is shown in Fig. 3, where the onset of conductivity at 400 T is clearly seen.

The results obtained in this work indicate the absence of an abrupt singlet semiconductor–ferromagnetic metal transition in FeSi, which was predicted in Refs. 9 and 10, at least up to 450 T at $t=77$ K. Instead, we observed a continuous increase of the conductivity of FeSi by approximately two orders of magnitude in a 450 T field as compared with zero field. Since the effective masses of the mobile charge carriers in FeSi are very large (much larger than the free-electron mass), in contrast to ordinary narrow-gap semiconductors and semimetals such as InSb, PbTe, Bi, and so on, the behavior of

this semiconductor in a magnetic field is quite unusual. The splitting between the Landau levels in FeSi is very small and orbital quantization can be neglected. Then the band gap should decrease linearly in the field as a result of the Zeeman splitting of the valence and conduction bands.

However, the nonlinear character of the dependence $\ln\sigma(B)$ should be noted. The change in the slope of the $\ln\sigma(B)$ curve could be due to renormalization of the electronic spectrum by spin fluctuations in the system of strongly correlated *d* electrons and collapse of the gap in the energy spectrum. We showed on the basis of the spin-fluctuation theory[3,6] that the Zeeman splitting of the *d*-electron spectrum increases as a result of spin fluctuations described by fluctuating exchange ξ fields

$$E(k)=E_0(k)\pm U_m(\xi,H), \tag{2}$$

where $E_0(k)$ is the spectrum of noninteracting *d* electrons, $U_m(\xi,H)=[(UM_0+H)^2+\xi^2]^{1/2}$ is the effective Zeeman splitting of the energy spectrum of *d* electrons in a magnetic field of intensity H (expressed in units of $2\mu_B$) in the presence of spin fluctuations, M_0 is the uniform magnetization of the *d* subsystem, and U is the intra-atomic Coulomb interaction parameter, while the magnitude ξ of the fluctuation-induced splitting, in accordance with Refs. 3 and 6, is given by the relation $\xi=U\langle m^2\rangle^{1/2}$.

The amplitude of the thermal spin fluctuations for the semiconductor state of the *d* electrons in FeSi can be calculated from the formula $\langle m^2\rangle^{1/2}=bT$, where $b=0.9/U$ and $U=0.8$ eV. Numerical estimates of the magnetic induction corresponding to the collapse of the gap in the spectra of the *d*, *s*, and *p* electrons at temperature 77 K give $B_d=275$ T and $B_s=389$ T, respectively. Therefore the observed deviation of the experimental dependence $\ln\sigma(B)$ from linearity above 250 T could be due to the appearance of a metallic state in the *d*-electron system. The field dependence of the conductivity of FeSi, calculated on the basis of the spin-fluctuation theory, is presented in Fig. 2.

In conclusion, we note that the contribution of *s* and *p* electrons to the conductivity is small for low magnetic inductions and increases appreciably in fields with $B>40$ T.

The investigation in ultrahigh magnetic fields was performed as part of the ''Kapitsa'' series of experiments with the support of the Ministry of Atomic Energy of the Russian Federation and the Ministry of Science and Technology of the Russian Federation.

[1] D. van der Marel, A. Damascelli, and K. Schulte, E-preprint LANL, cond-mat 9701005 [*sic*].
[2] V. Jaccarino, G. R. Wertheim, and J. H. Wernic, Phys. Rev. **160**, 476 (1967).
[3] P. V. Gel'd, A. G. Volkov, A. A. Povzner, and V. Yu. Ivanov, Dokl. Adad. Nauk SSSR **320**, 1097 (1991) [Sov. Phys. Dokl. **36**, 698 (1991)].
[4] M. B. Hunt, M. A. Chernikov, E. Felder, and H. R. Ott, Phys. Rev. B **50**, 14933 (1994).
[5] C. M. Varma, Phys. Rev. B **50**, 9952 (1994).
[6] P. V. Gel'd, A. A. Povzner, and A. G. Volkov, Dokl. Akad. Nauk SSSR **283**, 358 (1985) [Sov. Phys. Dokl. **30**, 585 (1985)].
[7] C. Fu, M. Krijn, and S. Doniach, Phys. Rev. **49**, 2219 (1994).
[8] L. F. Mattjeiss and D. R. Hamann, Phys. Rev. B **47**, 13114 (1993).
[9] V. I. Anisimov, S. Yu. Ezhov, and I. S. Elfimov, Phys. Rev. Lett. **76**, 1735 (1996).
[10] E. Kulatov, H. Ohta, T. Arioka *et al.*, *Fifth International Symposium on Research in High Magnetic Fields*, Sydney, Australia, 4–6 August, 1997.
[11] L. I. Vinokurova, A. V. Vlasov, and É. T. Kulatov, Trudy IOFAN **32**, 26 (1991).
[12] A. I. Pavlovskiĭ and R. Z. Lyudaev, in *Problems of Modern Experimental Science and Technology* [in Russian], edited by A. P. Aleksandrov, Nauka, Leningrad, 1984, p. 206.

[13] B. A. Boiko, G. V. Boriskov, A. I. Bykov *et al.*, *Eleventh IEEE International Pulsed Power Conference*, edited by G. Cooperstein and I. Vitkovsky, IEEE Inc., New York, 1997, p. 1486.
[14] A. A. Frolov, Trudy IOFAN **32**, 26 (1991).
[15] I. S. Dubenko, A. K. Zvezdin, A. S. Lagutin *et al.*, JETP Lett. **64**, 202 (1996).
[16] T. Sakakibara, T. Coto, and N. Miura, Rev. Sci. Instrum. **60**, 444 (1989).

Translated by M. E. Alferieff

Magnetic and structural transitions in $La_{1-x}Sr_xMnO_3$: $T-x$ phase diagram

A. A. Mukhin,[a] V. Yu. Ivanov, V. D. Travkin, and S. P. Lebedev
Institute of General Physics, Russian Academy of Sciences, 117942 Moscow, Russia

A. Pimenov and A. Loidl
Universität Augsburg, D-86159 Augsburg, Germany

A. M. Balbashov
Moscow Power Engineering Institute, 105835 Moscow, Russia

(Submitted 9 July 1998; resubmitted 22 July 1998)
Pis'ma Zh. Éksp. Teor. Fiz. **68**, No. 4, 331–336 (25 August 1998)

The electrical conductivity, magnetic susceptibility, magnetization, and submillimeter ($\nu=5-20$ cm^{-1}) permittivity and dynamic conductivity of $La_{1-x}Sr_xMnO_3$ ($0\leqslant x\leqslant 0.45$) single crystals are investigated. The anomalies in the temperature dependences of these quantities are identified with diverse magnetic and structural phase transformations, including antiferromagnetic and ferromagnetic ordering, structural transitions between strongly distorted (Jahn–Teller) and weakly distorted (pseudocubic) orthorhombic phases, structural transitions to a rhombohedral phase and unusual transitions to a polaron-ordering state. As a result, the complete $T-x$ phase diagram of the system $La_{1-x}Sr_xMnO_3$ is constructed in a wide interval of temperatures $T=4.2$–1050 K and concentrations $x=0$–0.45. © *1998 American Institute of Physics.* [S0021-3640(98)01616-8]

PACS numbers: 75.30.Kz, 61.50.Ks, 72.20.My, 75.50.Dd

Currently there is a great deal of interest in the investigation of substituted manganites $R_{1-x}A_xMnO_3$, where R is a rare earth and A =Ca,Sr, . . . This is due to the discovery of colossal magnetoresistance[1] as well as diverse magnetic and structural phase transformations[2,3] in these materials. These compounds all have the property that on doping with divalent Ca and Sr ions their magnetic structure changes from antiferromagnetic (with weak ferromagnetism) at $x=0$ to ferromagnetic at $x=0.2$–0.3, and their resistance decreases strongly.[2] Their crystal structure also undergoes a number of transformations. For example, as the Sr content in $La_{1-x}Sr_xMnO_3$ increases, the crystal symmetry changes from orthorhombic to rhombohedral, and in the intermediate Sr concentration range $x=(0.1$–$0.15)$ an unusual polaron-ordered state is observed, which neutron diffraction data[4] show to be due to an ordered arrangement of heterovalent ions Mn^{3+}/Mn^{4+} in alternating (001) planes and to the formation of a corresponding superstructure.

$T-x$ diagrams which, to a certain extent, take into account the observed phase

transformations in $La_{1-x}Sr_xMnO_3$ have been proposed in a number of works.[4–7] However, these investigations were performed for a small set of compositions and in a limited temperature interval, so that the phase diagrams are mainly of a schematic character, and in some places they even contradict one another (see, for example, Refs. 4, 5, and 7).

In the present work complete investigations were performed of the magnetic and structural phase transitions in $La_{1-x}Sr_xMnO_3$ in a wide interval of temperatures (up to 1050 K) and concentrations ($0 \leqslant x \leqslant 0.45$) on the basis of measurements of their static (magnetization, susceptibility, resistance, magnetoresistance) and submillimeter dynamic properties (permittivity, conductivity). Specifically, the permittivity was observed to increase strongly at phase transitions to a polaron-ordering state, and for lightly doped compositions two structural phase transformations were observed at high temperatures. As a result, the complete T–x phase diagram of the system was constructed.

We investigated $La_{1-x}Sr_xMnO_3$ ($0 \leqslant x \leqslant 0.45$) single crystals grown by the floating-zone method with radiation heating. The resistivity $\rho(T)$ was measured by a four-probe method in the temperature interval $4.2 \leqslant T \leqslant 1050$ K. The magnetic susceptibility $\chi_{ac}(T)$ was measured by an induction method at frequencies ranging from 4 Hz up to 2.5 kHz at $T = 4.2 - 300$ K. The amplitude of the ac field ranged from fractions of an oersted to several kOe. The measurements of the magnetization $M(H)$ were performed on a vibrating-coil magnetometer in fields up to 14 kOe at temperatures $T = 4.2$–300 K.

The dynamic properties were investigated by submillimeter quasioptic backward-wave-tube (BWT) spectroscopy[8] in the frequency range $\nu = 5$–20 cm^{-1} at $T = 5 - 300$ K. The transmission $T(\nu)$ and phase $\varphi(\nu)$ spectra of plane-parallel samples with transverse dimensions of 8–10 mm and thickness 0.1–1 mm were measured, and the results were used to determine the complex permittivity spectrum $\epsilon = \epsilon' + i\epsilon''$ or the dynamic conductivity spectrum $\sigma = \sigma' + i\sigma''$ using the well-known formulas for the transmission of a plane-parallel slab.

The results of the measurements of the temperature dependences of the magnetic susceptibility and resistance for different concentrations are presented in Figs. 1 and 2, while Fig. 3 illustrates the temperature behavior of the submillimeter permittivity and dynamic conductivity for $x = 0.125$ together with the static conductivity, magnetic susceptibility, and magnetization. One can see that the temperature dependences of these quantities exhibit a number of anomalies, which are designated in the figures by different symbols and which we identified with different magnetic and structural phase transitions. The temperatures of the corresponding phase transformations depend strongly on the composition and are represented in the form of the T–x phase diagram in Fig. 4.

The sharp peak in the susceptibility $\chi_{ac}(T)$ (Fig. 1), observed for pure $LaMnO_3$, is due to the antiferromagnetic ordering of Mn^{3+} ions at the Néel point $T_N = 140$ K. Below T_N spontaneous and remanent magnetization appear, attesting to the fact that the magnetic structure is not purely antiferromagnetic but rather weakly ferromagnetic. A similar behavior of $\chi_{ac}(T)$ and the magnetization also occurs for lightly doped compositions ($x = 0.05$ and 0.075), the only difference being that the spontaneous magnetization in this case increases considerably: from ≈ 4 G·cm^3/g for $x = 0$ up to ≈ 17 and ≈ 25 G·cm^3/g, respectively, for $x = 0.05$ and 0.075 at $T = 4.2$ K. This indicates a strong increase in the degree of noncollinearity of the magnetic structure as x increases. The behavior of the antiferromagnetic resonance (AFMR) which we observed in pure and lightly doped

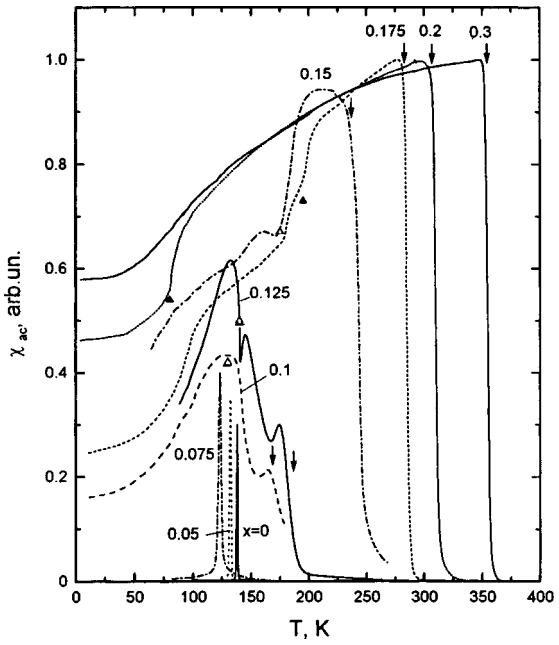

FIG. 1. Temperature dependences of the magnetic susceptibility of $La_{1-x}Sr_xMnO_3$ single crystals. The arrows mark the Curie temperatures; the symbols ▲ mark the temperatures of transitions between the rhombohedral R and orthorhombic O^* phases; the symbols △ mark the temperatures of the transition to the polaron-ordering phase P.

$LaMnO_3$[9] — the AFMT frequencies decrease appreciably as the Sr content increases (19 cm^{-1} and 6 cm^{-1} for $x=0$ and 0.05, respectively), while AFMR vanishes for $x \geqslant 0.1$ — also indicates suppression of antiferromagnetic order as the doping level increases.

At high doping levels ($x \geqslant 0.15$) the $\chi_{ac}(T)$ curves have a sharp anomaly (marked by the arrow), associated with the appearance of ferromagnetic order at $T=T_C$. As x decreases and T_C decreases (Fig. 4), the ordered state apparently becomes magnetically nonuniform, as is indicated by the smeared character of the transition on the $\chi_{ac}(T)$ curves as $T \to T_C$ for $x=0.1$ and 0.125. In addition, the maximum susceptibility χ_{ac} is less than the value $1/N$ corresponding to the maximum susceptibility at the Curie point of a homogeneous ferromagnet with demagnetizing factor N. We arrive at the same conclusion also from an analysis of the field dependences of the magnetization: The initial slope of the curves $M(H)$ at temperatures $T<T_C$ is less than that for compositions with $x \geqslant 0.175$, and saturation is not reached in fields up to 13 kOe. The nonuniformity of the magnetic state is apparently greatest in the hatched region of concentrations 0.8–0.9 in the phase diagram, where the lines $T_C(x)$ and $T_N(x)$ come together, and here the details of the diagram require additional investigation.

As one can see from Fig. 2, as the Sr content increases, the resistivity at low temperatures decreases from values $\gg 10^6\ \Omega \cdot cm$ (the instrumental measurement limit) to $\approx 4.7\text{–}10^{-5}\ \Omega \cdot cm$ for the compound with $x=0.3$. The form of the $\rho(T)$ curves on the whole corresponds to the results of Ref. 2, which were also obtained for single crystals

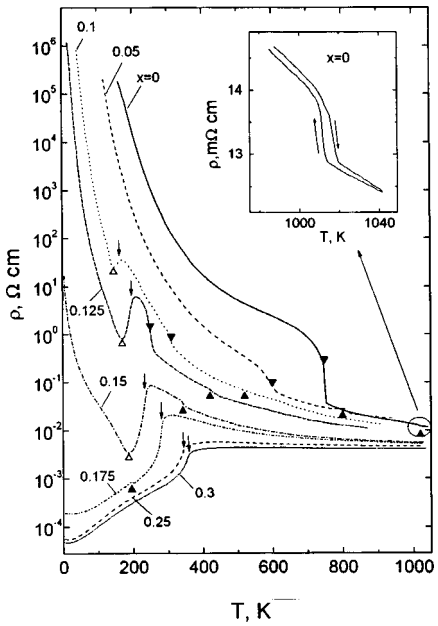

FIG. 2. Temperature dependences of the resistivity ρ of $La_{1-x}Sr_xMnO_3$ single crystals. The arrows mark the Curie temperatures; the symbols ▲ mark the temperatures of the transition between the R and O^* phases; ▼ mark the temperatures of the transition between the two orthorhombic phases O' and O^*; and, △ mark the temperatures of the transition to the polaron-ordering phase P. Inset: Behavior of $\rho(T)$ accompanying a structural phase transition $O^* \rightarrow R$ in pure $LaMnO_3$.

but at temperatures $T < 500$ K. For compounds with $x \geqslant 0.15$ the value of T_C determined from the anomalies on the $\chi_{ac}(T)$ curves, and the maxima of the magnetoresistance approximately corresponds to the maximum of the derivative $d\rho/dT$. The resistivity minimum, marked by the open triangles, below T_C and the change in the behavior of $\rho(T)$ from metallic to semiconductor behavior, which are observed for compositions with $0.1 \leqslant x \leqslant 0.15$, attest to strong charge-carrier localization at low temperatures and, as neutron-diffraction investigations show,[4] a transition to a polaron-ordering phase P at $T = T_p$. We note that additional anomalies, marked by open triangles, are also observed at this transition on the $\chi_{ac}(T)$ curves for $x = 0.1$, 0.125, and 0.15 (Fig. 1).

Here what is meant by a polaron is a hole in the e_g orbitals of the Mn^{3+} ion (i.e., actually a Mn^{4+} ion), surrounded by a corresponding local distortion of the lattice. Since the Mn^{4+} ion, in contrast to the Jahn–Teller Mn^{3+} ion, does not give rise to strong local distortion of oxygen octahedra, the lattice symmetry increases near such a polaron. According to Ref. 4, the polaron phase P is an ordered arrangement of Mn^{3+} and Mn^{4+} ions for which one of the two alternating atomic layers in the (001) plane contains only Mn^{3+} ions, as in pure $LaMnO_3$, while the other layer contains both Mn^{3+} and Mn^{4+} ions, i.e., holes. For the optimal concentration $x = 0.125$, the holes in this layer occupy 1/4 of the positions of manganese and form a quadrupled (2×2) square lattice with the respect to the initial perovskite cubic cell. As a result, a superstructure with wave vector (1/2, 1/2, 1/4) is formed. This structure apparently remains even in the presence of a small devia-

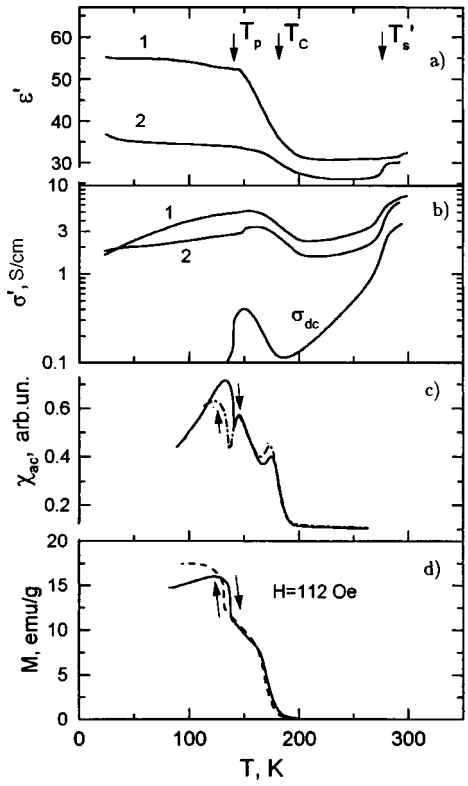

FIG. 3. Temperature dependences of the permittivity $\epsilon'(13.3\ \mathrm{cm}^{-1})$ (a), dynamic conductivity $\sigma'(13.3\ \mathrm{cm}^{-1})$ and static conductivity σ_{dc} (b), magnetic susceptibility χ_{ac} (c) and magnetization M (d) of $La_{1-x}Sr_xMnO_3$. The labels 1 and 2 for ϵ' and σ' correspond to different polarizations of the radiation. The vertical arrows mark the temperatures of the polaron (T_p) and magnetic (T_C) orderings and the structural transition $O' \rightarrow O^*$ (T_s').

tion of the Sr concentration from the optimal value 0.125 (within the range from 0.1 to 0.15).

Besides the anomalies associated with polaron ordering, other anomalies are also observed in the temperature dependences $\rho(T)$ in samples with $x \leqslant 0.2$. We attribute the most pronounced ones, which are marked by the symbols ▼, to a phase transition from a strongly distorted Jahn–Teller orthorhombic phase O' with *Pnma* symmetry ($b/\sqrt{2} < c < a$) to a weakly distorted orthorhombic (pseudocubic) structure O^* ($b/\sqrt{2} \sim a \sim c$) at T_s', relying in so doing on the neutron diffraction data given in Ref. 5 for the composition $x = 0.125$, where the same transition is observed at $T_s' \approx 250$ K. The temperature of this transition increases rapidly as the concentration x decreases and reaches 750 K at $x = 0$, while in the process the resistance changes abruptly by almost an order of magnitude. A similar behavior of ρ at a Jahn–Teller transition in pure $LaMnO_3$ was also observed in Ref. 10.

In addition, we observed in the temperature dependences $\rho(T)$ at higher temperatures a second transition accompanied by a weaker jump in the resistivity and marked by the symbol ▲ in Fig. 2 (see inset for $x = 0$). As x increases, the temperature T_s of this

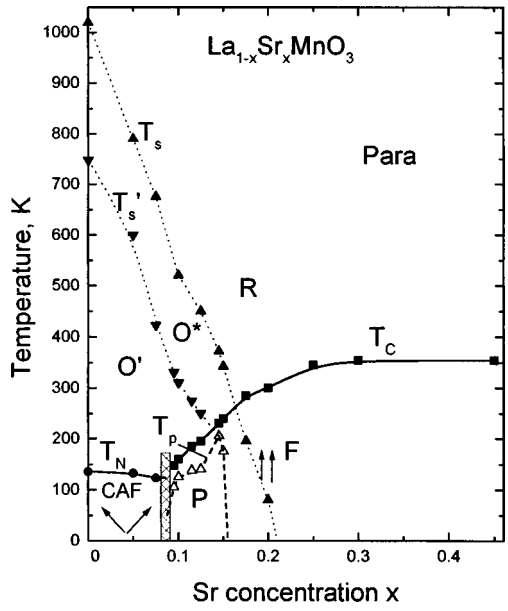

FIG. 4. Structural and magnetic T–x phase diagram of $La_{1-x}Sr_xMnO_3$. R — rhombohedral phase; O^* — weakly distorted orthorhombic phase; O' — strongly distorted (Jahn–Teller) orthorhombic phase; P — polaron-ordering phase; Para — paramagnetic state; F — ferromagnetic state; CAF — noncollinear phase; T_C and T_N — Curie and Néel temperatures; T_s and T_s' — temperatures of the transitions $O^*\rightarrow R$ and $O'\rightarrow O^*$, respectively; and, T_p — temperature of the transition to the polaron-ordering phase.

transition decreases appreciably, and for $x\geqslant 0.14$ the transition temperatures agree well with published data for a structural transition between orthorhombic O^* and rhombohedral R phases.[2,6] This gives us a basis for identifying the observed transitions as $O^*\rightarrow R$ right down to $x=0$. In the region of magnetic ordering, for $x=0.175$ and 0.2, these transitions also manifest themselves in the form of a sharp change in the susceptibility (Fig. 1) and magnetization. Therefore two high-temperature structural phase transitions $O'\rightarrow O^*$ and $O^*\rightarrow R$, corresponding to the lines $T_s'(x)$ and $T_s(x)$ on the phase diagram in Fig. 4, occur in $La_{1-x}Sr_xMnO_3$. The structures of the rhombohedral R and orthorhombic O^* phases are determined by distortions of the initial perovskite cubic structure which are associated with a rotation of the oxygen octahedra around axes of the type [111] and [110], respectively, while the structure of the orthorhombic phase O' is associated with the additional distortion of the O^* phase in the presence of static cooperative Jahn–Teller ordering of the deformed oxygen octahedra.

Let us now turn to the results of submillimeter measurements of the permittivity $\epsilon'(T)$ and dynamic conductivity $\sigma'(T)$, whose temperature dependences for $x=0.125$ are presented in Fig. 3 for the frequency $\nu=13.3$ cm^{-1}. The curves 1 and 2 refer to different polarizations of the radiation, which correspond to minimum and maximum transmission. This is evidently associated with the anisotropy of the crystal. It is evident see that appreciable anomalies are observed in the curves $\sigma'(T)$ and $\epsilon'(T)$. They correspond well with the features appearing in the curves of the static conductivity $\sigma_{dc}(T)$, magnetic susceptibility $\chi_{ac}(T)$, and magnetization $M(H)$ (Fig. 3c and 3d) as a result of

phase transitions at T_s', T_C, and T_p. The appreciable increase in $\epsilon'(T)$ after ferromagnetic ordering and a transition to the polaron phase P ($T<T_p$) attests to a substantial transformation of the crystal lattice and apparently a restructuring of the electronic spectrum of the crystal. The latter was observed recently in the optical conductivity spectra σ' for a roughly similar composition ($x=0.1$) and was manifested as the appearance of a maximum of σ' at the frequency ~ 0.5 eV (4000 cm^{-1}) for $T<T_C$,[11] attributed to electronic transitions between the states of the spin-polarized e_g band of Mn^{3+} split by the Jahn–Teller interaction. The strong growth of $\epsilon'(T)$ which we observed at temperatures $T<T_C$ is apparently due to the presence of strong Jahn–Teller spin–lattice coupling and a transition to a polaron-ordered state. We also observed a similar behavior of $\epsilon'(T)$ for compositions $x=0.1$ and 0.15, where ϵ' increased at a transition to the polaron-ordered phase P by the amounts $\Delta\epsilon' \approx 10$ and 50, respectively. At the same time, for the lightly doped compositions $x=0$, 0.05, and 0.075 $\epsilon'(T)$ did not exhibit any anomalies and decreased continuously by 5–15% as the temperature decreased. Therefore the growth (jump) in ϵ' is a characteristic feature of the transition to the polaron phase P, and its boundary with the Jahn–Teller phase O' falls in the concentration range between 0.075 and 0.1.

In summary, it has been shown in this work that the magnetic, dielectric, and conducting properties of $La_{1-x}Sr_xMnO_3$ are closely related, the relationship being most clearly manifested at phase transformations, and the complete T–x phase diagram of this system was constructed.

This work was supported by the Russian Fund for Fundamental Research (96-02-18091, 97-02-17325, and 96-15-96577).

[a)]e-mail: mukhin@ran.gpi.ru

[1] R. von Helmholt, J. Wecker, B. Holzapfel *et al.*, Phys. Rev. Lett. **71**, 2331 (1993).
[2] A. Urushibura, Y. Moritomo, T. Arima *et al.*, Phys. Rev. B **51**, 14103 (1995).
[3] É. L. Nagaev, Usp. Fiz. Nauk **166**, 833 (1996).
[4] Y. Yamada, O. Hino, S. Nohdo *et al.*, Phys. Rev. Lett. **77**, 904 (1996).
[5] H. Kawano, R. Kajimoto, M. Kubota, and H. Yoshizawa, Phys. Rev. B **53**, R14709 (1996).
[6] Y. Moritomo, A. Asamitsu, and Y. Tokura, Phys. Rev. B **56**, 12190 (1997).
[7] J.-S. Zhou, J. B. Goodenough, A. Asamitsu, and Y. Tokura, Phys. Rev. Lett. **79**, 3234 (1997).
[8] G. V. Kozlov (Ed.), *Submillimeter Dielectric Spectroscopy of Solids* [in Russian] (Trudy IOFAN, Vol. 25), Nauka, Moscow, 1990.
[9] V. Yu. Ivanov, V. D. Travkin, A. A. Mukhin *et al.*, J. Appl. Phys. **83**, 7180 (1998).
[10] A. Wold and R. J. Arnott, J. Phys. Chem. Solids **9**, 176 (1959).
[11] Y. Okimoto, T. Katsufuji, T. Ishikawa *et al.*, Phys. Rev. B **55**, 4206 (1997).

Translated by M. E. Alferieff

Destruction of localized electron pairs above the magnetic-field-driven superconductor–insulator transition in amorphous In–O films

V. F. Gantmakher,[a)] M. V. Golubkov, V. T. Dolgopolov, G. E. Tsydynzhapov, and A. A. Shashkin

Institute of Solid State Physics, Russian Academy of Sciences, 142432 Chernogolovka, Moscow Region, Russia

(Submitted 24 July 1998)
Pis'ma Zh. Éksp. Teor. Fiz. **68**, No. 4, 337–342 (25 August 1998)

The field-induced superconductivity-destroying quantum transition in amorphous indium oxide films are investigated at low temperatures down to 30 mK. It is found that, on the high-field side of the transition, the magnetoresistance reaches a maximum and the phase can be insulating as well as metallic. With further increase of the magnetic field the resistance of the film drops and in the high-field limit approaches the resistance value at the transition point, so that at high fields the metallic phase occurs for both cases. We give a qualitative account of this behavior in terms of field-induced destruction of localized electron pairs. © *1998 American Institute of Physics.*
[S0021-3640(98)01716-2]

PACS numbers: 74.25.Jb, 74.76.Db, 74.70.Ad

The theoretical description of the zero-field and field-induced quantum superconductor–insulator transitions (SIT) in a 2D superconductor is based on the concept of electron pairs which are delocalized on the superconducting side and localized on the insulating side of the transition.[1–3] According to Refs. 1–3, the temperature dependence of the film resistance near the field-induced SIT is controlled by the deviation $\delta = B - B_c$ from the critical field B_c, and the most specific among the perceptible features of the SIT is a fan-like set of resistance-versus-temperature curves $R_\delta(T)$. Such a set is expected to collapse onto a single curve as a function of the scaling variable $\delta/T^{1/y}$, where y is the critical exponent (see review[4]). Many of the SIT studies have been performed on amorphous In_2O_x ($x<3$) films, whose conductivity is caused by an oxygen deficiency compared to the fully stoichiometric insulating compound In_2O_3: by changing the oxygen content one can cover the range from a superconductor to an insulator and thus realize a zero-field SIT. On the insulating side of this SIT, activational behavior of the resistance, $R \propto \exp(T_0/T)^p$ with $p=1$ (Arrhenius law), was observed, with the activation energy T_0 tending to zero as the phase boundary is approached.[5] It was later found that applying a magnetic field results in a decrease in the resistance and a weakening of its temperature dependence from the Arrhenius law to the Mott law with exponent p

TABLE I. Parameters of two states of the sample. R_r is the resistance at room temperature; the values of R_c and B_c are determined by means of scaling analysis as described in Ref. 11.

State	R_r, kΩ	R_c, kΩ	B_c, T
1	3.4	7.5	2
2	3.0	9.2	7.2

$=1/4$ (Ref. 6). This was explained in Ref. 6 by magnetic-field-caused suppression of the binding energy Δ of localized electron pairs, which is manifested as a gap at the Fermi level.

A field-induced SIT is realized on the superconducting side of the zero-field SIT. It is indicated by the fan-like structure of the experimental curves $R_\delta(T)$, such that, in accordance with the scaling analysis, the expected collapse is indeed the case.[7] Above the field-induced SIT, the existence of two insulating phases was postulated on the basis of the results of Hall measurements;[8] however, the temperature dependence of the resistance of these phases was not studied. Reversal of a zero-bias peak in the differential resistance at the critical field B_c was observed and attributed to the granular structure of the films.[9]

Here we investigate the phase on the high-field side of the SIT, where the occurrence of localized electron pairs is predicted. We find that while this phase can be insulating or metallic, in the high-field limit the system always enters the metallic phase. This is interpreted as field-induced breaking of localized electron pairs.

The experiments were performed on a 200 Å thick amorphous In_2O_x ($x<3$) film without pronounced granularity, as was checked by the absence of a quasi-reentrant transition, i.e., the absence of a minimum on the $R_\delta(T)$ curves at low temperatures.[10] The oxygen content x could be reversibly altered by heat treatment; all experimental procedures are described in detail in Ref. 6. Assuming for the sake of simplicity that the film disorder remains unchanged during heat treatment, one finds that the quantity x controls the carrier density n, and then it is the variation of n that causes the zero-field SIT. Two states of the film were studied, having the parameters listed in Table I. Under the above assumption, the carrier density in a state should be inversely proportional to its room temperature resistance. Hence, state 2 is farther from the zero-field SIT and deeper in the superconducting phase as compared to state 1. The magnetoresistance of both states was measured in an Oxford TLM-400 dilution refrigerator in the temperature range 1.2 K to 30 mK using a four-terminal lock-in technique at a frequency of 10 Hz. The current across the sample was equal to 5 nA and corresponded to the linear response regime. The measurement runs were made by sweeping the magnetic field at fixed temperature.

Our preceding study has confirmed the existence of a magnetic-field-tuned quantum SIT in such films and revealed that this phenomenon is more general than the one considered in Ref. 2. In particular, to attain collapse of the $R_\delta(T)$ data in the vicinity of the transition in a plot versus the scaling variable $\delta/T^{1/y}$, one must take into account, e.g., the temperature dependence of the critical resistance R_c, which gives rise to a term linear in T in the dependence $R_\delta(T)$.[11]

Figure 1 displays the magnetoresistance traces for the two states of the film at a temperature of 60 mK. The critical field B_c and resistance R_c at $T=0$ (Table I) are

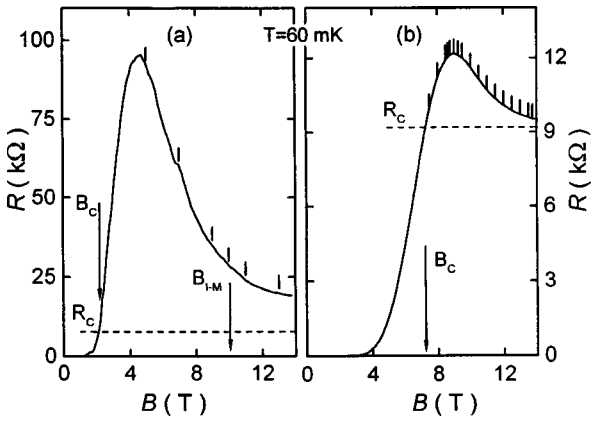

FIG. 1. Magnetoresistance of the film in state 1 (a) and in state 2 (b). The critical values R_c and B_c at $T=0$ are indicated. Also shown is the position of the metal–insulator transition, B_{I-M}, determined from Fig. 2. The temperature dependences of the resistance are analyzed at fields marked by vertical bars.

determined with the help of a scaling analysis, as described in detail in Ref. 11. One can see from the figure that with increasing field the magnetoresistance for both of the states reaches a maximum $R_{\max}$ above B_c and then drops, so that in the high-field limit it approaches the value of R_c. The relative value of the maximum $R_{\max}/R_c$ is considerably larger for state 1, which is closer to the zero-field SIT; moreover, the phase right above B_c is insulating in state 1 and metallic in state 2, as will be shown below.

The vertical bars in Fig. 1 mark the magnetic field values at which the temperature dependence of resistance is analyzed. The results of such an analysis for state 1 are represented in Fig. 2. At fields near the resistance maximum the $R(T)$ curves exhibit the

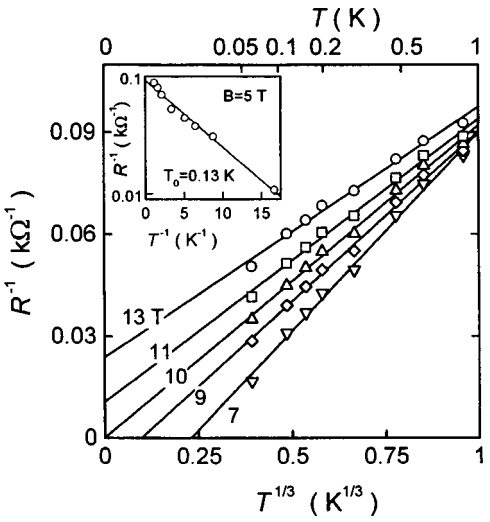

FIG. 2. Temperature dependence of the high-field conductance of state 1 at various magnetic fields. An Arrhenius plot of the conductance at $B=5$ T is displayed in the inset.

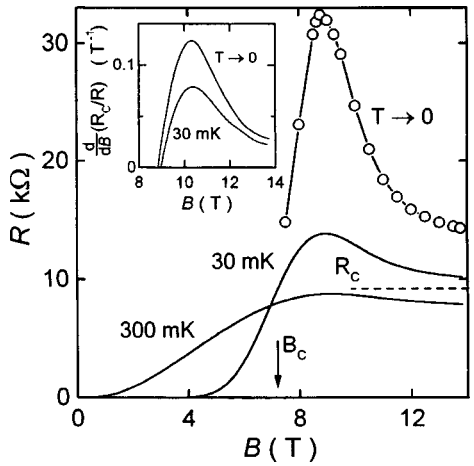

FIG. 3. Magnetoresistance of the film in state 2 at $T=30$ and 300 mK, and for $T\to 0$ as obtained from extrapolations (circles) in accordance with Eq. (1). The critical field and resistance are indicated. The field derivatives of R_c/R for $T\to 0$ and $T=30$ mK are compared in the inset.

activational behavior expected for an insulator (inset to Fig. 2). However, at higher fields the activation law does not hold, nor do the logarithmic corrections normally observed in 2D metals.[12] We therefore examine the film resistance over the field range 7 to 13 T in terms of 3D material behavior in the vicinity of metal–insulator transition:[13,14]

$$\sigma(T)=a+bT^{1/3} \quad b>0, \tag{1}$$

where the sign of the parameter a discriminates between a metal and an insulator at $T\to 0$. If $a>0$, it yields a zero-temperature conductivity $\sigma(0)=a$, whereas the negative a points to activated conductance at lower temperatures.

Let us emphasize that we are assessing the transport properties at $T=0$ as obtained by extrapolation from above 30 mK. Bearing this in mind, we determine from Fig. 2 the value $B_{I-M}\approx 10$ T for the field of the metal–insulator transition for state 1. Thus the conclusion of Ref. 8 that two phases exist above the SIT is confirmed. Yet, in contrast to Ref. 8, we find that their phase boundary is not near the resistance maximum but at an appreciably higher field, and also that the high-field phase is metallic (Fig. 1).

For state 2 the parameter a is positive over the entire field range 7.5 to 14 T above B_c, so that there is no insulating phase. The corresponding field dependence of $R_0 \equiv R_\delta(0)=1/a$ is presented in Fig. 3 along with the experimental curves $R(B)$ at 30 and 300 mK. Although the extrapolation is over a large distance, the tendency for the lowest-temperature data to approach R_c in the high-field limit seems valid for the extrapolated dependence as well.

The rise of the resistance near the field-driven quantum SIT is in agreement with theoretical ideas about localized electron pairs: above B_c it reflects the decrease of the pair localization length $\xi_{\rm loc}$ with increasing B.[1–3] That the resistance reaches a maximum with further increase in B has so far not been discussed theoretically. Nevertheless, a qualitative account of the observed resistance drop with field can be given in terms of pair breaking caused by the magnetic field.[6] In this case the behavior of the system of

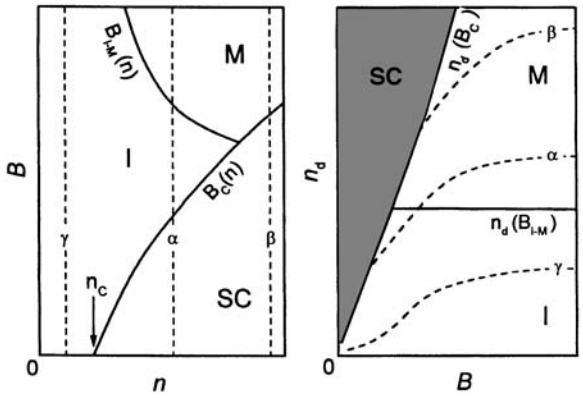

FIG. 4. Schematic phase diagram of the observed transitions in the (n,B) and (B,n_d) planes. The evolution of states α, β, γ with magnetic field is shown by dashed lines. In shaded area the value n_d is not defined.

depaired electrons is naturally determined by their density $n_d(B)$: at low n_d depaired electrons are certainly localized, whereas at sufficiently high n_d a metal–insulator transition may be expected. It is the second conduction channel that allows interpretation of the observed nonmonotonic dependences of the magnetoresistance.

In agreement with experiment, Fig. 4 shows schematically the field behavior for three states of the sample. Two of these, α and β, that are selected in the superconducting phase above the zero-field SIT at $n>n_c$ correspond to the investigated states 1 and 2, respectively. State γ selected in the insulating phase at $n<n_c$ corresponds to samples from Ref. 6. With increasing B state α undergoes a field-induced SIT at $B=B_c$, so that the depaired electrons available are localized at that small density n_d (Fig. 4). With further increase of field the value of n_d increases on account of localized pair breaking, giving rise to a metal–insulator transition in the system of depaired electrons. At $B\rightarrow\infty$, all electron pairs are expected to be broken, and so the value of n_d should be equal to the carrier density n. The different behavior of state β is due to the higher density n_d at the field-induced SIT because of higher n and B_c. As a result, the depaired electrons are already delocalized at $B=B_c$, and thus the field range of the insulating phase shrinks as one moves away from the zero-field SIT; see Fig. 4. Finally, state γ approaches the metal–insulator phase boundary with increasing B but remains insulating for all fields.[6]

Thus the concept of field-induced pair breaking requires the additional assumption that a metal–insulator transition occurs in the system of depaired electrons. Also, the theory[1–3] should be extended to include the possibility of a direct superconductor–metal quantum transition.

Although the origin of localized electron pairs is still an open question, a likely candidate for their breaking might be the paramagnetic effect. In this case the pair-breaking field should be proportional to the binding energy of a pair $B^*=2\Delta/g\mu_B$, where g is the Landé factor. It is clear that the broad field interval of the negative differential magnetoresistance points to a wide distribution of pair binding energies. To estimate the distribution function $\nu(\Delta)$ for state 2 we presume for the sake of simplicity

that, at fields above the resistance maximum, $R_0(B)$ at $T \to 0$ is inversely proportional to the density of depaired electrons (the Drude limit)

$$R_c/R_0 = n_d/n, \tag{2}$$

where n is the carrier density in the metallic state at $B \to \infty$, and n_d is given by the formula

$$n_d = n - 2\int_{g\mu_B B/2}^{\infty} \nu(\Delta)\mathrm{d}\Delta. \tag{3}$$

Then it is easy to obtain the distribution function

$$\nu(\Delta) = \frac{2n}{g\mu_B}\frac{\mathrm{d}}{\mathrm{d}B}(R_c/R_0)\big|_{B=2\Delta/g\mu_B}. \tag{4}$$

The field derivative of the ratio R_c/R_0, which is proportional to $\nu(B)$, is depicted in the inset of Fig. 3. Its behavior is similar to that of the field derivative of $R_c/R(T = 30\ \mathrm{mK})$ in spite of the long extrapolation to get $R_0(B)$; see Fig. 3.

The fact that the distribution $\nu(\Delta)$ is broad allows us to distinguish between two scenarios for localization of the electron pairs: (i) the localization radius ξ_{loc} is larger than the pair size ξ_0; and (ii) $\xi_{\mathrm{loc}} < \xi_0$. In the first case the binding energy Δ is determined mainly by intrinsic factors and is expected to be approximately the same for all pairs. In the opposite case two electrons forming a pair are localized at separate sites, and so the binding energy of the pair depends crucially on the local random potential.[6] This implies that a wide variance in Δ values. Hence, the data obtained are likely to point to the second localization scenario. We note that the limit $\xi_{\mathrm{loc}} < \xi_0$ was assumed in a model of localized bipolarons.[15]

In summary, our study of the field-driven quantum SIT in amorphous In_2O_x films shows that, on the high-field side of the transition, with increasing B the film magnetoresistance reaches a maximum and then drops, approaching in the high-field limit the resistance R_c at the transition point. We find that the high-field phase is always metallic, while the phase right above B_c can be insulating or metallic, depending on the distance to the zero-field SIT. The experimental data obtained can be understood within a model of localized electron pairs if one includes (i) a concept of field-induced pair breaking that presumes a metal–insulator transition in the system of depaired electrons; and (ii) the concept of a superconductor–metal quantum transition. That the negative differential magnetoresistance is observed in a wide field region is likely to point to a large variance of the binding energies of the localized electron pairs.

This work was supported by Grants RFBR 96-02-17497, RFBR 97-02-16829, and INTAS-RFBR 95-302 and by the ''Statistical Physics'' program of the Russian Ministry of Sciences.

[a)]e-mail: gantm@issp.ac.ru

[1] M. P. A. Fisher, G. Grinshtein, and S. M. Girvin, Phys. Rev. Lett. **64**, 587 (1990).
[2] M. P. A. Fisher, Phys. Rev. Lett. **65**, 923 (1990).
[3] S. M. Girvin, M. Wallin, M.-C. Cha *et al.*, Prog. Theor. Phys. Suppl. **107**, 135 (1992).
[4] S. L. Sondhi, S. M. Girvin, J. P. Carini, and D. Shahar, Rev. Mod. Phys. **69**, 315 (1997).

[5] D. Shahar and Z. Ovadyahu, Phys. Rev. B **46**, 10917 (1992).
[6] V. F. Gantmakher, M. V. Golubkov, J. G. S. Lok, and A. K. Geim, JETP Lett. **82**, 951 (1996).
[7] A. F. Hebard and M. A. Paalanen, Phys. Rev. Lett. **65**, 927 (1990).
[8] M. A. Paalanen, A. F. Hebard, and R. R. Ruel, Phys. Rev. Lett. **69**, 1604 (1992).
[9] K. Kim and H.-L. Lee, Phys. Rev. B **54**, 13152 (1996).
[10] Y. Liu, D. B. Haviland, B. Nease, and A. M. Goldman, Phys. Rev. B **47**, 5931 (1993).
[11] V. F. Gantmakher, M. V. Golubkov, V. T. Dolgopolov, G. E. Tsydynzhapov, and A. A. Shashkin, http://xxx.lanl.gov/abs/cond-mat/9806244.
[12] G. Bergmann, Phys. Rep. **107**, 1 (1984).
[13] Y. Imry and Z. Ovadyahu, J. Phys. C **15**, L327 (1982).
[14] V. F. Gantmakher, V. N. Zverev, V. M. Teplinskii, and O. I. Barkalov, Zh. Éksp. Teor. Fiz. **103**, 1460 (1993) [JETP **76**, 714 (1993)].
[15] A. S. Alexandrov and N. F. Mott, Rep. Prog. Phys. **57**, 1197 (1994).

Published in English in the original Russian journal. Edited by Steve Torstveit.

ERRATA

Erratum: Do excited states exist in a system of two neutrons? [JETP Lett. 67, No. 11, 903–909 (10 June 1998)]

D. V. Aleksandrov, E. Yu. Nikol'skiĭ, B. G. Novatskiĭ, and D. N. Stepanov
Kurchatov Institute Russian Science Center, 123182 Moscow, Russia

R. Wolski
Institute of Nuclear Physics, 31342 Kraków, Poland

[S0021-3640(98)01816-7]

PACS numbers: 13.75.Cs, 99.10.+g

This article consists of an error which was reported by the authors. Namely, the term ''deuteron'' was erroneously used throughout the article instead of a *correct* term ''dineutron.'' Therefore, below we offer a complete reprint of the article with the correction being incorporated. We apologize for the error.

Do excited states exist in a system of two neutrons?

D. V. Aleksandrov, E. Yu. Nikol'skiĭ, B. G. Novatskiĭ,
and D. N. Stepanov
Kurchatov Institute Russian Science Center, 123182 Moscow, Russia

R. Wolski
Institute of Nuclear Physics, 31342 Kraków, Poland

(Submitted 23 April 1998)
Pis'ma Zh. Éksp. Teor. Fiz. **67**, No. 11, 860–865 (10 June 1998)

The interaction in a system of two neutrons ($2n$) in the reaction T(d, ^{3}He) at energy $E_d=31$ MeV is investigated experimentally. Nuclear-unstable ^2n, with a decay width $\Gamma=(1.1\pm0.2)$ MeV, is observed with a large transverse cross sections in the interval of angles from 6° to 13° ($d\sigma/d\Omega(6°)\sim10$ mb/sr in the center-of-mass system). Two wide energy peaks were observed in the ^{3}He spectra. It is proposed that broad resonances with energies $E^*=(3.6\pm0.3)$ and $E^*\sim11.8$ MeV, populated in the reaction T(d, ^{3}He), are excited in the $n-n$ system. Their energy positions satisfy the interval rule $E_4:E_2\cong3.3$, indicating the possible existence of a ''rotational band'' with the characteristics 2^+ and 4^+. The ''radius'' of the dineutron is estimated from the relation

$\Delta E=\hbar^2 l(l+1)/2\mu R^2$ to be $\sim$8 fm. [S0021-3640(98)00511-8]

PACS numbers: 13.75.Cs

The question of the forces acting between two particles is a fundamental problem of classical and quantum physics. The solution of this problem has made it possible to understand the nature of electromagnetic and gravitational forces. It is well known that the existence of numerous excited states in the hydrogen atom was the key to the construction of the ''planetary'' model of the Bohr atom. Nuclear forces differ sharply from electromagnetic forces by their very short range, and the deuteron — the simplest nuclear system with an anomalously low binding energy ($\epsilon=2.22$ MeV) — does not have excited bound states like the hydrogen atom.

However, the experimental study of *pn* and *pp* scattering has firmly established an interaction in the final state in these systems with isospin $T=1$ and it has been shown that singlet d and $2p$ systems possess virtual levels near the decay threshold. In the 1960s and 1970s the hypothesis of the charge independence and symmetry of nucleon–nucleon interactions was checked experimentally in measurements of the scattering lengths. A small difference was found in the $n-n$ and $p-n$ interactions: $a_{nn}=-16.6$ fm and $a_{np}=-23.7$ fm (see, for example, the review in Ref. 1). In contrast to $p-p$ and $p-n$ scattering, because of the unavailability of neutron targets the main means of studying the $n-n$ interaction have been the reactions D(n, p), T(n, d), D(d, $2p$), T(d, ^{3}He), and T(t, ^{4}He). We note that in these investigations emphasis has been placed on confirmation of the hypothesis of charge independence and symmetry of the nuclear forces and not on a search for excited states of unstable ^2n. As a rule, the spectra have been obtained in a narrow energy range near zero binding energy of the dineutron.[2] On the other hand, in high-energy physics the searches have been conducted for ''narrow'' dibaryonic resonances (^2p) with energies of tens and even hundreds of MeV, which are traditionally far from the excitation energies characteristic for low-energy nuclear physics.[3]

The objective of the present work was to search for excited states of the dineutron in the reaction T(d, ^{3}He) by the conventional methods of nuclear spectroscopy in the interval from the ^2n ground state up to the maximum possible energies admissible under the experimental conditions ($E^*\sim 15$ MeV). Of the three variants of the search for dibaryonic resonances ($2n$,$2p$,np) the first one was chosen because a purely nuclear interaction of two identical particles occurs in this case.

The work was performed on the cyclotron at the Kurchatov Institute Russian Science Center, at a maximum deuteron beam energy $E=31$ MeV. The spectra of ^{3}He from the reaction T(d, ^{3}He) were measured in the range of angles $6-13°$. This imposed a strict limit on the intensity of the incident beam because of the enormous background due to elastically scattered deuterons. The average current of the deuterium ions on the targets was equal to ~ 0.01 μA.

Two self-supporting titanium foils of the same thickness 5.1 mg/cm^2, one of which

was saturated with tritium, served as targets. The tritium content in the Ti-T target and the presence of impurities in it were determined by special cyclotron measurements of the elastic scattering of deuterons with $E=13$ MeV. The cross sections for the elastic scattering of deuterons by tritium were taken from Ref. 4. The measurements established the content of tritium in the irradiated Ti-T foil to be 38.4% (in terms of the number of atoms relative to Ti).

The reaction products were detected with a telescope of semiconductor silicon counters with thicknesses 30 μm (ΔE — ionization-loss detector) and 1.2 mm (E — total-absorption detector), connected to a spectrometric system for multivariate analysis. The solid angle of the detecting system was equal to 1.3×10^{-4} sr.

The spectra of the ^{3}He nuclei were measured in the energy range 5–35 MeV with good statistical accuracy. In addition, spectra were systematically taken on Ti-T and Ti targets for each angle. The reaction ^{48}Ti(d, ^{3}He) and the reaction of the recoil nucleus ^{3}He(d, ^{3}He)D on the trace impurity ^{3}He(4–5%) in the Ti-T target (the peak in the discrete part of the spectra near 29 MeV) served as benchmarks for the energy calibration. The presence of this quantity of ^{3}He nuclei is due to the β decay of tritium. Figure 1 shows the energy spectra of helium nuclei from the reaction T(d, ^{3}He) after subtraction of the impurity from the reaction (d, ^{3}He) on titanium, the cross sections on which were found to be an order of magnitude smaller than on tritium. The spectra were measured at angles of 6, 8, 10, and 13° in the laboratory coordinate system. An intense peak corresponding to the interaction of two neutrons in the final state is clearly seen in the hard part of the spectra. In the figure it is marked by an arrow labeled with ^2n, and in the text below we shall refer to it as the ground state of the dineutron. A wide bump centered near 23 MeV is observed in the ''soft'' part of the spectra to the left of the ground state. A subsequent analysis — approximation of the bump by a Gaussian distribution — established that as the measurement angle increases, the center of the bump shifts continuously in the direction of low energies. This shift corresponds to the well-known energy–angle kinematic dependence for a binary reaction, which can be explained by the presence of a wide resonance in the nuclear system ^2n. Besides the features indicated, a continuous distribution with a maximum near 14 MeV, whose relative contribution increases rapidly with angle and becomes dominant at 13° (Fig. 1d), is present in the entire measured energy range. A similar picture has been observed before in measurements of the spectra of the reaction T(d, ^{3}He) with 11 MeV deuterons.[5]

We endeavored to explain the complicated structure of the spectra obtained by the well-known mechanisms of interactions in very light nuclei.

1. Resonance-like structures due to different two-step processes can appear in the spectra of the products of nuclear reactions on light nuclei. The probability of a two-stage mechanism of the reaction D + T depends on the kinematic conditions of the experiment, and it is impossible to rule out *a priori* the appearance of wide maxima in the spectrum of ^{3}He in the reaction channel $D+T\rightarrow n+{}^4He^*$ with the formation of the excited levels of the ^{4}He nucleus and their subsequent decay $^4He^*\rightarrow{}^3He+n$. Monte Carlo simulation of this process, taking into account the excitation of the levels $E^*=21$, 21.8, and 23.3 MeV in the ^{4}He nucleus,[6] established that the energies and widths of the observed maxima do not conform to the theoretical curves — dotted lines in Fig. 2 (the computed curves have not been normalized to the experimental data).

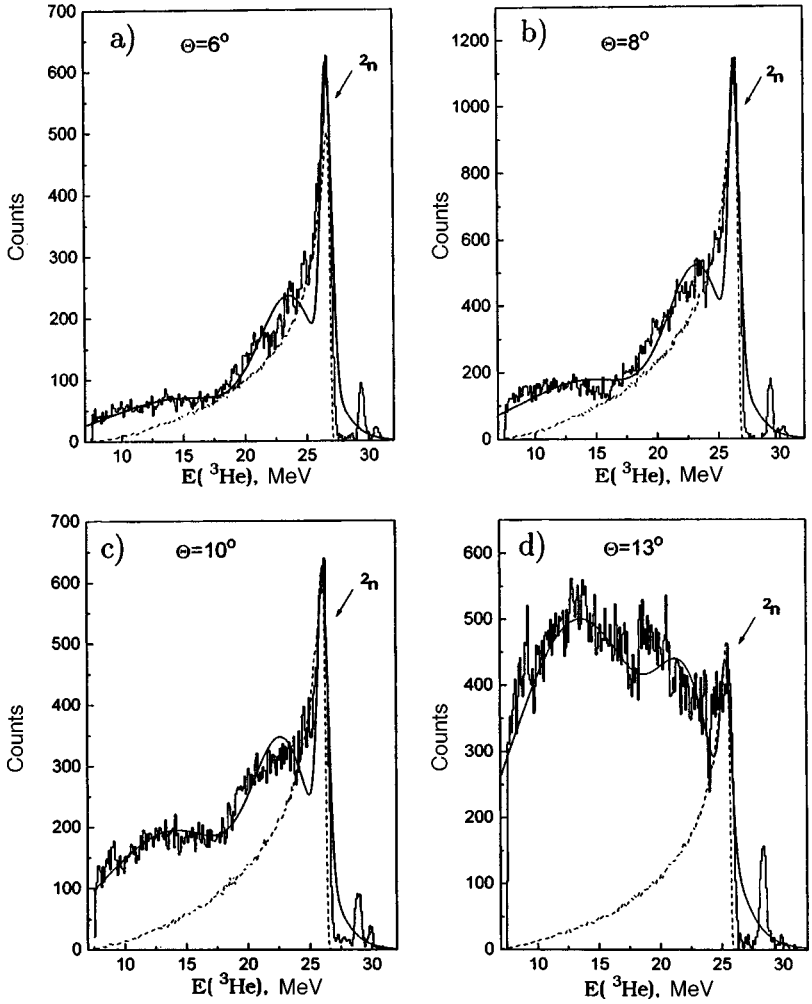

FIG. 1. Energy spectra of ^{3}He ions from the reaction T(d, ^{3}He)2n at angles of 6–13° in the laboratory system. The dotted lines show the calculation according to the Migdal–Watson theory with $a_{nn}=-16$ fm. The solid curves show the results of a fit by three Gaussian normal distributions.

2. The continuous distributions at all measured angles were calculated in the Migdal–Watson (MW) approximation. Figure 1 (dotted lines) shows the computed curves for scattering length $a_{nn}=-16$ fm. Satisfactory agreement was obtained between the computed and experimental distributions only for high energies. At 13° only the sharp rise in the hard part of the spectrum could be described by the MW method.

3. The characteristic features of the measured spectra also cannot be reproduced by calculations of the three-particle phase distribution for $D+T\rightarrow{}^3He+n+n$ (solid line in Fig. 2).

Thus none of the processes considered above reproduced the continuous ^{3}He distributions. We propose the hypothesis that in the reaction T(d, ^{3}He), besides the dineutron

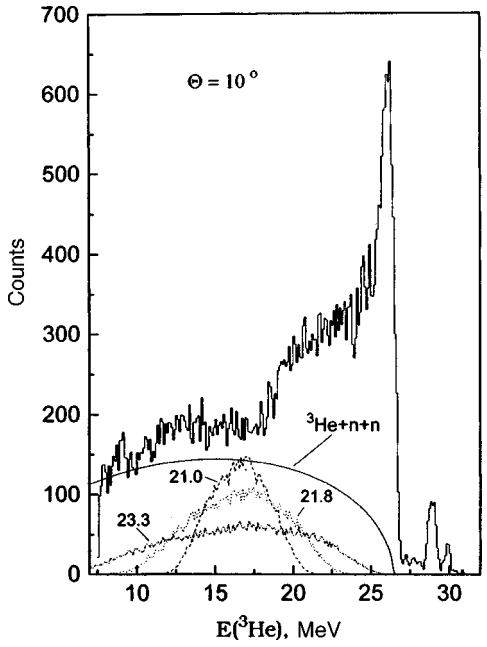

FIG. 2. Energy spectrum of ^{3}He nuclei from the reaction T(d, ^{3}He)$2n$ measured at an angle of 10°. The solid curve corresponds to the three-particle phase volume of the system $^3\mathrm{He}+n+n$ in the outgoing channel. The dotted lines show the computational results for the process $\mathrm{T}+\mathrm{D}\rightarrow n+{}^4\mathrm{He}^*\rightarrow{}^3\mathrm{He}+n+n$, which proceeds via ^{4}He levels with $E^*=21.0$, 21.8, and 23.3 MeV.

ground state, two wide resonances associated with excitation of the $n-n$ system are populated. To check this conjecture, a computer was used to carry out a χ^2-minimizing fit of the continuous spectra by three Gaussians, with automatic variation of the positions, widths, and areas of the desired resonances. The computational results are shown in Fig. 1 (solid lines). Satisfactory agreement was obtained between the experimental and computed distributions. After switching to the center-of-mass system, the excitation energies of the resonances were determined as $E^*=(3.6\pm0.3)$ MeV and $E^*\sim11.8$ MeV relative to the ^2n ground state. The values agree with one another, to within the error limits, at all measured angles. The energies satisfy the well-known interval rule $E_4:E_2\cong11.8:3.6=3.3$, indicating the possible existence of ''rotational'' excited states of the dineutron with quantum characteristics 2^+ and 4^+. The values of the spin and parity of the resonance $E^*=3.6$ MeV in ^2n are also consistent with the systematics of all even–even nuclei, according to which their first levels, except for the magic levels, possess 2^+ characteristics. The ''radius'' of a dineutron was estimated from the moment of inertia of the $n-n$ system $\Delta E=\hbar^2l(l+1)/2\mu R^2$ to be ~8 fm. This value is close to the values of the radii of the valence neutrons in weakly bound neutron-rich nuclei, such as (^{11}Li, ^{11}Be).[7,8]

In summary, in the present work we have apparently observed wide resonances in ^2n. We note a number of favorable factors and conditions which have led to the results obtained.

I. The choice of the $n-n$ system was a decisive factor for the search for dibaryonic

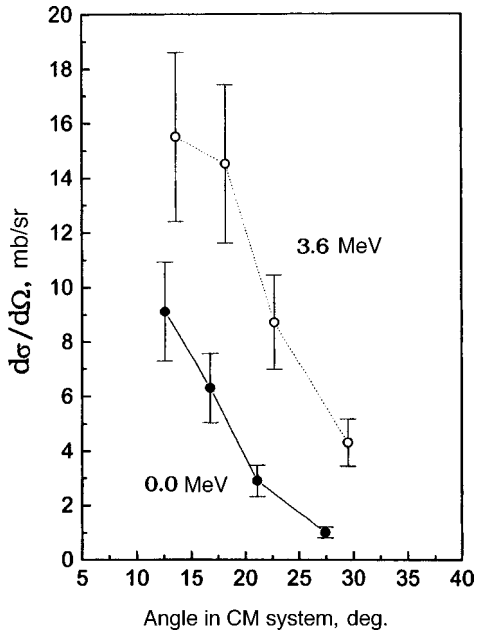

FIG. 3. Experimental angular distributions of ^{3}He from the reaction T(d, ^{3}He) for the ^2n ground state and a resonance with $E=3.6$ MeV.

resonances: a) In $p-p$ interactions, besides nuclear forces, it is also necessary to take account of Coulomb forces and their interference effects. Since the desired resonances lie in the continuum, the Coulomb repulsion of the two protons should result in smearing of their decay widths ($\Gamma \gg 1$ MeV). As an example, we indicate the unstable 2^+ levels of the nearest isobar-analog nuclei with $T=1$:^{6}He, ^{6}Li, and ^{6}Be, whose widths equal $\Gamma=0.113$ MeV, 0.540 MeV, and 1.16 MeV, respectively.[9] b) In $n-p$ scattering and in reactions where a singlet deuteron is investigated according to the spectra of the accompanying particles the analysis is greatly complicated by the contribution of the isobar-analog interaction with $=T=0$. Therefore, on account of the statistical factor, the cross section σ_s for $n-p$ scattering in the singlet state appears in the formula for the total cross section with a coefficient 1/4. c) In ^2n a purely nuclear interaction of identical particles appears and the interpretation of the levels in $n-n$ is much simpler than in the case of $n-p$ and $p-p$ systems.

II. We note an advantage of the reaction T(d, ^{3}He) for observing resonances in the dineutron. The reaction mechanism is very simple — a direct one-nucleon pickup reaction. This is indicated by the large values of the transverse cross sections ($d\sigma/d\Omega(6°)$ ~ 10 mb/sr in the center-of-mass system) and their sharp forward elongation. This is evident from Fig. 3, where the experimental angular distributions for the reaction T(d, ^{3}He) are presented. The filled circles indicate the differential cross sections for the ^2n ground state, while the open circles correspond to the resonance with $E=3.6$ MeV. Conversely, the parasitic process T(d, ^{4}He*), proceeding with formation of unstable levels of ^{4}He* and their subsequent dissociation into ^{3}He$+n$, is more complicated (two-nucleon pickup reaction). Moreover, as one can see from the table of the decay widths

TABLE I.

E^*(MeV)	J^π	Γ(MeV)
0.0	0^+	1.1 ± 0.2
3.6 ± 0.3	2^+	5.6 ± 0.5
~11.8	4^+	$\geqslant11$

presented in Ref. 6, the dissociation of ^{4}He* proceeds predominantly with the emergence of a triton and not a ^{3}He nucleus.

The main results of this work are presented in Table I, where the excitation energies of the hypothetical resonances in ^2n are given in the first column, the proposed values of the spins and parities are given in the second column, and estimates of their decay widths are given in the third column. Nonetheless, we believe that additional experiments at high incident deuteron energies (50–60 MeV) must be performed in order to confirm the results obtained.

We thank M. V. Zhukov and I. M. Pavlichenkov for helpful discussions and a number of valuable remarks, as well as SKTB ÉP of the Ukrainian National Academy of Sciences for preparing the titanium–tritium targets.

This work was supported by Russian Fund for Fundamental Research under Grant 96-02-17298a.

[1] B. Kühn, Fiz. Élem. Chastits At. Yadra, 378 (1975) [Sov. J. Part. Nucl. **6**(2), 139 (1976)].
[2] E. Baumgartner, H. E. Conzett, E. Shield, and R. J. Slobodrian, Phys. Rev. Lett. **16**, 105 (1966).
[3] Yu. A. Troyan, A. V. Nikitin, V. N. Pechenov *et al.*, Preprint R1-90-78, JINR, Dubna, 1990; Yad. Fiz. **54**, 1301 (1991) [Sov. J. Nucl. Phys. **54**, 792 (1991)].
[4] M. Ivanovich, P. G. Joung, and G. G. Ohlsen, Nucl. Phys. A **110**, 441 (1968).
[5] H. T. Larson, A. D. Bacher, K. Nagatini, and T. A. Tombrello, Nucl. Phys. A **149**, 161 (1970).
[6] D. R. Tilley, H. R. Weller, and G. M. Hale, Nucl. Phys. A **541**, 19 (1992).
[7] P. G. Hansen, A. S. Jensen, and B. Jonson, Annu. Rev. Nucl. Part. Sci. **45**, 591 (1995).
[8] I. Tanihata, J. Phys. G. Nucl. Part. Phys. **22**, 157 (1996).
[9] F. Ajzenberg-Selove, Nucl. Phys. A **413**, 1 (1984).

Translated by M. E. Alferieff